UNIVERSITY OF CALIFORNIA, SAN DIEGO

# Experiments on Asymmetry-Induced Particle Transport in Magnetized, Pure Electron Plasma Columns

A dissertation submitted in partial satisfaction of the

requirements for the degree Doctor of Philosophy

in Physics

by

Brian Paul Cluggish

Committee in charge:

Dr. C. Fred Driscoll, Chairman
Professor Thomas M. O'Neil
Professor Cliff M. Surko
Professor Charles W. Van Atta
Professor Richard L. Salmon

1995

The dissertation of Brian Paul Cluggish is approved, and it is acceptable in quality and form for publication on microfilm:

_____

_____

_____

_____

_____

_____

Chairman

University of California, San Diego

1995

*This thesis is dedicated to my mother and father,*

*who believed in me when I believed in nothing at all.*

# Contents

# List of Figures

# Acknowledgements

First and foremost among the people I would like to thank is my contrary but good-natured advisor, Fred Driscoll. He changed an artless "knob-turner" into something approximating an experimental physicist. I am also grateful for the vision of the late John Malmberg, who pioneered the field of nonneutral plasmas. Even he may have been surprised that the "Dance of the Diocotron" actually amounted to something!

It has been a pleasure working with Steve Crooks and Tom O'Neil, who answered my dumb questions about their "rotational pumping" theory; and with Bret Beck and Jerry Helffrich, my early tutors on the CV machine. Their guidance and friendship, along with that of the rest of the nonneutral plasma group at UCSD, made these past six and one-half years extremely gratifying.

I also owe a special debt of gratitude to many people outside the nonneutral group. Foremost among these are the love-of-my-life, Gail Olson, and my best friend, Bruce Stewart. Also, the friendship of Andrew Ware, John Garrett, and Rand and Jane Stoller has been much appreciated. The San Diego modern dance community has helped keep me sane at times, as well as taught me a few steps. Finally, I thank my family for their love and support.

Financial support for this research was provided by NSF Grant PHY94-21318, and by a DOE Magnetic Fusion Science Fellowship, administered by ORAU.

# Vita, Publications and Fields of Study

## Vita

| | |
|---|---|
| 26 September 1965 | Born, Framingham, Massachusetts |
| 1988 | B.S., Carnegie-Mellon University |
| 1988-1989 | Teaching Assistant, Department of Physics<br>University of California, San Diego |
| 1988-1995 | Research Assistant, Department of Physics |
| 1989 | M.S., University of California, San Diego |
| 1995 | Ph.D., University of California, San Diego |

# Publications

1. J. A. Helffrich, B. R. Beck, B. Cluggish, J. M. Fajans, and J. H. Malmberg, "Peculiar Long Time Behavior of the $l = 1$ Diocotron Mode," *Bull. Am. Phys. Soc.* **35**, 2135 (1990)

2. R. J. Groebner, W. A. Peebles, K. H. Burrell, T. N. Carlstrom, P. Gohil, R. P. Seraydarian, E. J. Doyle, R. Philpona, H. Matsumoto, and B. Cluggish, "Role of the Edge Electric Field and Microturbulence in the L-H Transition," in *Plasma Physics and Controlled Nuclear Fusion Research 1990,* Vienna: IAEA (1991)

3. J. A. Helffrich, B. Cluggish, and J. H. Malmberg, "Dance of the Diocotron and Long Time Evolution of a Pure Electron Plasma," *Bull. Am. Phys. Soc.* **36**, 2331 (1991)

4. B. Cluggish, J. H. Malmberg, T. B. Mitchell, and C. F. Driscoll, "Damping of the $l = 1$ Diocotron Mode and Associated Transport," *Bull. Am. Phys. Soc.* **37**, 1415 (1992)

5. B. Cluggish and C. F. Driscoll, "Cross-Field Transport in an Off-Axis Pure Electron Plasma," *Bull. Am. Phys. Soc.* **38**, 1972 (1993)

6. B. P. Cluggish and C. F. Driscoll, "Transport from Rotational Pumping in a Magnetized Pure Electron Plasma," *Bull. Am. Phys. Soc.* **39**, 1736 (1994)

7. A. C. Cass, B. Cluggish, F. Anderegg, K. S. Fine, C. F. Driscoll and E. Sarid, "Confinement Time Scalings of Non-neutral Plasmas," *Bull. Am. Phys. Soc.* **39**, 1737 (1994)

8. B. P. Cluggish and C. F. Driscoll, "Measurement of Transport and Damping from Rotational Pumping," *Non-neutral Plasma Physics II,* AIP Conference Proceedings #331, New York: AIP (1995)

9. B. P. Cluggish and C. F. Driscoll, "Transport and Damping from Rotational Pumping in Magnetized Electron Plasmas," accepted by *Phys. Rev. Lett.* (1995)

# Fields of Study

Major Field: Physics

Studies in Plasma Physics
Professors Patrick Diamond, Daniel Dubin, Marshall Rosenbluth, and Ronald Waltz

Studies in Mechanics
Professors Daniel Arovas and Roger Dashen

Studies in Electromagnetism
Professor Patrick Diamond

Studies in Quantum Mechanics
Professor Herbert Levine

Studies in Statistical Mechanics
Professor Daniel Arovas

Studies in Nuclear Physics
Professor Robert Gould

Studies in Particle Physics
Professor Hans Paar

Studies in Mathematical Physics
Professor Bruce Driver

# Abstract of the Dissertation

## Experiments on Asymmetry-Induced Particle Transport in Magnetized, Pure Electron Plasma Columns

by

Brian Paul Cluggish

Doctor of Philosophy in Physics

University of California, San Diego, 1995

Dr. C. Fred Driscoll, Chairman

Experiments are presented on asymmetry-induced particle transport in a magnetized, pure electron plasma confined in a cylindrical trap. This transport appears as the diffusive-like expansion of the plasma column across magnetic field lines, and is generic to many neutral and nonneutral plasma devices. Measurements of transport induced by 3 different types of asymmetry are presented.

Definitive measurements characterize the "rotational pumping" of a plasma column which is displaced from the trap axis. Rotational pumping is the collisional dissipation of the axial compressions caused by $\mathbf{E} \times \mathbf{B}$ rotation of the column through asymmetric confinement potentials; here, the confinement potentials appear asymmetric only because of the displacement of the column. This rotational pumping transport dissipates electrostatic energy but conserves angular momentum by simultaneously decreasing the displacement, which damps the $m = 1$ diocotron mode.

The rotational pumping rate is proportional to the collisional temperature equipartition rate, which drops precipitously in the cryogenic, strongly magnetized

regime; surprisingly, the transport rate is otherwise independent of magnetic field. The observed rates are in close agreement with a new theory by Crooks and O'Neil. The unusual temperature dependence of the transport explains previously observed "sawtooth" oscillations of the plasma displacement.

The $m = 1$ diocotron mode can also be damped by a "squeeze" perturbation, which is a static voltage applied to half the length of the trap. The measured dependence of the damping rate with temperature, density, and plasma radius is similar to that observed for rotational pumping. However, the Crooks and O'Neil theory predicts that the squeeze perturbation should *decrease* the damping rate, in contradiction with the observed increase. Futhermore, the measured rates are not suppressed by strong magnetization as are the rotational pumping rates.

Small, azimuthal asymmetries inherent in the trap cause "anomalous" transport even in on-axis plasmas. When the $\mathbf{E} \times \mathbf{B}$ rotation frequency of the plasma is less than the bounce frequency of a thermal electron, the transport rate is observed to strongly decrease with increasing temperature, increasing magnetic field, or decreasing density. However, when the bounce frequency is less than the rotation frequency, the transport rate is independent of temperature.

# Chapter 1

# Introduction and Summary

This thesis presents extensive, detailed measurements of asymmetry-induced, cross-field particle transport in trapped nonneutral plasmas, showing quantitative agreement with theory. The experiments characterize 3 different types of asymmetry-induced transport: a new "rotational pumping" transport which results from asymmetric end confinement fields; "squeeze damping," which results from axial variations in the wall potential; and "anomalous" transport, which results from asymmetries in the nominally cylindrical trap. Most striking is the "rotational pumping" transport, which occurs in plasmas which are displaced from the axis of the cylindrical trap. The transport rate is measured over a wide range of plasma parameters, including 4 orders of magnitude in temperature. In the cryogenic, strongly magnetized regime, a precipitous drop in the transport rate in observed. This unusual temperature dependence explains previously observed complex, nonlinear "sawtooth" oscillations of the plasma displacement and temperature. Quantitative numerical calculations of the 3-D plasma end shapes and confinement potentials are obtained using the measured charge density profiles, enabling quantitative comparison with theory.

Magnetic and electrostatic asymmetries drive particle transport in many neutral and nonneutral plasma confinement devices. In magnetic mirrors, it has long been postulated that particles whose orbits are resonant with field asymmetries en-

hance radial diffusion [55, 56], but experimental verification is difficult [23, 28, 54]. In tokamaks, "magnetic pumping" by the poloidal variation in the magnetic field is thought to dissipate poloidal rotation [59, 60]. In nonneutral traps, confinement times much greater than the rotation and transit times are important for a number of technologies and experiments [21, 24, 25, 64]; but trap asymmetries can degrade confinement [11, 12, 15, 41]. Nonneutral plasmas are often approximated as 2D guiding-center fluids on the rotational timescale [40, 29, 42] with 3D transport processes causing dissipative or viscous effects [13, 45, 46].

The pure electron plasmas described in this thesis were confined in the CV Penning-Malmberg trap [1]. This liquid-helium-cooled trap consists of a series of conducting cylinders in an axial magnetic field. Negative voltages on the end cylinders confine the plasma in the axial direction, while the magnetic field gives radial confinement. The unneutralized space-charge fields give rise to $\mathbf{E} \times \mathbf{B}$ drifts, which cause the plasma to rotate around its own axis. Chapter 2 describes the CV trap, the characteristics of the confined plasma, and the measurements and manipulations which can be performed on the plasma. The most unique aspect of the CV trap is that the strong magnetic field causes the electrons to cool through cyclotron radiation. At cryogenic temperatures, the electrons become "strongly magnetized" [2]. In this regime, the cyclotron radii of the electrons become so small that the electron motions parallel to the magnetic field and the motions perpendicular to it are no longer collisionally coupled.

The first class of asymmetry-induced transport presented in this thesis is the ubiquitous "anomalous" loss of particles due to small, azimuthal asymmetries in the cylindrical trap. These asymmetries exert a drag on the rotating plasma, causing it to slowly spin down and expand. In Chapter 3, I present measurements of anomalous transport over a wide range of plasma densities, temperatures, and

magnetic fields. I have found, somewhat unexpectedly, that the lifetime of a plasma can be extended up to 3 orders of magnitude by increasing its temperature. At high enough temperatures, the anomalous transport rate is so slow that the primary transport mechanism is the loss of angular momentum by cyclotron radiation. The plasma lifetime is also strongly dependent on density; a factor of 5 increase in density can cause a thousandfold increase in the transport rate. These results explain the anomalously short plasma lifetimes found for the CV trap relative to the EV and V′ traps [11, 12]. These two devices have similar geometries to the CV apparatus, but have much lower densities and magnetic fields, and a much narrower temperature range.

Comparing my measurements to the plasma lifetimes measured on two other traps, I have found that the transport rate on all three traps can be empirically estimated by comparing the $\mathbf{E} \times \mathbf{B}$ rotation frequency of the electrons, $f_E$, to the mean axial bounce frequency, $\overline{f_B}$. Lifetimes increase approximately as $(\overline{f_B}/f_E)^2$. However, I have also found that when $\overline{f_B} < f_E$ this scaling no longer holds, as the transport rate is then independent of temperature. This temperature plateau has not been observed on other pure electron plasma devices.

These scalings with plasma parameters are consistent with the constraints placed on the transport by conservation of energy and angular momentum. These constraints stipulate that the plasma can expand only if it increases in temperature, and that the temperature can increase only by breaking adiabatic invariants associated with the cyclotron and axial bounce motions of the electrons. The breaking of these invariants becomes more diffcult as $\overline{f_B}/f_E$ increases, resulting in the observed increase in the plasma lifetime. However, the mechanism by which the field asymmetries break the adiabatic invariants and transport the electrons radially is still unknown.

Much better understood than anomalous transport is the radial expansion and mode damping caused by the "rotational pumping" of a plasma column which is displaced from the trap axis. Rotational pumping is the dissipation, through electron-electron collisions, of the axial compressions which are caused by $\mathbf{E} \times \mathbf{B}$ rotation of the column through asymmetric confinement potentials. Here, the confinement potentials appear asymmetric only because of the displacement of the column away from the symmetry axis of the trap. Measurements of rotational pumping transport are presented in Chapter 4. I find that this rotational pumping transport conserves electron number; conserves total energy by dissipating electrostatic energy into thermal energy; and conserves angular momentum by moving the plasma column back to the trap axis as the column expands.

Rotational pumping is the mechanism by which compressional, or "second," viscosity drives the plasma towards thermal equilibrium. Driscoll [13] investigated the effect of the shear, or "first," viscosity on the transport to thermal equilibrium. However, the shear stresses induced by the displacement of the plasma column are insignificant compared to the compressional stresses.

The decrease in the displacement of the column during rotational pumping transport damps the $m = 1$ diocotron mode, which is the $\mathbf{E} \times \mathbf{B}$ drift of the entire plasma around the trap axis. At small displacements, the diocotron mode is observed to damp exponentially, indicating a linear process. The damping rate is found to be proportional to the collisional temperature equipartition rate, which drops precipitously in the cryogenic, strongly magnetized regime; surprisingly, the damping rate is otherwise independent of the magnetic field strength. The dependence of the damping rate on plasma density, length, radius, and confinement voltage has also been measured.

Analysis of the data includes numerically calculating the 3-D plasma shapes

from the measured temperature and density profiles. This enables quantitative comparison with a new theory by Crooks and O'Neil [7]; close agreement with the theory is found for nearly all the measurements.

However, when the plasma is too hot or too cold, discrepancies appear between the theory and experiments. At high temperatures, the damping rate increases with temperature, whereas the Crooks and O'Neil theory predicts a decrease. This is probably because the large thermal spread in kinetic energies gives rise to electron orbits which are not well modeled by the theory. At low temperatures, a possible resonant particle enhancement to the damping rate is not observed, presumably because the high collisionality of the plasma destroys bounce-rotation resonances. However, supplemental measurements of the heating of a nearly collisionless plasma indicate that the resonant particle theory may be valid in the proper parameter regime.

In the strongly magnetized regime, the steep drop of the collisional temperature equipartition rate causes a nonlinear instability in the plasma temperature, and consequently gives rise to unstable variations in the transport rate. This instability can cause bifurcations in the time evolution of the plasma displacement. Furthermore, if a resistive wall destabilizes the diocotron mode, nonlinear oscillations in the temperature result in "sawtooth" oscillations of the displacement of the plasma column. A simple computer model incorporating the unusual temperature dependence of the rotational pumping rate quantitatively reproduces this complicated, nonlinear "dance" of the diocotron mode [26].

The $m = 1$ diocotron mode can also be damped by applying a "squeeze" perturbation; this damping was originally observed by Fine [16]. The squeeze perturbation is a static, negative voltage applied to a cylinder which contains one-half the length of the plasma. Fine observed exponential damping of the diocotron mode, accompanied by an angular-momentum-conserving expansion of the plasma column,

much like rotational pumping.

In Chapter 5, I present my own measurements of squeeze damping in the CV trap. For long enough plasmas, I observe the same enhanced damping as Fine, and find that the dependence of the damping rate on temperature, density, and plasma radius is similar to the dependence observed for rotational pumping. However, numerical calculations of the 3-D density profiles of the experimental plasmas indicate that the squeeze perturbation should reduce the azimuthal variation in the plasma length. Hence, Crooks and O'Neil's theory predicts that squeeze should *reduce* the damping rate, in contradiction with the observed increase. Furthermore, the measured rates are not suppressed by strong magnetization as are the rotational pumping rates.

Thus, some other theory is needed to explain squeeze damping. Fine's data showed some agreement with a resonant particle, beat-wave damping theory by Crawford and O'Neil [5, 6]. However, this theory is also insufficient to explain my measurements, as the theory gives the wrong scaling with plasma density. Also, many CV plasmas are too collisional for resonant particle theories to be valid.

Appendix A contains data on plasma heating caused by modulating the plasma length by applying azimuthally symmetric, oscillating voltages to the confinement cylinders. I find that the most efficient heating occurs when the frequency of the applied voltage $f_{mod}$ is near the mean bounce frequency $\overline{f_B}$. For $f_{mod} \leq \overline{f_B}$, the heating rate strongly increases with $f_{mod}$ and strongly decreases with $\overline{f_B}$. The scalings of the heating rate with $f_{mod}$ and $\overline{f_B}$ show some agreement with a heating rate derived from the Crooks and O'Neil resonant particle rotational pumping theory [7]. This implies that resonant particles may enhance rotational pumping transport in plasmas that are not too collisional.

Analytical and numerical calulations of the end shapes of off-axis plasma

columns are presented in Appendix B. The curvature of the confining equipotentials causes the plasma to be longer on one side of the plasma than the other when the column is displaced from the trap axis; this length difference is the basis for rotational pumping. The difference in the length can be estimated analytically when the plasma is wide or hot. However, perturbation of the space charge fields increases the difference in cold, narrow plasmas. The end shapes of these plasmas must be calculated numerically in order to correctly predicted the rotational pumping transport rate.

In Appendix C, I derive an upper limit to the plasma lifetime imposed by the loss of angular momentum by cyclotron radiation. If the plasma is heated to a high temperature by azimuthally symmetric voltages, radiation of angular momentum can be the primary transport mechanism.

Appendices D and E contain heuristic derivations of diocotron mode damping rates. In Appendix D, I derive the rotational pumping damping rates of the $m \geq 2$ modes, and find that they are nearly identical to the damping rate of the $m = 1$ mode. In Appendix E, I calculate the damping rates due to shear viscosity. The $m \geq 2$ modes should damp exponentially, and these shear-induced damping rates can be larger than the rotational pumping-induced damping rates in the strongly magnetized regime. In contrast, shear viscosity damps the $m = 1$ mode only nonlinearly, and at a much slower rate than rotational pumping.

In Appendix F, I give an alternate derivation of the rotational pumping transport rate. Whereas the derivation in Chapter 4 uses conservation of energy and angular momentum, this derivation considers the forces on the plasma from the confining fields. The drifts arising from these forces result in the expansion of the plasma column and the damping of the $m = 1$ diocotron mode.

# Chapter 2

# Background

## 2.1 Overview

This chapter describes the experimental apparatus and the measurements and manipulations performed on the plasma. The experiments described in this thesis were performed on the CV device at the University of California in San Diego. The "C" in CV stands for Cryogenic and the "V" denotes the axial Voltage confinement. The CV device is a liquid helium cooled Penning-Malmberg trap. A pure electron plasma is contained within the trap by the application of magnetic and electric fields.

Section 2.2 gives a description of the CV apparatus. The Penning-Malmberg trap consists of a series of conducting cylinders enclosed in a vacuum chamber. The vacuum chamber resides in the bore of a superconducting solenoid, and both are enclosed in a liquid-helium filled cryostat. Section 2.3 describes how the electrons are injected into the trap, where they are confined axially by negative voltages and radially by the magnetic field.

Section 2.4 describes how the density and potential profiles of the electron plasma are determined. The plasma density profile is measured by dumping the plasma onto collector plates. Azimuthal motions of the plasma are monitored by measuring currents induced on electrically isolated "sector probes." A computer code

then calculates the 3-D equilibrium density and potential from these measurements and the measurement of the plasma temperature.

Temperature measurements are described in Section 2.5. The temperature is determined by measuring the rate at which the electrons escape as the confining voltage is slowly lowered. The plasma can cool to temperatures as low as 4.2K through cyclotron radiation. Conversely, the plasma can be heated, as described in Section 2.6, by modulating the plasma length.

Sections 2.7 and 2.8 describe the rapid evolution of the plasma to a long lived equilibrium state. Within 10-100 msec, the plasma is in local thermal equilibrium along each magnetic field line and the temperature and density are azimuthally uniform around the plasma axis.

Section 2.9 decscibes how the magnetic field is aligned with the Penning-Malmberg trap. While alignment is not neccesary for good plasma confinement, it is neccesary for density and temperature measurements.

## 2.2 Description of CV Apparatus

A schematic of the CV cryostat, magnet, and vacuum vessel is shown in Figure 2.1. The Penning-Malmberg trap resides in an evacuated brass tube inserted into the bore of a superconducting solenoid, which provides a uniform, axial magnetic field. Superconducting saddle coils provide perpendicular components to the solenoidal field, enabling the field to be aligned with the axis of the trap. The solenoid and vacuum vessel are immersed in liquid helium at the bottom of a cryostat. The liquid helium cools the solenoid, vacuum vessel, and trap to 4.2K, which serves three purposes. First, it causes the solenoid to be superconducting, allowing the generation of fields up to 64 kG. Second, it acts to cryopump the vacuum vessel to a pressure estimated to be lower than $10^{-13}$ torr [1]. This extremely low pressure

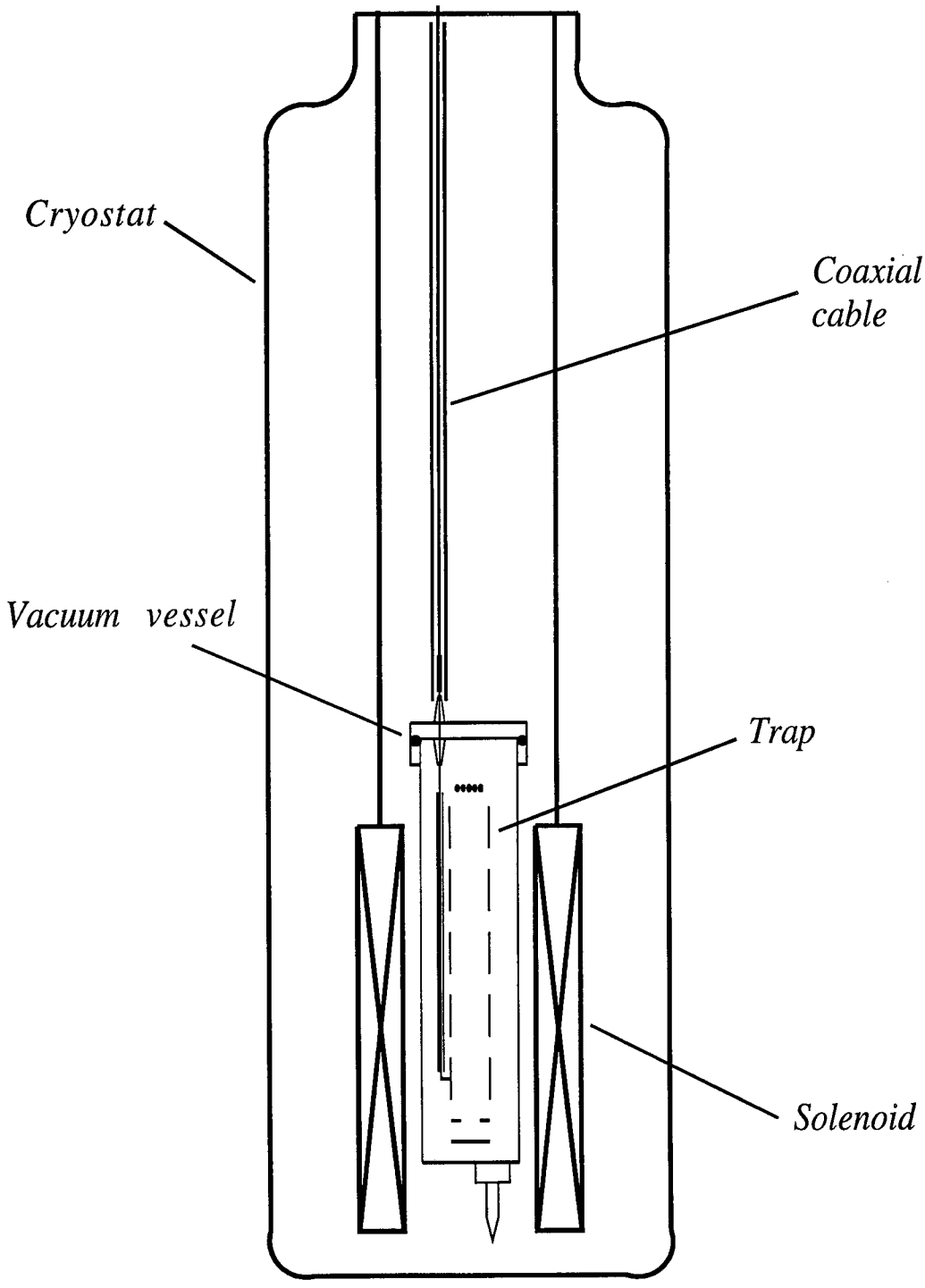


**Figure 2.1:** Schematic of the CV apparatus. The cryostat is filled with liquid helium, which cools the magnet, vacuum tube, and trap to 4.2K.

effectively eliminates collisions between electrons and neutral atoms, which would otherwise cause the loss of electrons from the trap [37]. It also allows the plasma to be heated to arbitrarily high temperatures without causing ionization of the background gas. Finally, the liquid helium provides a 4.2K background temperature to which the electrons can cool.

The Penning-Malmberg trap is shown schematically in Figure 2.2. The electrons are generated through thermionic emission by ohmically heating a filament. The filament is a spiral of 0.001 inch diameter thoriated tungsten wire, located such that the longitudinal axis of the solenoid runs through the center of the spiral. Because of the thinness of the wire and the strength of the magnetic field, the $\mathbf{I} \times \mathbf{B}$ force would destroy the filament if it was located inside the solenoid. Instead, the filament is located in the fringing fields outside the bore of the solenoid, where the magnetic field strength is a factor of 20 less than its value in the bore.

The trap consists of a series of conducting cylinders arranged along the solenoidal axis from the filament into the bore of the magnet. The cylinders, also called rings, are made of gold-plated OFHC copper and vary in length from 1.27 cm to 11.43 cm. Each has a inner wall radius of $R_w$= 1.27 cm and a wall thickness of 0.127 cm. The sector probe ring has 2 electrically isolated wall sectors, shown schematically in Figure 2.3; these "sector probes" are 0.4318 cm in axial length, and 60° in azimuthal extent.

The inject and compress cylinders are located in the low magnetic field region. These cylinders are sequentially biased so as to push the electrons which are emitted from the filament into the uniform, high field region in the bore of the solenoid. Radial confinement of the electrons is provided by the magnetic field, which causes the electrons to spiral about the field lines in tight cyclotron orbits. Longitudinal confinement is provided by applying negative voltages to the cylinders at either end

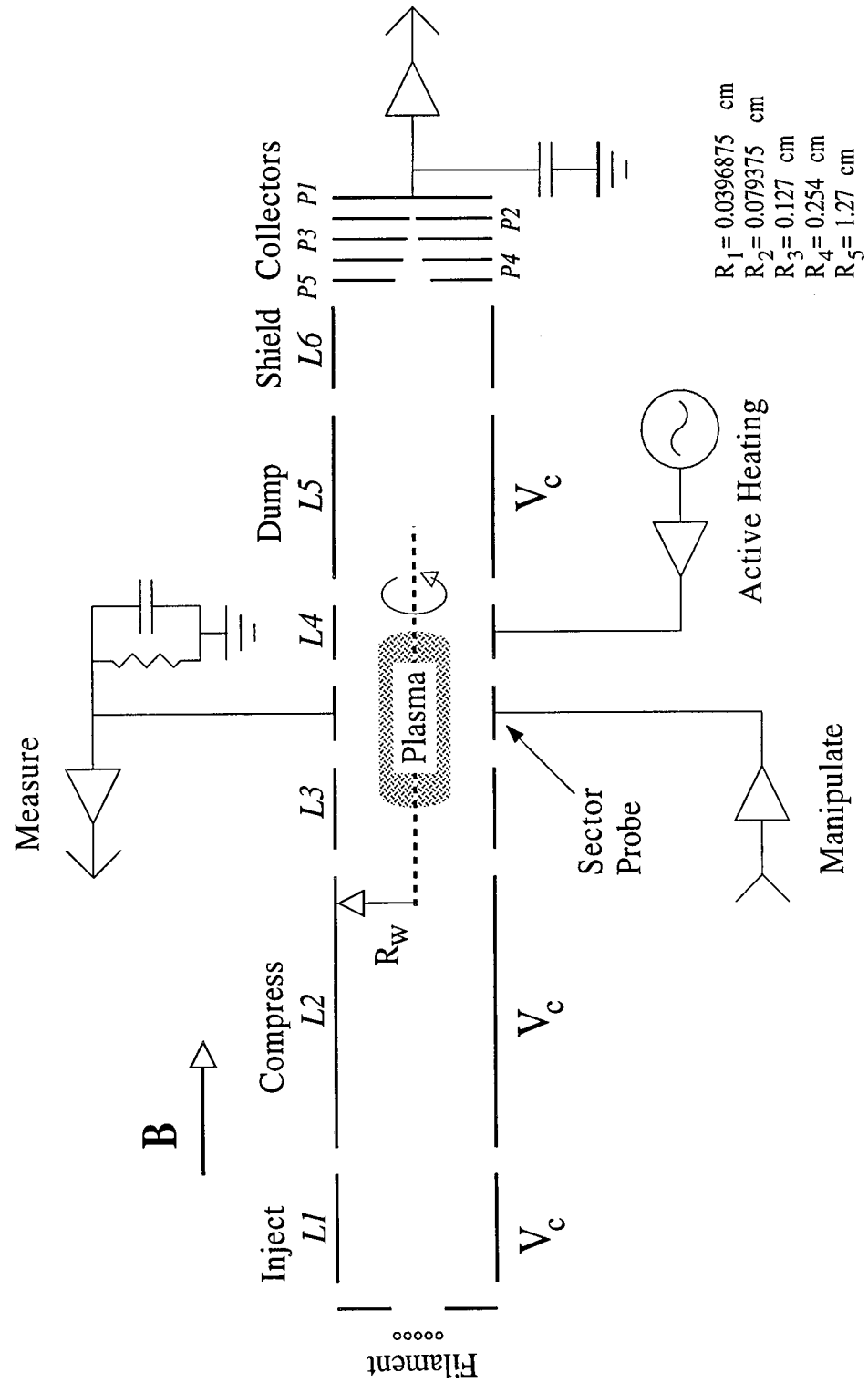


**Figure 2.2:** Schematic of the CV Penning-Malmberg trap, showing the confinment cylinders and collector plates. The filament, L1, and L2 are in the low magnetic field region. The $R_i$ are the collector radii. The sector probe ring is shown in Figure 2.3.

of the plasma. The applied voltages draw any positive ions that may be present out of the plasma, leaving only the negatively charged electrons. The length of the trapped plasma depends on the length of the cylinders in which it is confined and on the voltages confining it. While the plasma is confined, the sector probes can be used to detect or manipulate azimuthal modes in the plasma. The entire trap is engineered to be cylindrically symmetric, in order to minimize the loss of electrons.

At the opposite end of the cylinders from the filament are 5 collector plates arranged in series, labeled P1-P5 in Figure 2.2. Each of the first 4 plates has a collimator hole through its center. When the plasma is dumped, the electrons stream along the magnetic field lines, passing through the succesively smaller holes until they hit the collectors. This provides information about the radial charge distribution of the electrons. The effective radius of a collector is the radius of the hole in the plate before it. These radii are shown in Figure 2.2 as $R_1$ – $R_5$. The radial size of the P5 collector is effectively $R_w$.

A shielded copper lead is attached to the outside of each ring and each collector. These leads run out of the vacuum vessel through epoxy feedthroughs, and then up and out of the cryostat. Each ring or collector can thus be attached to a power supply, amplifier, or ground, in order to detect or transmit voltages. The lead from the last collector, which is used in measuring the plasma temperature, connects to a low-noise amplifier which is located inside the crysotat. Its temperature is maintained at around 100K.

## 2.3 Operation of the CV Apparatus

The CV apparatus is operated in an inject, manipulate, dump cycle. A plasma is captured, subject to various voltages applied to the trap walls, non-destructively measured while it evolves, and then destructively measured by dumping

it onto the collector plates. The response of the plasma to a change in an experimental parameter is measured over many cycles, or "shots." Measurements of the plasma density and temperature are shot-to-shot repeatable to within about 1%.

For nearly all of the experiments described in this thesis, the plasma was confined in 3 grounded cylinders of total length $L_c = 4.953$ cm. The confining voltage, $V_c$, ranged from -100V to -250V, depending on the space charge potential and temperature of the plasma being confined. These values of $L_c$ and $V_c$ give a typical plasma length of $L_p \sim 3.5$ cm. Longer or shorter plasmas can be captured by changing the confinement region and/or the confining voltage, giving 2 cm $< L_p <$ 10 cm.

The injection of the electrons into the trap begins by biasing the center of the filament spiral to $V_b$, while a voltage $V_f$ is placed across the filament to make the center is more negative than the edge. Typically, $V_f$ = -1.5 V and -10 V $< V_b <$ -20 V. The inject and compress rings are then grounded, while the dump ring is biased to $V_c$. Electrons boil off of the filament and stream into the grounded cylinders. The electrons are allowed to fill the trap for several milliseconds. The voltage on the inject ring is then ramped to $V_c$ over a millisecond, trapping the electrons between the inject and dump rings. The compress ring voltage is then likewise ramped over a few milliseconds, compressing the plasma into the grounded confinement region. This two stage injection process is required to push the electrons through the "magnetic mirror" formed by the fringing fields at the end of the solenoid. It also allows more electrons to be captured than if the voltages on the inject and compress rings were all ramped to $V_c$ at the same time.

Using this injection process, a pure electron plasma column is created along the axis of the trap. The trapped plasma typically has an initial density $10^9 < n < 10^{10}$ cm$^{-3}$ and temperature $T \sim 1$ eV; the magnetic field is typically $B \sim 40$ kG.

The column is initially very narrow; pushing the plasma from the low field region near the filament into the high field region compresses the plasma radius, $R_p$, to less than 10% of $R_w$.

The electrons in the plasma execute tight cyclotron orbits around magnetic field lines, bounce back and forth along the field lines, and $\mathbf{E} \times \mathbf{B}$ drift across the field lines. The cyclotron frequency, $\omega_c = eB/m_e c$, is typically $10^{12}$ Hz, and is much greater than any other frequency. The mean bounce frequency, $\overline{f_B} \equiv \bar{v}/2L_p$, defined as the bounce frequency of an electron moving at the thermal velocity $\bar{v} \equiv \sqrt{kT/m_e}$, is typically $4 \times 10^5$ to $3 \times 10^7$ Hz. The $\mathbf{E} \times \mathbf{B}$ rotation frequency, $f_E \approx nec/B$, is the rate at which the plasma rotates about its own axis due to its self electric field; it typically ranges from $5 \times 10^5$ to $3 \times 10^6$ Hz.

Once the plasma is trapped, it can be manipulated to set up a desired initial condition. One common manipulation is the creation of an $m = 1$ diocotron mode, which is shown schematically in Figure 2.3. This mode is the $\mathbf{E} \times \mathbf{B}$ orbit of the entire plasma column around the axis of the trap due to the electric field of its image charges in the conducting walls. The frequency of this mode, $f_d \approx f_E(R_p/R_w)^2$, is typically between $5 \times 10^3$ Hz and $3 \times 10^4$ Hz.

The $m = 1$ diocotron mode is easily created by biasing a sector probe for a time equal to about 1/2 an orbit period. This causes the plasma to $\mathbf{E} \times \mathbf{B}$ drift away from the trap axis. Once created, the mode can be monitored by measuring the induced charge on the other sector probe. It is observed to be a very stable mode, lasting for many thousands of orbits without a change in amplitude [16]. The $m = 1$ diocotron mode can also be manipulated with feedback techniques. The received signal on one sector probe is phase shifted, amplified, and then fed back to the other sector probe. Positive feedback grows the mode, and negative feedback damps it.

After the plasma has been held for the desired amount of time, the plasma

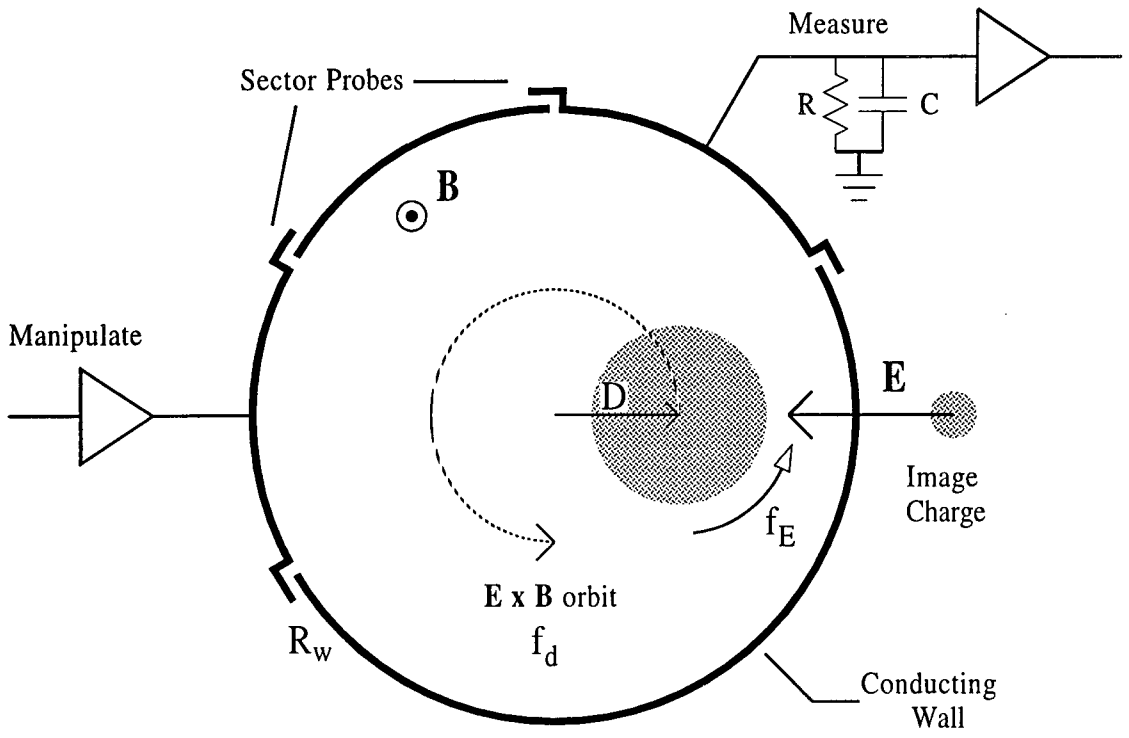


**Figure 2.3:** Schematic of the $m = 1$ diocotron mode and sector probe cylinder. The mode is detected through the image charge current on the electrically isolated sectors.

is dumped by ramping the dump ring voltage to +10 V. The shield cylinder acts to minimize the charge induced on the collectors by the ramping of the dump ring voltage. The electrons stream out and hit the collection plates, which are typically biased to +90V. By measuring the voltage on each collector, the amount of charge dumped on each can be determined if their capacitances are known. This provides information about the plasma radial charge distribution or temperature, depending on the speed at which the dump ring voltage is ramped.

## 2.4 Density Measurements

Using the sector probe and charge collector measurements, the full 3 dimensional density and potential profiles of the plasma, $n(r, \theta, z)$ and $\phi(r, \theta, z)$, can be

determined assuming that the only azimuthal perturbation of the plasma density is the displacement of a circular plasma column from the trap axis. This condition is easily satisfied if the self rotation of the column has had sufficient time to shear apart any azimuthal structure [29, 30], and if the amplitude of the $m = 1$ diocotron mode is small compared to $R_w$. The center of the trap is used as the origin of the cylindrical coordinate system $(r, \theta, z)$.

### 2.4.1 Sector Probe Measurements

The displacement, $D$, of the plasma column from the trap axis is determined by measuring the charge induced on a sector probe by the $m = 1$ diocotron mode. For small displacements of the plasma column, Fine [18] has shown that the plasma is nearly circular in cross section. The rapid motion of the electrons along the field lines also ensures that the density is nearly uniform along the field lines. The image charges which the plasma induces are thus nearly the same as those induced by a finite length line charge of uniform "line density" (charge per unit length). Kapetanakos and Trivelpiece [33] calculated the current induced on a sector probe located at the middle of such a plasma. If the plasma is orbiting with frequency $\omega_d = 2\pi f_d$ at a displacement $D$ about the trap axis, the current is can be written as

$$i_s = \frac{2N_L e\omega_d L_s}{\pi} \sum_{n=1}^{\infty} \sin\left(\frac{n\Delta\theta}{2}\right) \sin(n\omega_d t - \theta_s) \times \left[\left(\frac{D}{R_w}\right)^n - 4\left(\frac{R_w}{L_s}\right) \sum_{k=1}^{\infty} \frac{J_n(j_{nk}\frac{D}{R_w}) \sinh(j_{nk}\frac{L_s}{2R_w})}{(j_{nk})^2 J_{n+1}(j_{nk})} \exp\left(-j_{nk}\frac{L_p}{R_w}\right)\right]. \quad (2.1)$$

Here $N_L$ is the line density of the plasma, $L_s$ is the axial length of the sector probe, $\Delta\theta$ is the angular displacement of the sector probe, $\theta_s$ is the angular position of the sector probe center, and $j_{nk}$ is the $k$th zero of the $J_n$ Bessel function. The first term in the square brackets is the expression for an infinite length plasma. The second term is the correction due to finite length, which goes to zero as $L_p \to \infty$. In the experiments descibed in this thesis, the finite length correction was typically under

10%. [Note that the right hand side of Eq.22 in Ref.[33] should be multiplied by 2, as noted by Fine [16]. Also, the (R/a) term in front of the second summation should be a/d.]

The voltage measured by the the sector probe amplifier is $V_s = i_s Z$, where $Z$ is the impedance between the sector probe circuit and ground. The capacitance of the measurement circuit, $C$, is approximately 400 pF, which is mainly in the coaxial cable running out of the cryostat. The circuit resistance, $R$, is 10 M$\Omega$. Because $R \gg 1/\omega_d C$, the impedance is mostly capacitive, i.e. $|Z| \approx 1/\omega_d C$, and $V_s$ is independent of the diocotron mode frequency $\omega_d$. The voltage is also phase-shifted relative to the induced current; i.e. the $\sin(n\omega_d t - \theta_s)$ terms in Equation 2.1 become $-\cos(n\omega_d t - \theta_s)$. This signal can be sent to a spectrum analyzer, which isolates the different harmonics. Note that $J_1(j_{nk} D/R_w) \propto D/R_w$ for $D \ll R_w$. Thus, $D$ is proportional to the fundamental component of the spectrum, and $D$ can be deduced if $N_L$ is known.

### 2.4.2 Radial Density Profile Measurements

Ramping the voltage on the dump ring quickly (1 $\mu sec$) causes all the electrons to hit the collectors on a time scale much faster than the $RC$ time of the amplifiers connected to them, which causes a voltage step easily measured by the capacitively coupled amplifiers. The charge collected on the $i$th collector is an integral of $n(r, \theta, z)$ over the area of the collector and over the axial length of the plasma:

$$Q_i = -e \int_{R_{i-1}}^{R_i} r dr \int d\theta \int dz \, n(r, \theta, z), \qquad i = 1, 5 \tag{2.2}$$

where $R_i$ is the outer radius of the $i$th collector, and $R_0 \equiv 0$. The $z$-integrated charge density averaged over the collector, $q_i$, is obtained by dividing the $Q_i$ by the area of the collector:

$$q_i = \frac{Q_i}{\pi(R_i^2 - R_{i-1}^2)}, \tag{2.3}$$

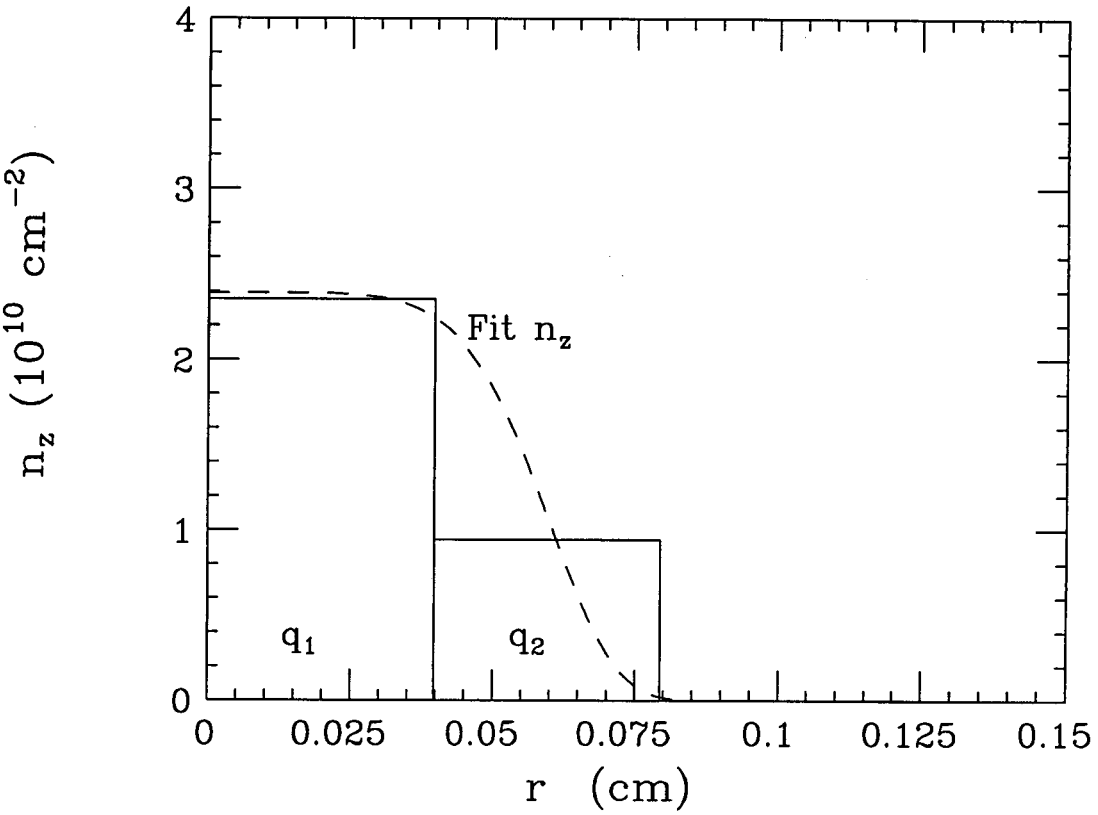


**Figure 2.4:** Measured $q_i$ and the $n_z(r)$ profile fit to them. The rectangles show the average $n_z$ on the P1 and P2 collectors.

while the total number of electrons, $N$, is the sum of the number on each of the 5 collectors:

$$N = \frac{1}{-e}\sum_{i=1}^{5} Q_i \tag{2.4}$$

If the plasma is azimuthally symmetric and is on axis, the $q_i$ provide a crude approximation to the plasma's $z$-integrated radial density profile, $n_z$, i.e.

$$n_z(r) \equiv \int dz\, n(r,z) \approx \frac{q_i}{-e}, \tag{2.5}$$

for $R_{i-1} < r < R_i$.

Figure 2.4 shows a typical measurement of $n_z(r)$. The histogram shows the values of $q_1$ and $q_2$. This plasma column was so narrow that $q_3$ was very small, and $q_4$ and $q_5$ were zero. In order to obtain a more useful radial profile, the charge

measurements from the five collectors were often fit to a density profile curve of the form

$$n_z(r) = n_z(0) \exp\left[ -\left(\frac{r}{R_{fit}}\right)^p \right], \tag{2.6}$$

where the "fit radius" $R_{fit}$ and the "steepness factor", $p$, were the fitting parameters. The central density was normalized to the measured total charge by

$$n_z(0) = \frac{N}{\pi R_{fit}^2 \Gamma(1+2/p)}, \tag{2.7}$$

where $\Gamma$ is the gamma function. [Note that if $p \to \infty$, $n_z(r)$ becomes a square profile and $\Gamma(1+2/p) = 1$.] This profile was chosen because it resembles the density profiles measured with better density profile diagnostics on other pure electron plasma devices [16], and because the 2 free parameters allowed a range of plasma sizes and shapes. The dashed curve in Figure 2.4 is the profile fit to the $q_i$. Unless otherwise noted, the data in this thesis was analyzed using these fit profiles.

Towards the end of the time period in which these experiments were performed, I developed an improved method of measuring density profiles. This method requires many shots to obtain one density profile, relying on the reproducibility of the plasma. At the end of a confinement period, the plasma is displaced from the trap axis. The displacement $D$ of the column is measured over about 10 msec. The plasma is then dumped while still off axis. The cylindrical symmetry of the trap ensures that the charge dumped on each collector is independent of the phase of the $m = 1$ diocotron mode at the time of dump. By displacing the electron column a different amount on each shot, the dependence of $q_1$ on $D$ is obtained, providing many data points of information about the density profile. However, the radius of the central collector is too large compared to plasma radius to obtain good resolution of $n_z(r)$. In order to obtain better resolution this data has to be deconvoluted.

The deconvolution method used was basically a matrix inversion. The measured data provides $q_1(D)$, the charge dumped onto the P1 collector as a function of

the column displacment. This data was fit with a cubic spline that was smoothed by minimizing the second derivatives of $q_1(D)$. The cubic spline was then interpolated to obtain a smoothed set of $q_1$ at evenly spaced displacements. I denote this data set by the vector $q_{sm}(D_i)$, where the $D_i = i\Delta$ (for i=0 to N), are N+1 displacements spaced $\Delta$ apart. The true, $z$-integrated density profile $n_z(r)$ is then written as the solution of the matrix equation

$$q_{sm}(D_i) = -e\sum_{j=0}^{N} W_{ij} n_z(r_j) \tag{2.8}$$

where $r_j = j\Delta$ and $W_{ij} = A_{ij} - A_{i,j-1}$ is the convolution matrix. The $A_{ij}$ terms are given by

$$A_{ij} = \begin{cases} \pi R_1^2 & \text{if } R_1 + D_i < r_j \\ \pi r_j^2 & \text{if } R_1 - D_i > r_j \\ 0 & \text{if } D_i - R_1 > r_j \end{cases} \tag{2.9}$$

and

$$A_{ij} = R_1^2 \arccos(X_{ij}/R_1) + r_j^2 \arccos((D_i - X_{ij})/r_j) - D_i\sqrt{R_1^2 - X_{ij}^2}$$
$$\text{if } |r_j - D_i| < R_1,$$

where $X_{ij} = (R_1^2 - r_j^2 + D_i^2)/2D_i$. Equation 2.8 can be solved by directly inverting matrix $W_{ij}$, but any noise in the data will be amplified, resulting in a very noisy answer for $n_z(r_i)$. Instead, a method due to Phillips [51] and Twomey [62] was used to introduce smoothing into the deconvoluted profile. In addition, an iterative method due to Subrahmanya [61] was used to restrict the answer for $n_z(r_i)$ to positive densities.

Figure 2.5 shows the density profile obtained with this method for the plasma of Figure 2.4. The data points are $q_1(D)$; the error bars are the result of averaging over 3 shots for each value of $D$. The solid curve is the deconvoluted profile obtained using a $r_j$ interval of $\Delta = 0.0065$ cm, less than 1/10th the diameter of the P1 collector. Note that the fit profile in Figure 2.4 is fairly close to the deconvoluted

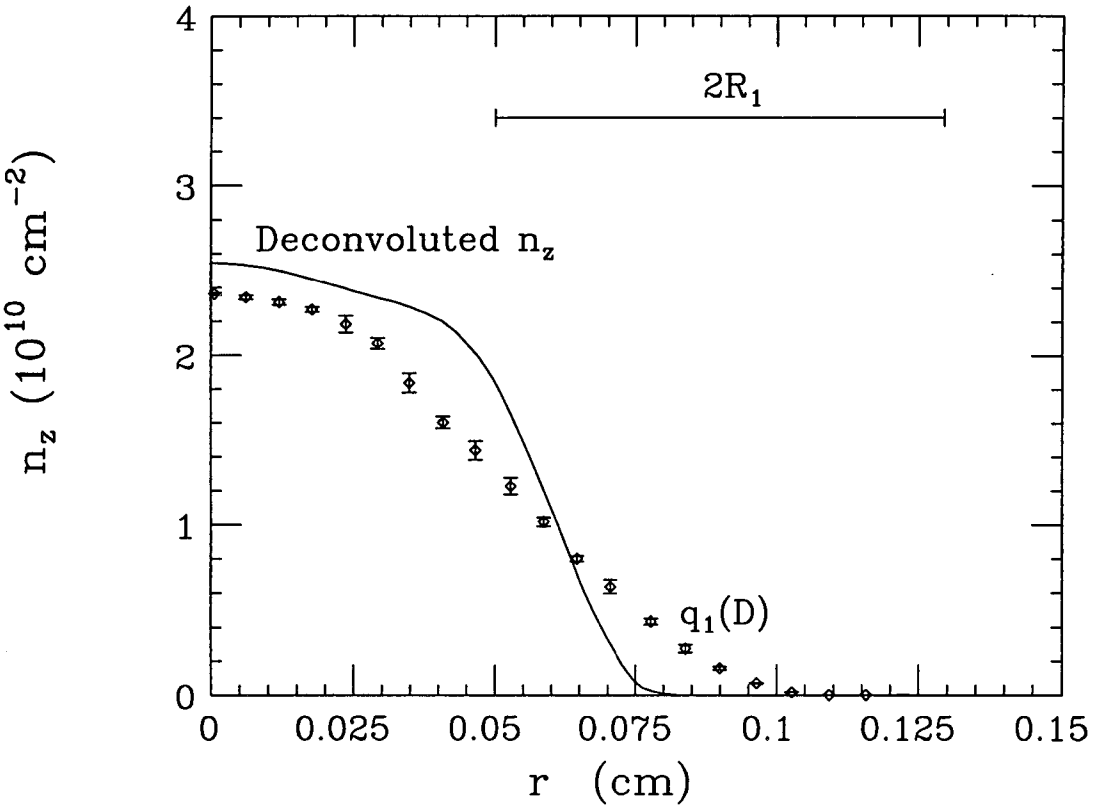


**Figure 2.5:** Measured $q_1(D)$ and the deconvoluted $n_z(r)$. The $r_j$ interval for the deconvoluted profile is 0.0065 cm, less than 1/10th the diameter of the P1 collector shown by the horizontal bar.

profile in Figure 2.5, demonstrating the reasonableness of the functional form of the fit profile.

### 2.4.3 3D Density and Potential Profiles

The CV device has no diagnostics which directly measure the electron density distribution along $z$. The axial distribution is numerically calculated, given $n_z(r)$ and $D$, assuming that the electrons are in thermal equilibrium along each magnetic field line. This is accomplished with a three-dimensional Poisson-Boltzmann code which calculates the potential $\phi$ by solving Poisson's equation on a Cartesian grid,

$$\nabla^2\phi(x,y,z) = 4\pi e\, n(x,y,z). \tag{2.10}$$

The grid size is typically $125 \times 125 \times 200$, with $r^2 = x^2 + y^2$. The code then iteratively solves for the density assuming a Boltzmann distribution of electrons in $z$, i.e.

$$n(x,y,z) = n_0(x,y)\ \exp\left(\frac{e\phi(x,y,z)}{kT(x,y)}\right), \tag{2.11}$$

where $n_0(x,y)$ is determined from $n_z(r)$. The iterative calculation will not converge if the Debye length, $\lambda_D = \sqrt{kT/4\pi ne^2}$, is smaller than the grid spacing. In that case, I find the lowest temperature for which the calculation converges and use the solution as an approximation to $n(x,y,z)$ and $\phi(x,y,z)$. Using $n(x,y,z)$ and $\phi(x,y,z)$, I define the mean plasma length by

$$L_p = \frac{\int dxdydz\ n(x,y,z)\ [n_z(x,y)/n(x,y,z=0)]}{\int dxdydz\ n(x,y,z)}, \tag{2.12}$$

and the average line density by

$$N_L = \frac{N}{L_p}. \tag{2.13}$$

## 2.5 Temperature Measurements

The CV apparatus can create plasmas with a wide range of temperatures, from 0.0005 eV to 200 eV. The extremely low temperatures are accessible because the electrons cool by cyclotron radiation. A single electron in free space radiates energy with an e-folding time of $\tau_{rad} = 387/[B(\text{kG})]^2$ sec [1]; at 40kG, $\tau_{rad}$= 0.23 sec. Electrons in CV radiate energy at a slightly slower rate, presumably because the conducting cylinders act somewhat like a waveguide; the experimentally measured value of $\tau_{rad}$ is 0.29 sec at $B = 40$ kG [1]. The plasma can cool to arbitrarily low temperatures without recombining because there are no ions present. CV plasmas can also be heated to hundreds of eV without ionizing background gas because the cryopumping by the liquid helium produces an extemely good vacuum.

The temperature of the plasma parallel to the magnetic field, $T_{\|}$, is measured by ramping the dump cylinder voltage to ground slowly compared to the mean elec-

tron axial bounce frequency, $\overline{f_B}$. As the dump ring voltage is ramped, the potential barrier which confines the electrons is decreased. This barrier is weakest on the axis of the trap. The more energetic electrons escape before those with less energy, and are collected on P1. The voltage on P1 and the dump ring voltage are simultaneously digitized at 1MHz. The parallel temperature is determined by measuring the number of electrons which escape as a function of the dump ring voltage. Beck [1] calculated the rate at which electrons escape assuming that their parallel velocity distribution is a Maxwellian and the escaping electrons come from the tail of the Maxwellian. This rate is given by

$$-\frac{1}{e^2}\frac{d}{dV_c}\log(Q_1) \approx \frac{1.05}{kT_{||}}. \tag{2.14}$$

The right hand side of this equation is an approximation to an asymptotic expansion. The first term in this expansion is $1/kT_{||}$, and the second term is at most 10% of the first term. Hence, the asymptotic expansion can be approximated to within 5% by $1.05/kT_{||}$.

Typically, the measurements of 4 shots are averaged; temperature measurements are repeatable to within 10%. The theory and operation of the temperature measurement system are well described by Beck and Eggleston [14]. Radial energy transport is discussed in Section 2.7.

Only the parallel temperature, $T_{||}$, can be measured on the CV apparatus. While the perpendicular temperature, $T_{\perp}$, is not measureable, the two temperatures equilibrate through electron-electron collisions. As long as the equilibration rate between the two temperatures, $\nu_{\perp||}$, is larger than the rate of change of either $T_{\perp}$ or $T_{||}$, the two temperatures will be near a common value, $T$, i.e. $T_{\perp} \approx T_{||} \equiv T$. This was true for nearly all of the experiments described in this thesis.

### Low Temperature Considerations

The lowest temperature measureable with this method is limited by the minimum number of escaping electrons which can be measured, which is limited by the noise in the measurement circuit. This noise is primarily due to microphonics in the leads from the central collector P1 to the first stage amplifier. For this reason, the first stage amplifier is located inside the cryostat, in order to shorten these leads.

Even so, to measure temperatures lower than 0.05 eV on a typical CV plasma requires additional analysis of the collected electron signal. In order to do this, the digitized $Q_1$ and dump ring voltage signals are fed into a program which models the escape of electrons from over the potential barrier, including the effects of the change in space charge potential and the loss of electrons with velocities which are not in the tail of the Maxwellian distribution. This process is more time consuming than the normal measurement process, but it enables temperature measurements down to 0.003 eV.

## 2.6 Plasma Heating

The thermal energy of the plasma can increase in a variety of ways. The most ubiquitous method is Joule heating from the radial transport of electrons through the plasma's radial electric field. Because the electrostatic energy of the plasma is much larger than the thermal energy, a small amount of radial transport can cause significant heating.

A number of the experiments described in this thesis required that the plasma be actively heated. A simple way to accomplish this is to modulate the length of the plasma by applying a sinusoidally varying voltage to one of the rings near the end of the confinement region. (The L4 cylinder in Figure 2.2 was typically used.) If the modulation frequency $f_{mod}$ is small compared to the mean electron bounce

frequency, $\overline{f_B}$, but large compared to the anisotropic temperature equilibration rate, $\nu_{\perp\|}$, then the parallel temperature varies as if the the plasma were a 1-D ideal gas, i.e. $T_{\|}L_p^2$ remains a constant. Electron-electron collisions attempt to equilibrate $T_{\|}$ with $T_{\perp}$, causing the modulation $T_{\|}$ to be out of phase with the applied voltage. This results in net work being done on the plasma, raising both $T_{\perp}$ and $T_{\|}$, as shown by Beck [1].

I have found experimentally that if $f_{mod} > 0.3\overline{f_B}$, the heating rate is as much as 2 orders of magnitude greater than if the plasma length is modulated adiabatically, i.e. $f_{mod} \ll \overline{f_B}$. Much smaller applied voltages can then be used to heat the plasma, giving smaller perturbations to the plasma length and density. This non-adiabatic heating is discussed in Appendix A.

For many experiments, a stable plasma temperature is desired. This can be achieved if the cooling of the plasma through cyclotron radiation is balanced by Joule heating and active heating. This requires that $\nu_{\perp\|} \gg 1/\tau_{rad}$, so that $T_{\perp}$ and $T_{\|}$ equilibrate much faster than $T_{\perp}$ decreases through radiation or $T_{\|}$ increases by the heating processes described here. This condition holds for most of the experiments I describe in this thesis. By adjusting the amplitude of the applied voltage, the plasma temperature can be set to any desired value.

## 2.7 Energy Transport

The major shortcoming of the temperature diagnostic on CV is that it only measures the temperature at the center of the plasma. Beck [1] showed that over 90% of the electrons that are measured originate within $4\lambda_D$ of the plasma axis. At a typical temperature of $T = 0.1$ eV and density of $n = 5 \times 10^9$ cm$^{-3}$, the Debye length is $\lambda_D = 0.0033$ cm, and $4\lambda_D/R_p \approx 0.05$ for a typical plasma radius of $R_p/R_w = 0.05$. To analyze my data, I assume that the plasma has uniform temperature; e.g.

to calculate the distribution of electrons along the field lines using Equation 2.10 and Equation 2.11, or to compare to rotational pumping theory. It is therefore worthwhile to examine the validity of this assumption in relation to the cross-field transport timescales of interest.

The bounce motion of the electrons phase mixes any temperature variations along the field lines on a time scale of $\overline{f_B}^{-1}$. Collisions between the electrons then equilibrate $T_\perp$ and $T_\parallel$ and bring the plasma to local thermal equilibrium along each field line on a time scale of $\nu_{\perp\parallel}^{-1}$. Previous experimental [2, 31] and theoretical [22, 27] work has shown that the anisotropic temperature equilibration rate, $\nu_{\perp\parallel}$, can be written as

$$\nu_{\perp\parallel} = \frac{8\sqrt{\pi}}{15}\, nb^2\bar{v}\, I(r_c/b), \tag{2.15}$$

where $b \equiv e^2/T$ is the distance of closest approach, and $r_c = \bar{v}/\omega_c$ is the mean cyclotron radius. For $r_c \gg b$, the function $I(r_c/b)$ is the Coulomb logarithim, i.e. $I \equiv \ln(r_c/b)$. Here, $r_c$ is the maximum and $b$ is the minimum impact parameter for an electron-electron collision. For $r_c \ll b$, the electrons cannot get close enough together to exchange perpendicular and parallel energy, causing $I$ to decrease exponentially with decreasing $r_c/b$. Thus, at a given density and magnetic field, $\nu_{\perp\parallel}$ is a maximum for $r_c \approx b$. For the experiments described in this thesis, $100 < \nu_{\perp\parallel} < 6 \times 10^5$ sec$^{-1}$. Thus, the plasma reaches local thermal equilibrium in $z$ in less than 10 msec.

Temperature equilibration is presumably also rapid in the $\theta$ direction, due to shears in the $\mathbf{E} \times \mathbf{B}$ rotation profile [29, 30]. Consider electrons which are originally at the same $r$ and $\theta$. Over a time $\tau_\theta$ they will diffuse in radius a distance $\delta r$, and so will also spread out over an angle $\delta\theta \approx 2\pi\tau_\theta(\partial f_E/\partial r)\delta r$. Setting $\delta\theta = 2\pi$ and $\delta r^2 = D_r\tau_\theta$, where $D_r$ is the radial diffusion coefficient given below in Equation 2.17, gives the equilibration time in $\theta$ as

$$\tau_\theta \sim \left[D_r^{1/2}(\partial f_E/\partial r)\right]^{-2/3}. \tag{2.16}$$

For a typical CV plasma, $\tau_\theta < 10$ msec, similar to the equilibration time in $z$.

At the present time there is no direct experimental measurements of radial energy transport in pure electron plasma. A lower bound can be estimated from collisional transport theory, which gives a radial diffusion coefficient of

$$D_r \approx \nu_{ee} r_c^2. \tag{2.17}$$

Here, $r_c$ is the radial step size during a collision and the electron-electron collision rate is given by

$$\nu_{ee} \approx n b^2 \bar{v} \ \ln(\lambda_D / b). \tag{2.18}$$

This is nearly the same expression as that for $\nu_{\perp\|}$ when $r_c > b$, except that $\lambda_D$ replaces $r_c$ in the Coulomb logarithim. The reason for this substitution is that, as shown by O'Neil [45, 46], collisions with impact parameters greater than $r_c$ but less than $\lambda_D$ can cause diffusion without equilibrating $T_\|$ and $T_\perp$. Defining the radial energy transport time by $\tau_r \approx R_p^2/D_r$, gives 9 sec $< \tau_r <$ 52 sec for a typical CV plasma at temperatures from 0.001 eV to 10 eV and $B = 40$ kG.

The arguments given above show that the plasma temperature should be relatively uniform in the $z$ and $\theta$ directions. The theoretical estimate of radial energy transport, however, does not rule out radial temperature gradients, especially for plasmas which are wider or denser than typical plasma I have considered here ($n = 5 \times 10^9$ cm$^{-3}$ and $R_p/R_w = 0.05$). Thus, the assumption that the temperature is uniform is not entirely valid and may be responsible for some disagreements between my data and the rotational pumping theory.

## 2.8 Symmetrization of the Density Profile

In measuring the plasma density profile I assume that it is symmetric about its own axis. This assumption is valid, as previous researchers have shown that the

symmetrization rate is much faster than the transport rates which I discuss in this thesis.

Huang [29, 30] studied the relaxation of turbulence in the $\mathbf{E} \times \mathbf{B}$ flow in the plasma. He found that density flucuations in $\theta$ shear out within 100 $\mathbf{E} \times \mathbf{B}$ rotations of the plasma column. Vortices in the $\mathbf{E} \times \mathbf{B}$ flow which are strong enough to resist the shear may last for 10-100 times longer, but for a typical CV plasma this time scale is still less than 10 msec.

Coherent modes may last much longer than the random turbulence; e.g. diocotron modes may last for many plasma rotations. However, the high mode number ($m \geq 2$) modes damp through a spatial Landau-type mechanism [4, 8, 52]. Mitchell [39] also showed that these modes can decay into lower $m$ modes through "beat-wave" damping. For a typical CV plasma, the $m \geq 2$ modes are estimated to damp in less than 100 msec. The $m = 1$ diocotron mode cannot Landau damp or decay into a lower $m$ mode; however, for small amplitudes ($D \ll R_w$) the plasma should be essentially symmetric around its own axis, as shown by Fine [18].

## 2.9 Alignment of the Magnetic Field

Proper alignment of the magnetic field with the conducting cylinders is crucial in running the CV apparatus. It is implicitly assumed in both density and temperature measurements and in the calculation of the 3D density and potential profiles.

The standard alignment procedure on Penning-Malmberg traps is due to Fine [16], who demonstrated that misalignment between the magnetic field and the conducting cylinders can result in increased radial transport. Fine incremented the magnetic field angle until he found the value which caused the least radial transport. This procedure is not feasible on the CV device, as shown by Figure 2.6. The plot

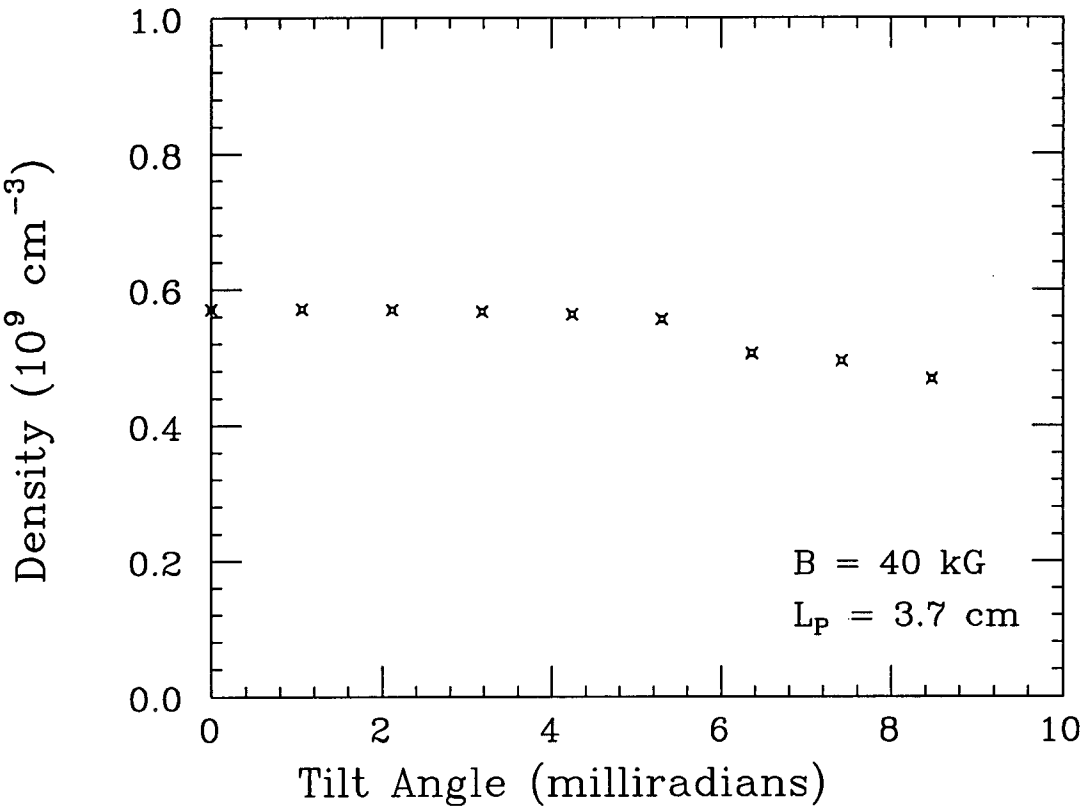


**Figure 2.6:** Final central density after 30 sec of magnetic tilt. The density decreases less than 20% even at a tilt angle of 8 mrad.

shows the central density of a plasma as a function of the magnetic field tilt angle. The magnetic field was held at the tilt angle shown during the 30 second confinement period, but was properly aligned during the injection and dump periods. The change in central density was at most about 20% for the largest tilt angles, which limits the precision of the magnetic field alignment to several milliradians. This lack of transport from radial tilt is qualitatively consistent with Fine's results, who measured a transport rate that scaled as

$$\frac{1}{n}\frac{dn}{dt} \propto B^{-2}L_p^q \tag{2.19}$$

where $q > 2$. This scaling predicts very slow transport due to magnetic tilt in the CV apparatus, which has magnetic fields 100 times greater than Fine's EV device,

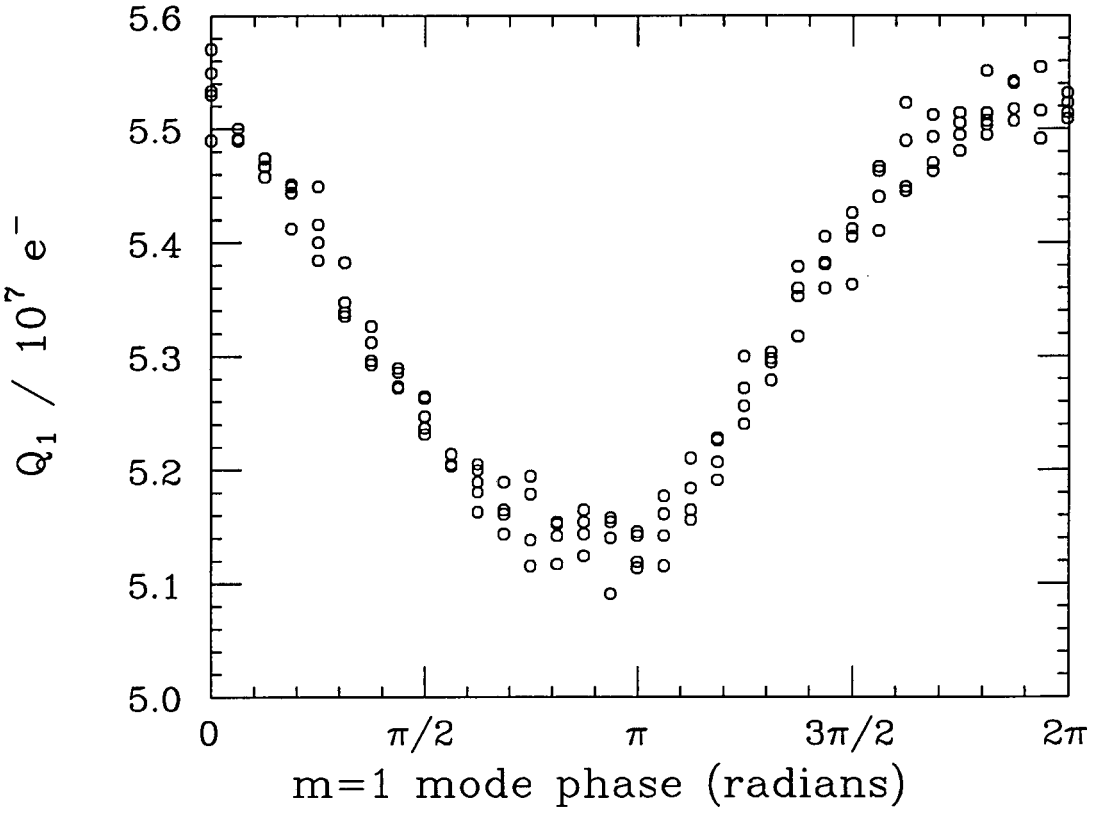


**Figure 2.7:** The number of electrons dumped on the central collector, P1, varies about 6% with the phase of the diocotron mode, indicating the magnetic field is not aligned with the collectors.

and plasma lengths several times shorter.

While the slowness of the transport caused by magnetic misalignment is fortuitous in terms of confining the plasma, it neccesitates a new method of aligning the magnetic field. The method which I developed uses the $m = 1$ diocotron mode and the azimuthal symmetry of the P1 collector. The plasma is dumped while the diocotron mode is present. If the field is misaligned, the axis of the column's orbit will not be the same as the trap's axis of symmetry, and the number of electrons dumped on the central collector will depend on the phase of the $m = 1$ diocotron mode, as shown in Figure 2.7. The magnetic field is aligned by finding the tilt angle for which the number of electons dumped on the central collector is independent

of phase. The magnetic field can be aligned in this way to within a fraction of a milliradian.

# Chapter 3

# Anomalous Transport

## 3.1 Overview

In this chapter, I present measurements on the radial transport of electrons in the CV trap due to the inherent asymmetries of the trap. The mean square radius of the plasma is constrained by the conservation of its angular momentum; radial transport arises because azimuthal asymmetries exert a torque on the plasma. Since the form of these asymmetries is not known, radial expansion of the column due to inherent asymmetries is refered to as "anomalous" transport.

I have found that for high enough temperatures, the anomalous transport rate in the CV trap decreases with temperature. The dependence on temperature has not previously been observed, and can be quite strong. However, at temperatures low enough that the $\mathbf{E} \times \mathbf{B}$ rotation frequency of the plasma, $f_E$, is larger than the mean electron bounce frequency, $\overline{f_B}$, I find that the transport rate is independent of temperature. The transition between these two temperature regimes is observed to occur where $\overline{f_B} \approx f_E$. I have also observed that the transport rate increases with plasma density, and decreases with magnetic field. The magnetic field dependence in the CV trap is stronger than has been observed in other pure electron plasma traps.

In comparing the CV anomalous transport rates to those in similar devices, I find that the value of $f_E/\overline{f_B}$ is a good indicator of the loss time for a wide range of

plasma parameters. This is consistent with the constraints placed on the expansion of the column by conservation of energy and by adiabatic invariants associated with the kinetic energy of the electrons. In order for the plasma to expand, it must dissipate electrostatic energy into thermal energy. This requires the breaking of the adiabatic invariants, which becomes easier as $f_E/\overline{f_B}$ increases.

While the observed scalings of the transport rate with plasma parameters are consistent with theoretical constraints, the actual mechanism by which the plasma expands is unknown. One possible mechanism is single particle resonant transport. The data shows some agreement with resonant particle transport theory, but is not clean enough to establish resonant particle transport as the primary transport process.

## 3.2 Angular Momentum and Torques

Pure electron plasmas have exceptional confinement properties compared to neutral plasmas. The single sign of charge allows the use of static voltages to confine the plasma along the magnetic field, eliminating the need for curvature in the magnetic field lines. As long as the voltage barrier is high enough, axial confinement is energetically ensured, and the electrons can only escape radially across the magnetic field.

The radial expansion of the plasma is constrained by the conservation of the angular momentum of the electrons and fields [43]; the plasma can expand radially only if external torques act to reduce the total angular momentum, $P_\theta$. This can be seen in the expression for the total canonical angular momentum of the pure electron plasma:

$$P_\theta = \int d^3r\, n(m_e\mathbf{v} - \frac{e}{c}\mathbf{A}) \cdot r\hat{\theta} = \int d^3r\, nm_e(v_\theta r - \omega_c\frac{r^2}{2}), \tag{3.1}$$

where the vector potential for the uniform, axial magnetic field is $\mathbf{A} = \frac{1}{2}Br\hat{\theta}$. For

a CV plasma, the inertial part of angular momentum is usually a factor of $\sim 10^{-4}$ smaller than electromagnetic part. Equation 3.1 can then be written as

$$P_\theta \approx \frac{m_e \omega_c}{2} N( R_w^2 - \langle r^2 \rangle ) \tag{3.2}$$

where $\langle r^2 \rangle$ is the mean square radius of the plasma. The $R_w^2$ term is due to the positive image charges on the conducting walls; it is a constant as long as $N$ is conserved.

For constant $N$, the mean square radius of the plasma is a constant in the absence of external torques which change $P_\theta$. Note that this is not true in a neutral plasma, because the electromagnetic part of each particle's angular momentum is proportional to its charge, and positive and negative charges are distributed equally.

Previous work by Malmberg and Driscoll [37] showed that collisions between the electrons and a stationary, neutral background gas induce a drag on the plasma that increases its mean square radius. They found that the rate of expansion of the plasma column is proportional to the neutral pressure and decreases with the magnetic field as $B^{-2}$. Their measurements are well explained by theory [9].

When the neutral pressure is sufficiently low, transport caused by electron-neutral collisions becomes negligible. The plasma expansion is instead due to some anomalous process which is independent of pressure. I use the word "anomalous" because the source of the external torques is not known. They are believed to be caused, however, by small azimuthal asymmetries in the confining magnetic or electric fields. These asymmetries are present in all nonneutral plasma devices, but are minimized by careful engineering and the use of non-magnetic materials in the construction of the trap.

The first measurements of anomalous transport in a Penning-Malmberg trap were performed by Driscoll and Malmberg [12] on the V′ apparatus. They defined the "mobility time", $\tau_m$, as the time for the central density of the plasma to decrease by

1/2. They found that $\tau_m$ scaled as $(L_p/B)^{-2}$ over 5 decades in the parameter $L_p/B$. Subsequent work on the EV apparatus [11] showed the same scaling with $L_p/B$. It also demonstrated that field asymmetries play an important role in the transport. By carefully minimizing asymmetries in the construction of the EV apparatus, transport rates were reduced by a factor of 20 compared to V'.

Here, I define $\tau_m$ as the confinement time at which the amount of charge dumped on the central collector P1 is 1/2 of its original value. Since the signal on P1 averages over a sizeable portion of the density profile, my definition of $\tau_m$ largely ignores $P_\theta$ conserving radial transport. The mobility time for a given plasma is measured by incrementing the confinement time over many shots. The plasma temperature is maintained at a constant level over the confinement time through the use of the non-adiabatic heating technique described in Section 2.6.

## 3.3 Temperature and Magnetic Field Dependence

### 3.3.1 Increase in $\tau_m$ at High Temperatures

I find that the mobility time $\tau_m$ usually increases with temperature. Figure 3.1 shows $\tau_m$ as a function of temperature at 5 different magnetic fields. At $B = 4$ kG, the mobility time increases by 3 orders of magnitude as the temperature is increased by a factor of 50, from $T = 2$ eV to $T = 100$ eV. As the magnetic field increases, $\tau_m$ increases less strongly with temperature. At $B = 64$ kG, $\tau_m$ increases only 1 order of magnitude as $T$ increases by a factor of 50. The dashed lines show scalings of $\tau_m \propto T^2$ and $\tau_m \propto T^1$ for comparison.

The increase in $\tau_m$ with temperature is at first counter-intuitive: more energetic electrons are better confined. However, it is consistent with several fundamental ideas about radial transport.

1. The kinetic energy of the electrons increases with temperature, whereas the

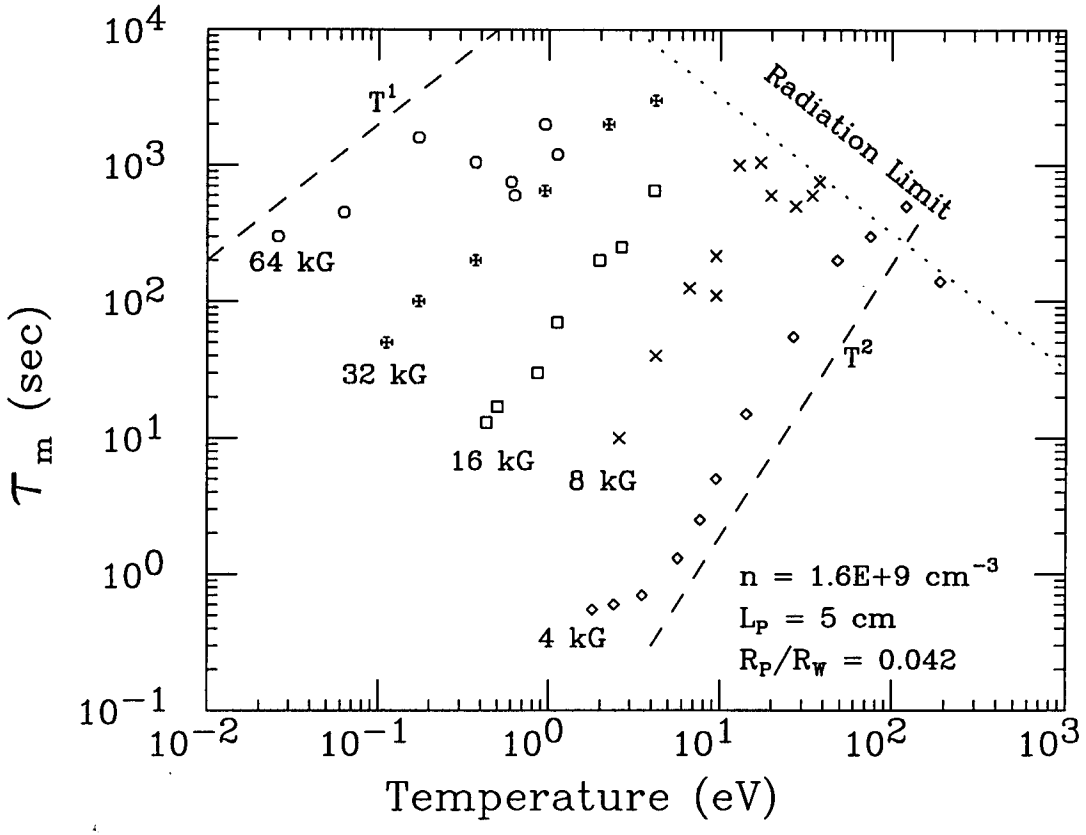


**Figure 3.1:** Increase in $\tau_m$ with temperature at 5 different magnetic fields. The dashed lines show $T^1$ and $T^2$ scalings for comparison. The dotted line shows the upper limit put on $\tau_m$ by cyclotron radiation.

strength of the field asymmetries does not. Thus, as the temperature is increased, the field asymmetries presumably make smaller perturbations to the orbits of the electrons. Also, high energy electrons are less likely to be trapped in any local potential wells created by field asymmetries.

2. The electron-electron collision rate, $\nu_{ee}$, and the collisional temperature equilibration rate, $\nu_{\perp\parallel}$, both decrease strongly with temperature for the temperature range shown in Figure 3.1. Collisional transport mechanisms, such as the rotational pumping discussed in Chapter 4, will be weaker at higher temperatures.

3. The plasma Debye length, $\lambda_D$, increases with temperature. This may weaken

transport from collective effects. However, I do not observe any change in the the dependence of $\tau_m$ on $T$ when $\lambda_D$ becomes comparable to the plasma radius $R_p$. (In Figure 3.1, $\lambda_D = R_p$ at $T = 12$ eV.)

The increase in $\tau_m$ with temperature could conceivably be due to some non-linear interaction between the plasma and the sinusoidal voltages used to heat it. Paul traps, for instance, use RF voltages to confine a plasma without a magnetic field. I do not believe that this is the case for several reasons. First, the frequency and amplitude of the applied voltage can be varied while maintaining the same plasma temperature. The value of $\tau_m$ is observed to depend on the temperature, not the amplitude of the applied voltage. Second, for the first 7 points in Figure 3.1 at $B = 4$ kG, $\tau_m$ is less than the radiative cooling time $\tau_{rad}$. The temperature of those plasmas were set by applying a voltage burst at the beginning of the confinement time; continual active heating was not required to increase $\tau_m$. Finally, the decrease in radial transport with temperature has recently also been observed on a pure $Mg^+$ ion plasma [58]. The ion plasma was cooled by ion-neutral collisions and heated by driving the cyclotron motion of the ions. The common factor between these two experiments is the increase in $\tau_m$ with temperature.

The dotted line in Figure 3.1 is an estimate of the mobility time $\tau_m$ if cyclotron radiation is the only source of angular momentum loss. In Appendix C, I show that cyclotron radiation lowers the angular momentum as well as the perpendicular energy of the electrons. However, actively heating the plasma increases only its parallel energy, not its angular momentum, because the applied voltage is azimuthally symmetric. As electron-electron collisions equilibrate $T_\perp$ and $T_\parallel$, they must exchange angular momentum between the electrons and the fields in order to conserve $P_\theta$. Therefore, the loss of angular momentum through cyclotron radiation must be accompanied by a radial expansion of the column. This puts an upper limit

on $\tau_m$ of

$$\tau_m \approx \frac{\tau_{rad}}{12}\left(\frac{R_p}{r_c}\right)^2 \tag{3.3}$$

where $r_c$ is the mean electron cyclotron radius. The transport due to cyclotron radiation is independent of magnetic field, since $\tau_{rad}$ and $r_c$ are both proportional to $B^{-2}$, and is normally much slower than the transport from asymmetries. However, radiation transport is important at the highest temperatures in Figure 3.1, as is evident by the decrease in $\tau_m$ at $B = 4$ kG and $T = 220$ eV.

### 3.3.2 Increase in $\tau_m$ with Magnetic Field

Figure 3.2 shows the data from Figure 3.1 plotted against magnetic field at 5 different temperatures. The dotted lines are simply to guide the eye. The dependence of $\tau_m$ on magnetic field is comparable to $\tau_m \propto B^4$, as shown by the dashed line. This is a much stronger dependence than previously observed, and may indicate that the transport processes in this parameter regime are qualitatively different than those in the EV and V′ apparatuses.

The weakening of the dependence of $\tau_m$ on $T$ with increasing magnetic field is responsible for the rightward bend in the data in Figure 3.2. The reason for this weakening is not known. It may be that different transport processes are dominant at different magnetic fields, or it may be a systematic error. As the temperature and magnetic field are varied, it is not possible to keep the plasma length and density profile exactly constant. Also, $\tau_{rad}$ decreases with magnetic field, which requires that stronger active heating be used. Since the radial energy transport rate presumably also decreases with magnetic field, radial temperature gradients are more likely to exist at higher magnetic fields. If the center of the plasma is heated more than the edge, the measured temperature may be larger than the average plasma temperature.

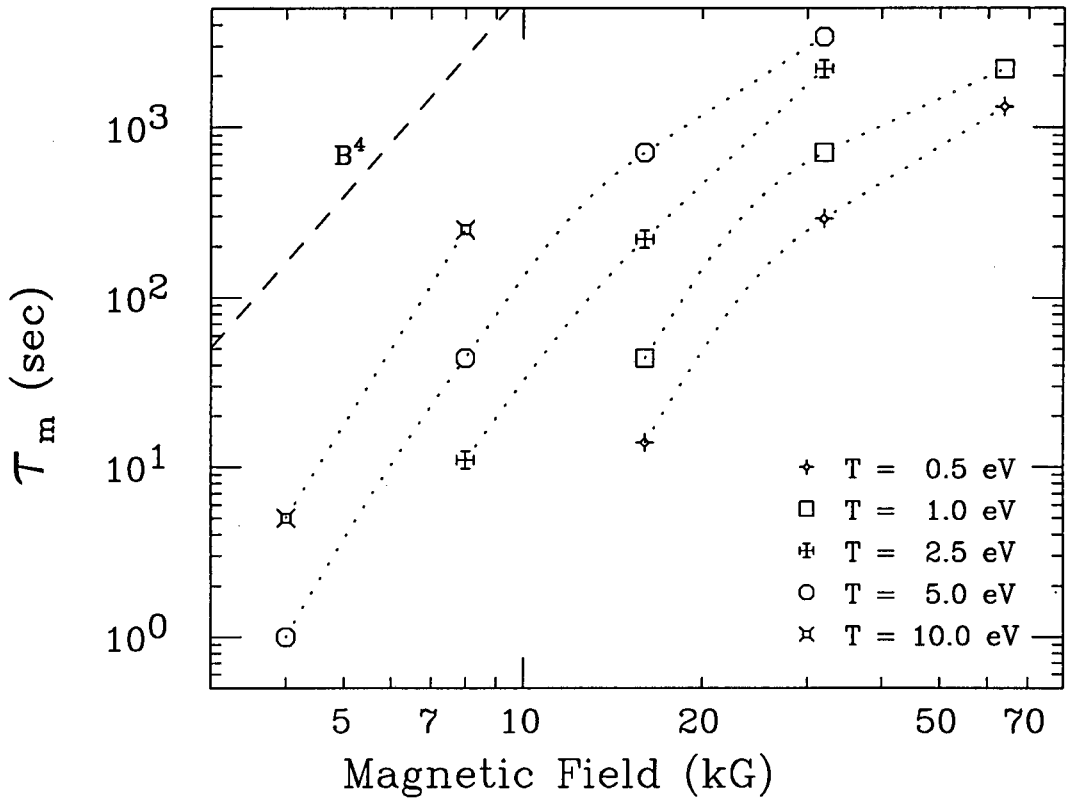


**Figure 3.2:** The same data as Figure 3.1, plotted against magnetic field at 5 different temperatures. The mobility time increases strongly with magnetic field strength. The dotted lines are merely to guide the eye; the dashed line shows a scaling of $B^4$ for comparison.

### 3.3.3 Temperature Independence of $\tau_m$ at Low Temperatures

At sufficiently low temperatures, $\tau_m$ is observed to be indepedent of temperature. Figure 3.3 shows $\tau_m$ as a function of temperature for a short, high density plasma and for a plasma twice as long and one quarter the density. The magnetic field is 40 kG in both cases. The mobility time for the 2 plasmas increases approximately linearly with temperature for $T > 1$ eV, but is independent of $T$ at lower temperatures.

I have observed this transistion between the temperature dependent and tem-

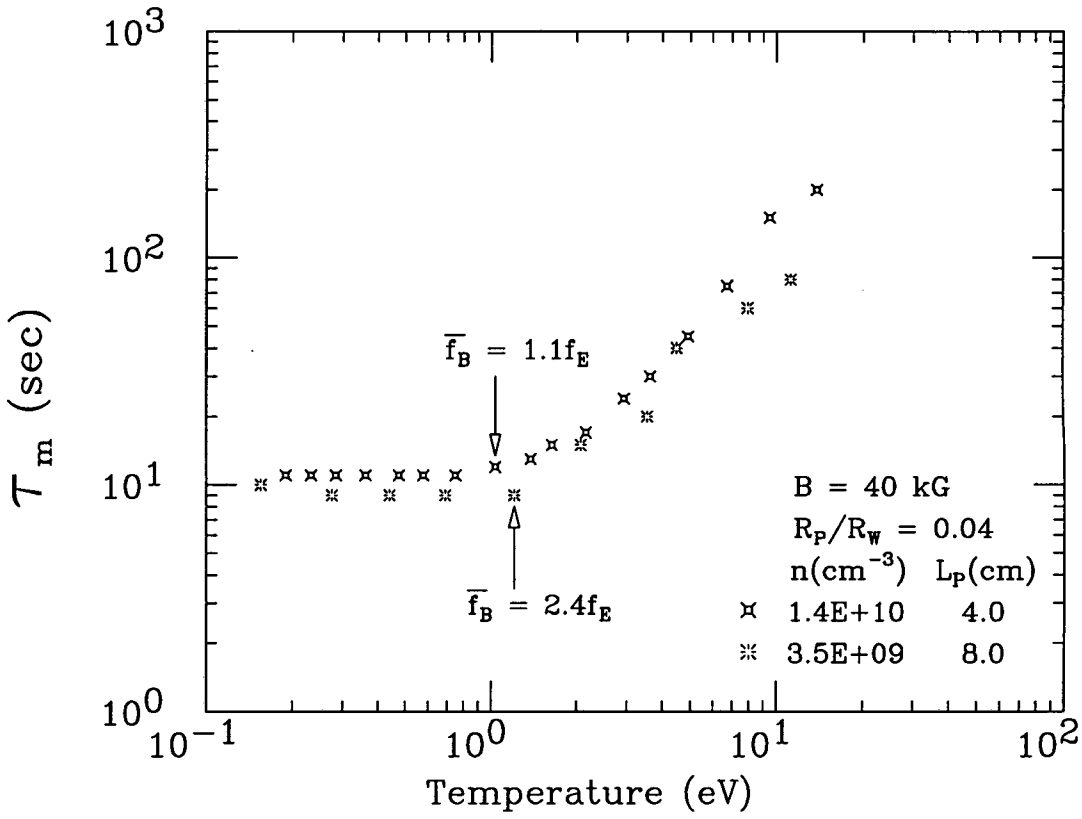


**Figure 3.3:** $\tau_m$ is independent of temperature when $f_E > \overline{f_B}$.

perature independent regimes in 8 different measurements of $\tau_m$ as a function of temperature, at densities from $5.5 \times 10^8$ to $1.4 \times 10^{10}$ cm$^{-3}$ and temperatures from 0.052 to 2.8 eV. The temperature at which the transistion occurs is observed to depend on density, magnetic field, and plasma length in such a way that $\tau_m$ is always independent of temperature when $f_E > \overline{f_B}$. For instance, in Figure 3.3, the transition occurs at $f_E/\overline{f_B} \approx 0.9$ for the higher density plasma and at $f_E/\overline{f_B} \approx 0.4$ for the lower density plasma. In Figure 3.1, $f_E$ is greater than $\overline{f_B}$ only for the first two points at $B = 4$ kG. This presumably explains why only the $B = 4$ kG data exhibits a transition to the temperature independent regime, although, in general, the transition is observed at values of $f_E/\overline{f_B}$ as small as 0.3. The reason for the transition is not known; it may mark the boundary between different parameter regimes

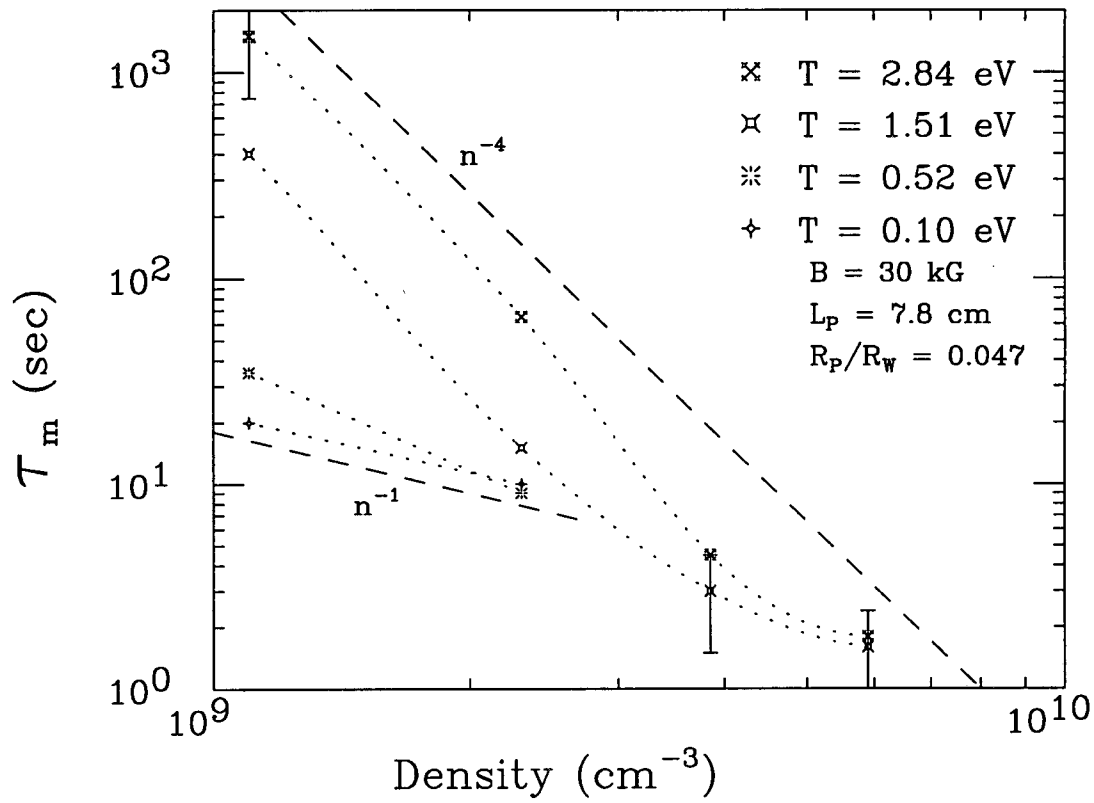


**Figure 3.4:** $\tau_m$ decreases strongly with density. The strength of the dependence decreases with temperature; the dashed lines show $n^{-1}$ and $n^{-4}$ scalings for comparison. The dotted lines are merely to guide the eye. The points with error bars were extrapolated from lower or higher temperatures.

with different transport processes.

## 3.4 Density Dependence

While $\tau_m$ usually increases with temperature and magnetic field, it decreases with density, as shown in Figure 3.4. The mobility time is shown as a function of density at 4 different temperatures. At the highest temperature of 2.84 eV, $\tau_m$ decreases by 3 orders of magnitude, from 1500 sec to 1.8 sec, as the density is increased by a factor of 5. The dependence of $\tau_m$ on density is weaker at lower temperatures; at $T = 0.1$ eV, increasing the density from $1.1 \times 10^9$ cm$^{-3}$ to $2.3 \times 10^9$ cm$^{-3}$ only de-

creases $\tau_m$ by a factor of 2. The dashed lines in Figure 3.4 show scalings of $\tau_m \propto n^{-4}$ and $\tau_m \propto n^{-1}$ for comparison. The dotted lines are simply to guide the eye.

Unlike the increase in $\tau_m$ with temperature, the decrease in $\tau_m$ with density is intuitively expected; it is harder to confine many electrons than a few. It is consistent with several fundamental plasma physics concepts:

1. The plasma's self electric field is proportional to its density. A higher density means faster $\mathbf{E} \times \mathbf{B}$ drifts and a larger radial force on each electron.

2. The electron-electron collision rate, $\nu_{ee}$, and the collisional temperature equilibration rate, $\nu_{\perp\parallel}$, both increase linearly with density. Collisional transport mechanisms should be stronger at higher densities.

3. The plasma Debye length decreases with density. This may strengthen transport from collective effects.

The minimum temperature at each density is limited by the Joule heating caused by the radial expansion. The higher the plasma density, the faster it expands and the more electrostatic energy is released as it does. The points with error bars in Figure 3.4 were not accessible experimentally and have been extrapolated from values of $\tau_m$ measured at higher or lower temperatures. The large error bars show the factor of 2 uncertainty in the values of $\tau_m$ at these points.

## 3.5 Comparison with Previous Experiments

Very long mobility times are predicted for CV plasmas if the EV and V′ scalings with neutral gas pressure and $L_p/B$ are extrapolated to the CV parameter regime. The vacuum in CV is estimated to be superior to that in the EV and V′ machines, due to the cryopumping produced by the liquid helium. Furthermore, the parameter $L_p/B$ is orders of magnitude smaller in CV than in EV and V′. However,

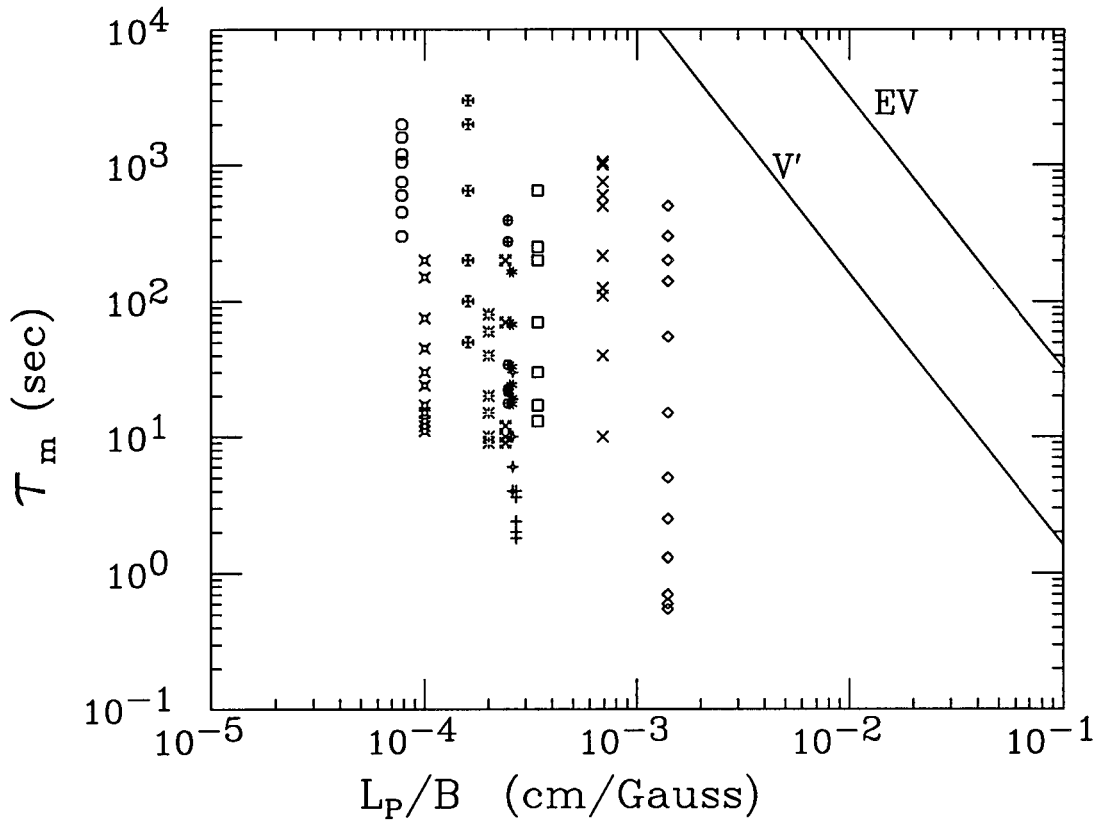


**Figure 3.5:** CV data plotted gainst $L_p/B$. The wide spread in $\tau_m$ at each $L_p/B$ is due to variations in temperature and magnetic field. Each symbol corresponds to a different data set in which $\tau_m$ was measured as a function of temperature. The solid lines show the $(L_p/B)^{-2}$ scalings obtained on the EV and V′ devices.

the mobility times in CV are comparable to EV and V′, due to the higher densities and colder temperatures in CV.

It is instructive to compare my measurements of $\tau_m$ with the measurements made by Driscoll and Malmberg on the V′ and EV apparatuses. Figure 3.5 shows all the data from Figures 3.1 - 3.4 plotted against the parameter $L_p/B$. The solid lines show the $(L_p/B)^{-2}$ scalings of $\tau_m$ obtained on EV and V′. The large vertical spread at each value of $L_p/B$ reflects the variation of $\tau_m$ with temperature and density. In contrast, the EV and V′ plasmas all had the same density, $n \sim 10^7$ cm$^{-3}$, and the same temperature, $T \sim 1$ eV.

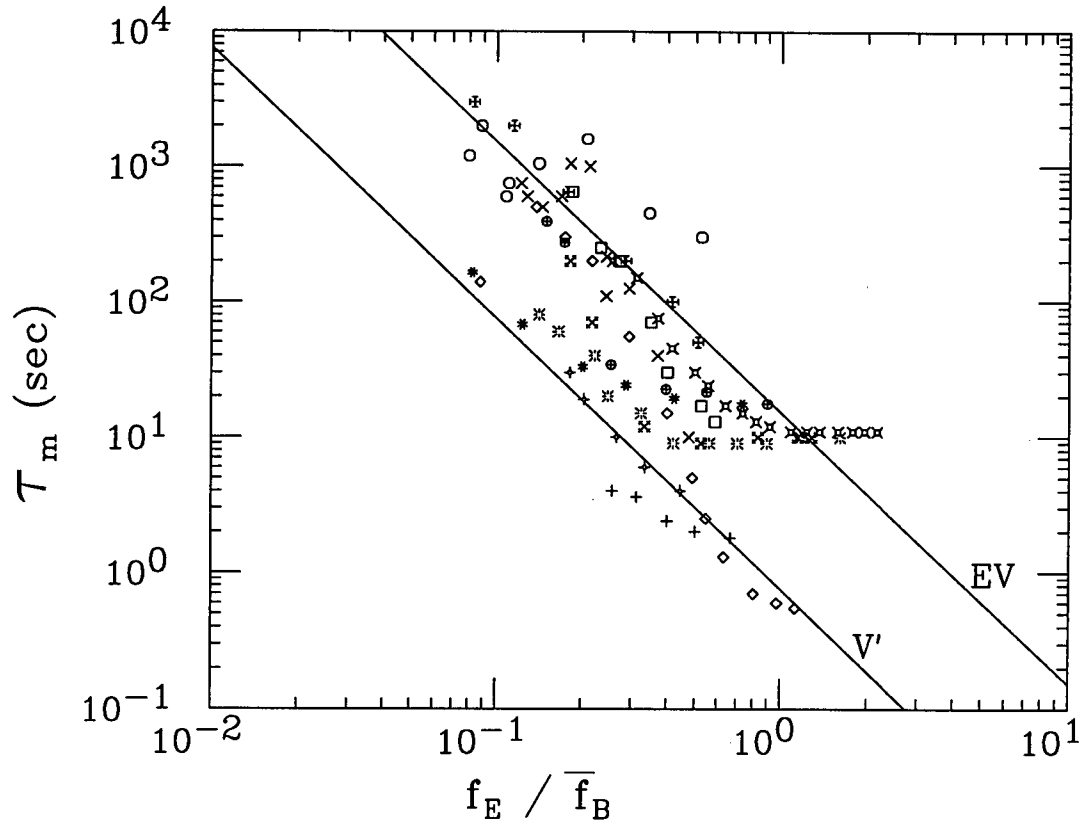


**Figure 3.6:** The CV data coincides with the EV and V′ data when plotted against $f_E/\overline{f_B}$. Some data sets show $\tau_m$ to be independent of $f_E/\overline{f_B}$; this is due to the temperature independent transport shown in Figure 3.3.

In order to compare the CV data to the EV, V′ data, I need a dimensionless parameter which is proportional to $L_p/B$ and also increases with $n$ and decreases with $T$. The ratio $f_E/\overline{f_B}$ satisfies these conditions, and is also an important parameter in resonant particle transport theory. Figure 3.6 shows all of the data in Figure 3.5 plotted against $f_E/\overline{f_B}$. The CV data points fall largely between the two solid lines which show the EV and V′ scalings. These lines give $\tau_m = 0.76\,(f_E/\overline{f_B})^{-2}$ for the V′ data and $\tau_m = 15.2\,(f_E/\overline{f_B})^{-2}$ for the EV data. Now, $(f_E/\overline{f_B})^{-2}$ is proportional to $(L_p/B)^{-2}(T/n^2)$. While my data exhibits a temperature dependence in the scaling of $\tau_m$ with $n$ and $B$, I find that $\tau_m \propto (L_p/B)^{-2}(T/n^2)$ is certainly within the range of scalings I observe. Therefore, while $(f_E/\overline{f_B})^{-2}$ may not be the proper

scaling in all parameter regimes, it does have the advantage of being a single dimensionless parameter which can be used to roughly predict the effectiveness of radial confinement over a broad range of parameter regimes. Recently, measurements of $\tau_m$ on two new machines at UCSD, IV and CAMV, have also exhibited rough $(f_E/\overline{f_B})^{-2}$ scalings which are also close to EV and V′.

## 3.6 Comparison with Theory

### 3.6.1 Constraints

The radial expansion of the plasma column is subject to several theoretical constraints. One, the non-conservation of angular momentum, is discussed in Section 3.2. The total angular momentum of the plasma, $P_\theta$, must decrease in order for the column to expand [43].

Another constraint is the limitations of $\mathbf{E} \times \mathbf{B}$ drift dynamics. $\mathbf{E} \times \mathbf{B}$ flows are incompressible and conserve the electrostatic energy of the plasma [10], while the radial transport studied here is compressible and decreases the electrostatic energy. Hence, some mechanism besides $\mathbf{E} \times \mathbf{B}$ drift dynamics must be involved.

Since the field asymmetries responsible for the transport are presumably time-independent, the total energy of the plasma is also conserved, aside from losses due to cyclotron radiation. Since the energy of the plasma is divided between only two components, electrostatic and thermal, any expansion of the plasma column must be accompanied by an increase in the thermal energy.

Finally, as noted by O'Neil [47], the increase in the thermal energy of the plasma is constrained by 2 adiabatic invariants which constrain the kinetic energy of each electron. These invariants are

1. $J_\perp = m_e v_\perp^2 / B^2$, associated with the cyclotron motion of an electron, and

2. $J_{||} = \oint dz\, m_e v_{||}$, associated with the bounce motion of an electron.

In order for the kinetic energy of an electron to increase, one of these adiabatic invariants must be broken.

If the cyclotron and bounce motions of an electron are faster than any other plasma motions, only collisions can break the two adiabatic invariants. In the absence of collisions, the extremely high cyclotron frequency of the electron, $\omega_c \sim 10^{12}$ Hz, ensures that $J_\perp$ remains invariant. However, $J_{||}$ is not an invariant if the $\mathbf{E} \times \mathbf{B}$ rotation frequency exceeds the bounce frequency of the electron or if high frequency plasma modes are present. In that case, the parallel kinetic energy of the electron can increase, providing a sink for the electrostatic energy released by radial transport.

The presence of these constraints partially explains the basic features of the observed scalings of $\tau_m$ with plasma parameters and hence with the parameter $f_E/\overline{f_B}$. Increasing the magnetic field or decreasing the density decreases the $\mathbf{E} \times \mathbf{B}$ rotation and plasma mode frequencies, which makes $J_{||}$ an adiabatic invariant for more electrons. Similarly, increasing the temperature or decreasing the plasma length increases the mean bounce frequency, which decreases the number of electrons for which $J_{||}$ is not a good adiabatic invariant. Also, bringing the plasma mode and mean bounce frequencies closer together increases Landau damping, which suppresses the growth of plasma modes. Finally, increasing $T$ and decreasing $n$ decreases the collisional temperature equilibration rate, so collisions are less likely to break the adiabatic invariants.

When the $\mathbf{E} \times \mathbf{B}$ rotation frequency $f_E$ is larger than the mean bounce frequency $\overline{f_B}$, the quantity $J_{||}$ is not an adiabatic invariant for most electrons. In that case, increasing $T$ should not inhibit the conversion of electrostatic energy into thermal energy. This is consistent with the observed independence of $\tau_m$ on $T$ when $f_E > \overline{f_B}$.

### 3.6.2 Resonant Particle Transport Theory

While the arguments made above partially explain the basic parameter scalings observed for anomalous transport, they do not explain the mechanism behind the transport. The lack of knowledge of the nature of the field asymmetries causing the transport makes estimating transport rates exceedingly difficult. However, the anomalous transport observed in Penning-Malmberg traps has long been considered to be some sort of resonant particle transport, so it is worthwile to examine the data from this perspective.

Single particle resonant transport theories [55, 56] assume that the field asymmetries can be reduced to Fourier components like

$$\delta\phi_{p,m}(r) = \delta\phi_0(r)\cos(p\pi z/L_p)\cos(m\theta). \tag{3.4}$$

The bounce and $\mathbf{E}\times\mathbf{B}$ rotation frequencies of a resonant particle satisfy the condition $mf_E = pf_B$. A particle which satifies the resonance condition continually traces out the same orbit. [This is analagous to the safety factor in a tokamak, $q$, being a rational number.] The orbit of such a particle is in phase with the variation in $\delta\phi$. This causes the particle to make large $\mathbf{E}\times\mathbf{B}$ excursions in the radial direction, $\Delta r$, during an orbit. The particle then continually executes this same orbit until an electron-electron collision knocks it out of resonance. The transport that results from the resonant particles is thus proportional to $(\Delta r)^2$. In contrast, non-resonant particles are not in phase with the field asymmetry, and do not continually trace out the same orbit. Hence, the field asymmetry causes these particles to take only small, random, radial steps. The increase in $P_\theta$ thus comes predominantly from the resonant particles, with collisions knocking particles in and out of resonance.

Obviously, the amount of transport that occurs is strongly dependent on the number of resonant particles. If the spread in particle energy is a Maxwellian, the bulk of the particles will have bounce frequencies around $\overline{f_B} = \bar{v}/(2L_p)$. If

$mf_E < p\overline{f_B}$, the number of resonant particles decreases as $T$ increases. This is consistent with the observed increase in $\tau_m$ with plasma temperature.

When $p\overline{f_B}$ becomes smaller than $mf_E$, the number of electrons resonant with a given Fourier component of a field asymmetry decreases as $T$ decreases. However, if the field asymmetry has multiple Fourier components, many possible resonances exist, and the total number of resonant particles does not neccesarily decrease. Thus, the observed $\tau_m \propto T^0$ scaling for $\overline{f_B} < f_E$ is not inconsistent with resonant particle transport theory.

Another important parameter in resonant particle transport theory is $\overline{f_B}/\nu_{ee}$, the ratio of the mean bounce frequency to the electron-electron collision rate. If this ratio is too small, collisions knock particles out of resonance before any transport occurs. Non-resonant transport processes should then be dominant. This may explain the transition between temperature dependent and independent transport discussed in Section 3.3.3. This transition occurs when $f_E/\overline{f_B} \approx 1$. For most CV plasmas, $\nu_{ee}$ is large when $f_E/\overline{f_B} \approx 1$. Thus, the transition to the temperature independent regime may indicate that the plasma is too collisional for resonant particle transport.

I have calculated $\overline{f_B}/\nu_{ee}$ at the transistion point for several sets of data and find that it is usually between 100 and 300. While knocking a particle out of resonance presumably requires much less then a full 90° collision, this ratio is probably still too high to rule out resonant particle transport in the temperature independent regime. Nevertheless, neither the theory nor the data are clean enough to definitively rule out the observed transition as one between resonant and non-resonant transport.

# Chapter 4

# Transport and Mode Damping from Rotational Pumping

## 4.1 Overview

In this chapter, I present measurements of the radial expansion of the plasma and the damping of the $m = 1$ diocotron mode from "rotational pumping" of a pure electron plasma column displaced from the trap's cylindrical axis. Rotational pumping is the collisional dissipation of the axial compressions caused by $\mathbf{E} \times \mathbf{B}$ rotation of the column through asymmetric confinement potentials. In these experiments, the confinement potentials appear asymmetric only because of the displacement of the column from the symmetry axis of the trap. A schematic of the end of the plasma column is shown in Figure 4.1. The confining potential is strongest on the axis of the trap and weakest near the grounded wall. Hence, the length of a tube of plasma is maximal when the tube is closet to the trap wall, and undergoes a cyclic variation as the tube $\mathbf{E} \times \mathbf{B}$ drifts around the plasma axis. Electron-electron collisions act to dissipate this compressional motion. This dissipation causes the plasma to expand radially and increase in temperature over a time period of $10^5$ or more column rotations. Simultaneously, the displacement of the column decreases, damping the diocotron mode. Ultimately, the plasma column axisymmetrizes with the cylindrical trap.

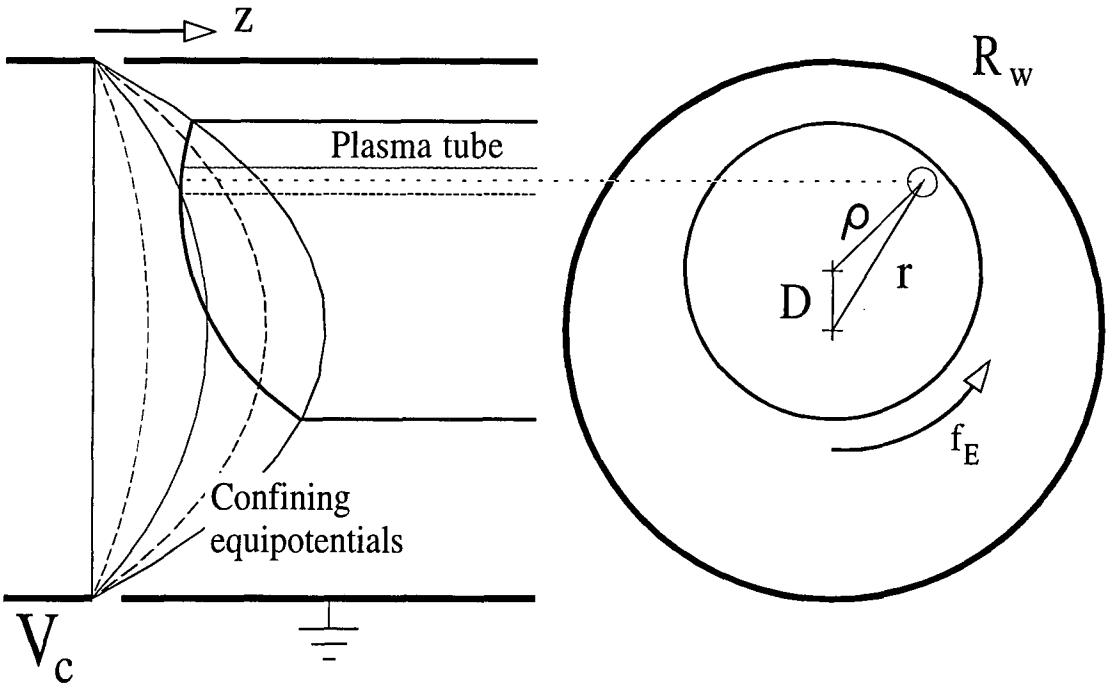


**Figure 4.1:** Length of a tube of plasma in an off-axis plasma column is pumped by the $\mathbf{E} \times \mathbf{B}$ rotation. The curvature of the confining equipotentials makes the tube longer near the trap wall than near the trap axis.

In Section 4.2, I describe measurements of the evolution of the plasma's density profile, temperature, and displacement from the trap axis. These measurements show that the total number of electrons and the total angular momentum of the plasma are both conserved by the expansion/damping process. The total energy of the plasma is also conserved by the dissipation of electrostatic energy into heat. This thermal energy is then cyclotron radiated away.

In section 4.3, I describe measurements of the transport and damping rate as a function of several plasma parameters. Because the transport conserves the total angular momentum of the plasma, the damping rate of the $m = 1$ diocotron mode provides a nondestructive measurement of the radial expansion of the plasma. These measurements indicate that the transport rate is independent of the magnetic field

strength and that the mechanism behind the transport depends on the collisional equilibration of $T_\perp$ and $T_\parallel$.

In section 4.4, I present a simple theory, due to Crooks and O'Neil [7], that explains the observed transport and damping. They analyze the cyclic variation in the length of a tube of plasma as it drifts around the plasma axis. This variation causes a variation in $T_\parallel$. Collisions then act to equilibrate $T_\perp$ and $T_\parallel$, resulting in an irreversible heating of the plasma. Equating the increase in thermal energy with Joule heating gives the radial electron flux, while conservation of $P_\theta$ gives the damping rate of the $m = 1$ diocotron mode.

In section 4.5, I compare the predictions of the theory to measured particle fluxes and damping rates. The theoretical fluxes agree to within a factor of 3 with my measurements. The theoretical damping rates are in good agreement with my measurements, both in absolute magnitude and in scalings with plasma parameters.

In section 4.6 and 4.7, I discuss 2 parameter regimes where the Crooks and O'Neil theory breaks down. At very low temperatures, where $f_E/\overline{f_B} \geq 1$, the bounce motion of the electrons is no longer an adiabatic invariant, and the theory predicts additional transport due to bounce-rotation resonances. I do not observe this increase in transport, but find that the adiabatic invariant theory still works quite well. In the high temperature regime, the Debye length becomes large, and the "length" of a tube of plasma is ill-defined. In this regime, I observe an increase in the transport rate with temperature, whereas the theory predicts a decrease. At these temperatures, the confining electric fields cause a thermal spread in the $\mathbf{E} \times \mathbf{B}$ drift velocities. The increase in the damping rate can be qualitatively explained by this thermal spread.

In section 4.8, I discuss the nonlinear damping of the $m = 1$ diocotron mode. I show that while the damping of large amplitude ($D > R_p$) modes is still described by the linear theory, the damping rate changes with time as the plasma density and

temperature profiles are changed by the damping process. In the strongly magnetized regime, the steep drop of the anistropic temperature equilibration rate causes a nonlinear instability in the plasma temperature, and consequently gives rise to unstable variations in the transport rate. This instability can cause bifurcations in the time evolution of the plasma displacement. Furthermore, if a resistive wall destabilizes the diocotron mode, nonlinear oscillations in the temperature result in "sawtooth" oscillations of the displacement of the plasma column. A simple computer model incorporating the unusual temperature dependence of the rotational pumping rate quantitatively reproduces this complicated, nonlinear "dance" of the diocotron mode [26].

In section 4.9, I discuss alternative mechanisms for the damping of the $m = 1$ diocotron mode and show that they have negligible effect compared to the rotational pumping mechanism. In section 4.10, I discuss how rotational pumping may be important in several other plasma experiments, neutral as well as nonneutral.

## 4.2 Conserved Quantities

In this section, I present measurements of a typical evolution of a plasma undergoing transport and mode damping caused by rotational pumping. The plasma in this evolution was initially about 3.5 cm long and 0.7 cm in radius, with a central density of $7.5 \times 10^9$ cm$^{-3}$. The initial temperature was 0.05 eV and the magnetic field was 40 kG. I created an $m = 1$ diocotron mode and observed the evolution of the plasma over 10 seconds, which is more than $10^6$ column rotations.

The evolution of the plasma displacement, radius, and temperature is shown in Figure 4.2. The initial displacement of the plasma column is $D/R_w = 0.175$. As $D$ decreases, the plasma expands. In Figure 4.2, the "plasma radius" $R_p$ is defined

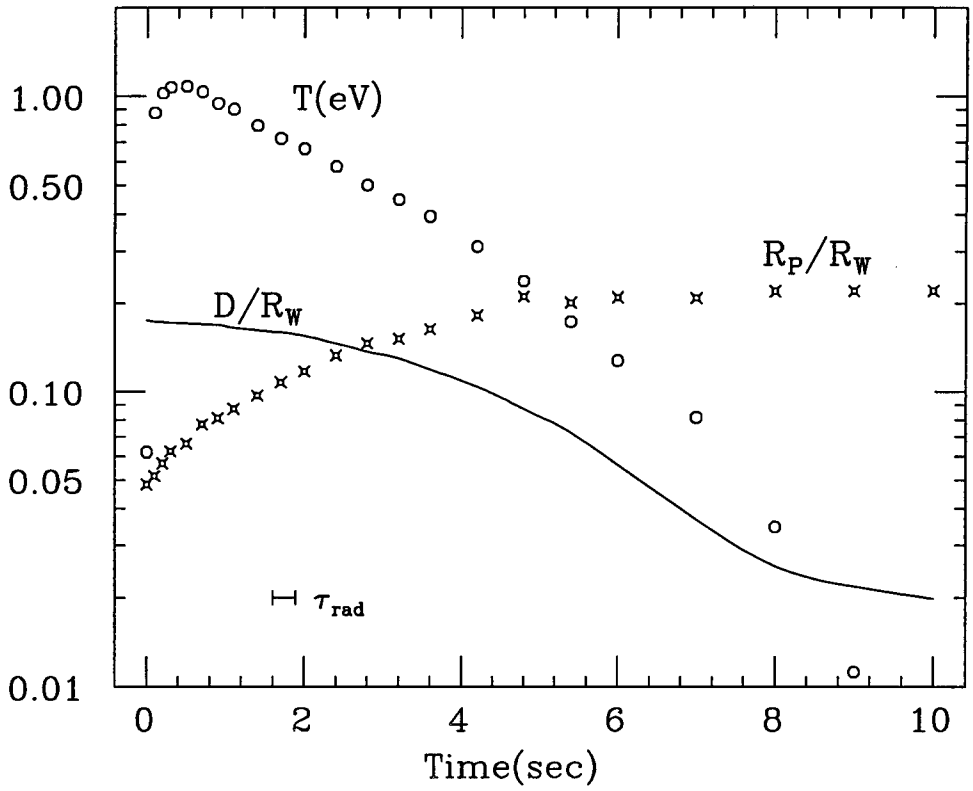


**Figure 4.2:** The radius of an off-axis plasma column increases with time; the displacement of the column simultaneously decreases. The initially cold plasma heats up and then slowly cools. The cooling time is much longer than the cyclotron radiation time.

by

$$R_p = \frac{3}{2}\frac{\int_0^{R_w} \rho d\rho \; n_z \rho}{\int_0^{R_w} \rho d\rho \; n_z}, \tag{4.1}$$

where $n_z$ is the $z$-integrated plasma density and $\rho$ is the radial distance from the plasma axis as shown in Figure 4.1, i.e. $\mathbf{r} = \mathbf{D} + \boldsymbol{\rho}$. For a uniform density column, $R_p$ is the radius of the column. The temperature $T$ shows a rapid initial increase, but after 0.5 seconds starts to slowly decrease due to cyclotron cooling. The measured radiation time at $B = 40$ kG is $\tau_{rad} = 0.29$ sec [1], which is much shorter than the time on which $T$ decreases. This indicates that the cyclotron cooling is nearly balanced by the generation of thermal energy in the plasma.

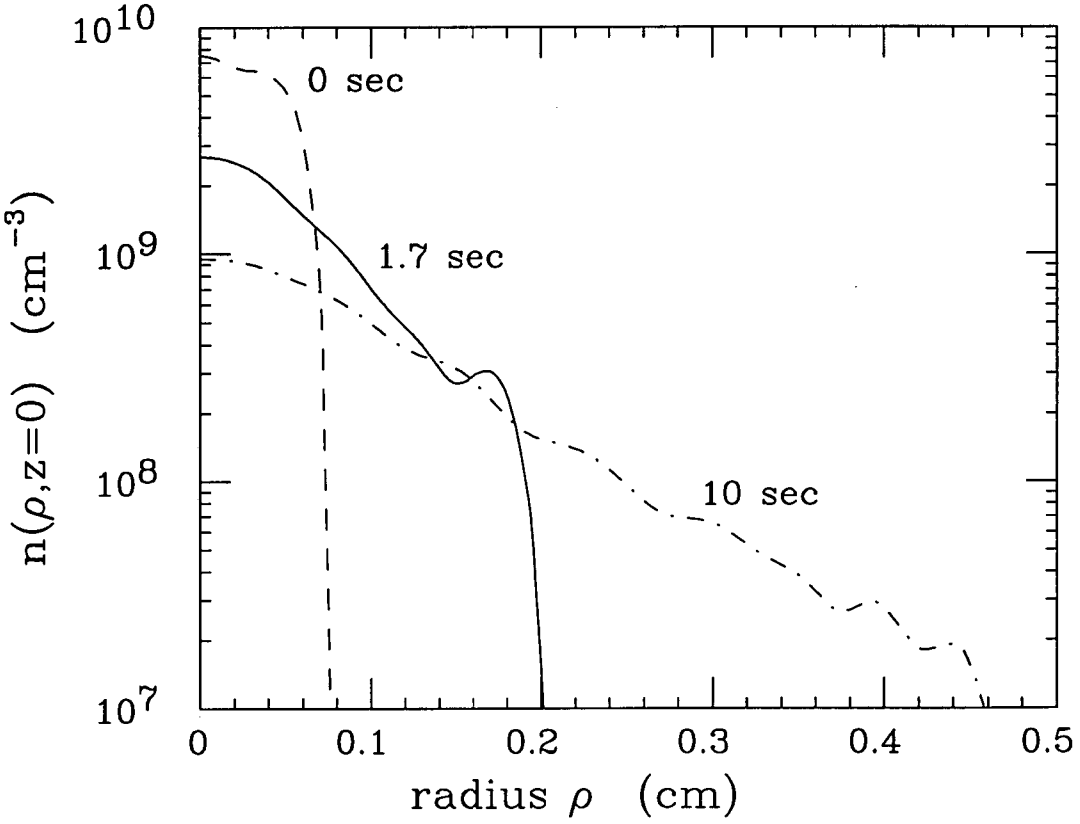


**Figure 4.3:** Evolution of the plasma density profile during rotational pumping. The central density decreases by a factor of 8 with a corresponding increase in radius.

As time goes on, $D$ decreases at a continually faster rate as $R_p$ continues to grow. The plasma cools as the rate of generation of thermal energy decreases. Finally, $D$ and $R_p$ level off at constant values when $T$ drops below 0.01 eV.

Figure 4.3 shows the radial density profile at the axial center of the plasma, $n(\rho, z = 0)$, at 3 different times during the evolution: 0, 1.7, and 10 seconds. A log scale is used on the vertical axis to show the radial extent of the final profile. These profiles were measured using the many-shot, deconvolution technique described in Section 2.4.2. The initially narrow, high density plasma undergoes considerable radial expansion, causing a decrease in the central density by a factor of 8 over the 10 second evolution. The shape of the profile also changes significantly. The

initial density profile has a very steep gradient, while the final profile has a much milder slope. Despite causing large changes in density profile, the transport process conserves the total number of electrons in the plasma, $N$. No electrons are lost to the trap walls or over the potential barriers at the end.

The damping of the $m = 1$ diocotron mode as the plasma expands conserves the total angular momentum of the plasma, $P_\theta$. The total angular momentum is proportional to $\langle r^2 \rangle$, the mean square radius of the plasma about the axis of the trap, as shown by Equation 3.1. The parallel axis theorem can be used to write

$$\langle r^2 \rangle = \langle \rho^2 \rangle + D^2. \tag{4.2}$$

Figure 4.4 shows the measured values of $\langle (\rho/R_w)^2 \rangle$ and $(D/R_w)^2$ over the 10 second evolution. Initially the radius of the column is small compared to its displacement, and 97% of the angular momentum is in $(D/R_w)^2$. As the plasma expands radially, the diocotron mode simultaneously damps, so that by 10 seconds only 1% of the angular momentum is in $(D/R_w)^2$. The sum of $\langle (\rho/R_w)^2 \rangle$ and $(D/R_w)^2$ is constant, however, indicating that $P_\theta$ is conserved. The forces causing the transport must be azimuthally symmetric about the trap axis.

The expansion/damping process converts the plasma's electrostatic energy, $H_\phi$, into thermal energy, $H_T$. To measure the total energy balance in the plasma, I calculate the energy lost to cyclotron radiation, $H_{rad}$; as well as the work done by the plasma on the power supplies, $W_{ps}$, as they maintain the end cylinders at constant voltage. The values of $H_\phi$, $H_T$, $H_{rad}$, and $W_{ps}$ per electron are calculated as

$$H_\phi = -\frac{1}{2N} \int d^3x \; n(x,y,x) \, e\phi(x,y,z), \tag{4.3}$$

$$H_T = \frac{3}{2} kT, \tag{4.4}$$

$$H_{rad} = \frac{3}{2} \int_0^t \frac{kT}{\tau_{rad}} dt', \tag{4.5}$$

$$W_{ps} = -\frac{1}{2} \frac{\Delta Q}{N} V_c, \tag{4.6}$$

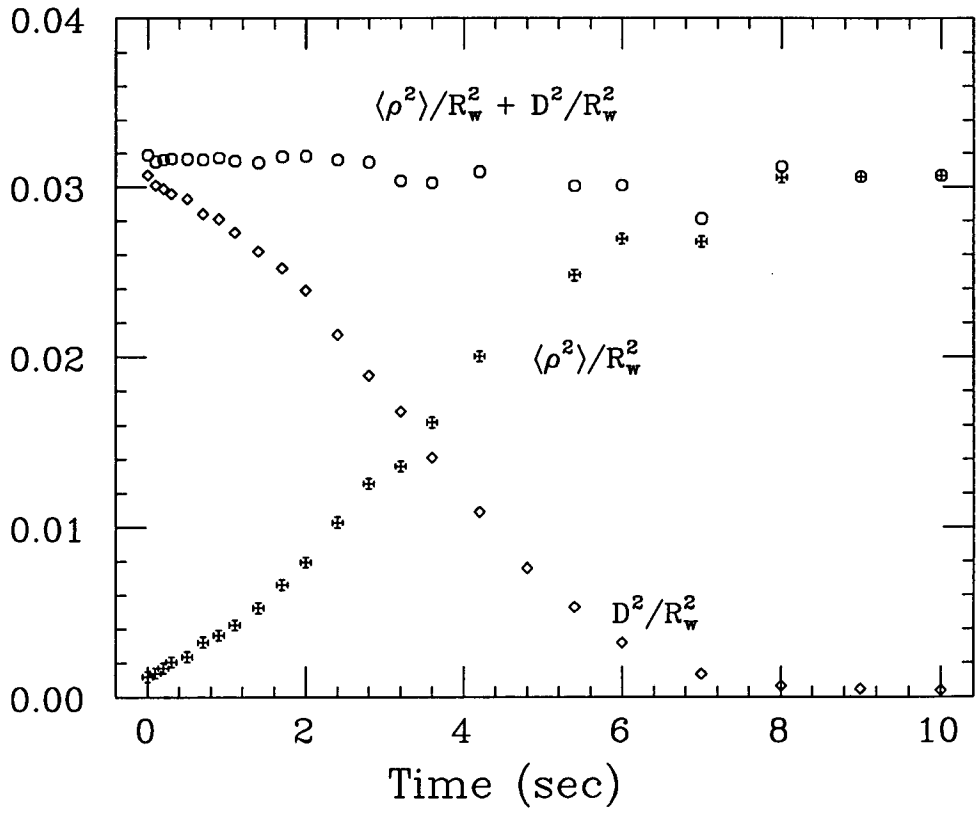


**Figure 4.4:** Evolution of $D^2$ and $\langle\rho^2\rangle$ during rotational pumping, showing that the total angular momentum is conserved.

where $\Delta Q(t)$ is the change in the amount of charge on the end cylinders since $t = 0$, and I assume that $T_\perp \approx T_\parallel \equiv T$ since the anisotropic temperature equilibration rate is much faster than the cyclotron cooling rate, i.e. $\nu_{\perp\parallel} \gg \tau_{rad}^{-1}$.

Figure 4.5 shows the evolution of $H_\phi$, $H_T$, $W_{ps}$, and $H_{rad}$. Over the 10 second evolution, $H_\phi$ decreases by 40% from its intial value as the plasma column expands. About 6% of this energy is recovered in $W_{ps}$ because the confining potentials compress the plasma axially as its space charge potential decreases. The electrostatic energy released is converted into heat, increasing $H_T$ over the first 0.5 seconds, until the Joule heating is overwhelmed by cyclotron cooling, gradually reducing $H_T$. The dissipation of $H_\phi$ into $H_T$ indicates that $\mathbf{E} \times \mathbf{B}$ drift dynamics alone (which conserve

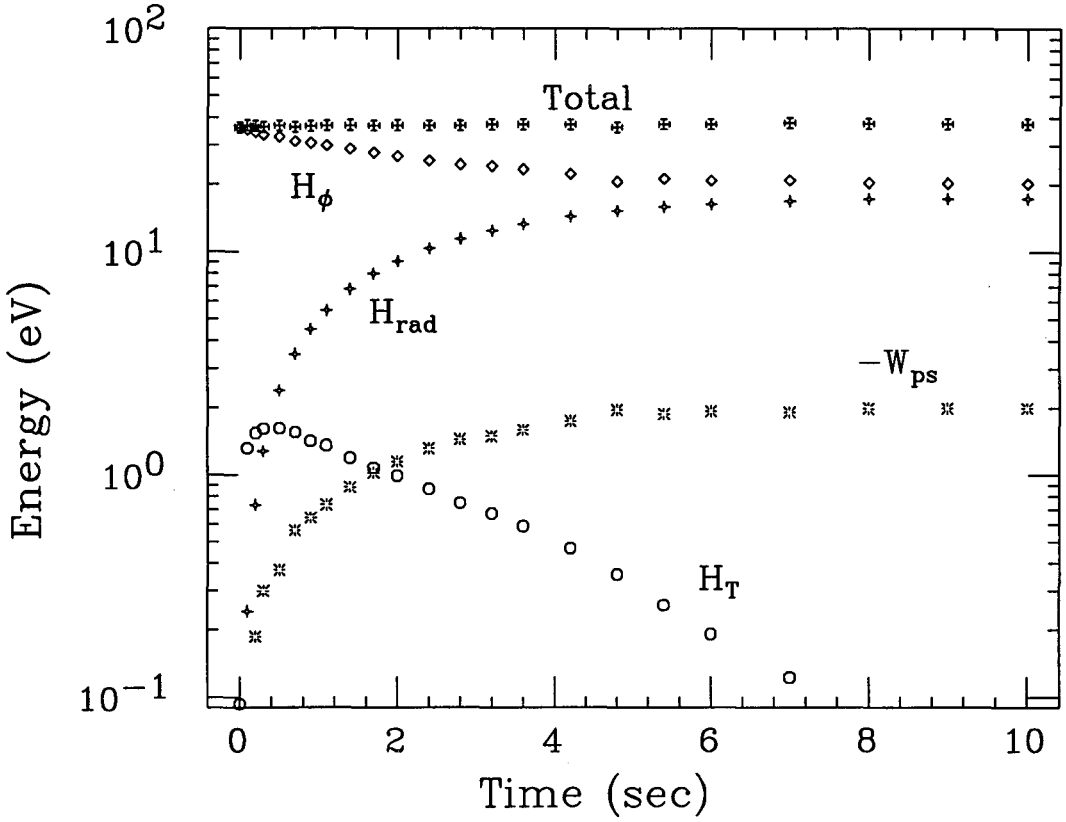


**Figure 4.5:** Evolution of the electrostatic, radiated, thermal and power supply components of the total energy during rotational pumping. The sum of the 4 components is conserved over the 10 second evolution.

$H_\phi$) cannot be responsible for the observed transport. The total energy of the plasma, $H_\phi + W_{ps} + H_T + H_{rad}$, remains constant over the evolution. This indicates that the plasma is not coupled to any unknown energy sources or sinks, and that the forces causing the transport are not time dependent.

## 4.3 Damping Rates

I characterize the transport by the damping rate of the $m = 1$ diocotron mode, which can be measured nondestructively. Figure 4.6 shows $D$ as a function of time for 6 different initital displacements of essentially the same plasma. The displacement decreases exponentially with time, i.e. $D = D_0 \exp(-\gamma t)$, for $D_0 < R_p$.

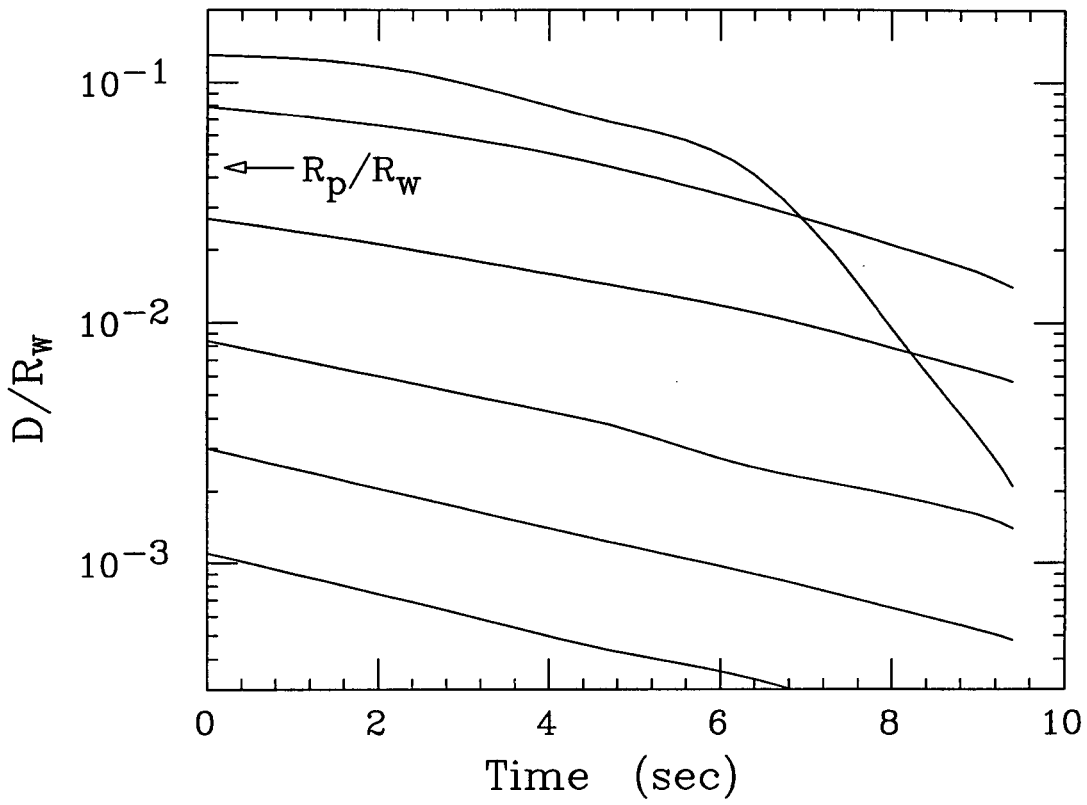


**Figure 4.6:** Damping of the $m = 1$ diocotron mode from 6 different initial displacements. The damping is exponential in time for $D < R_p$.

Thus, the damping is a linear process for $D_0 < R_p$.

I have measured the damping rate, $\gamma$, as a function of several plasma parameters for $D_0 \ll R_p$. The parameteric dependence of $\gamma$ exhibits several unique signatures. One is that, for moderate temperatures, it is nearly independent of magnetic field strength, as shown in Figure 4.7. As $B$ is increased from 10 to 60 kG, $\gamma$ decreases only about 30%. This is counter-intuitive, as transport rates usually scale with $\mathbf{E} \times \mathbf{B}$ drifts or the mean electron cyclotron radius, $r_c$, both of which decrease with $B$. Indeed, previous experiments on nonneutral plasmas have found transport rates that scaled as $B^{-1}$ [13] or $B^{-2}$ [11, 12].

The most striking signature of the $m = 1$ diocotron mode mode damping is

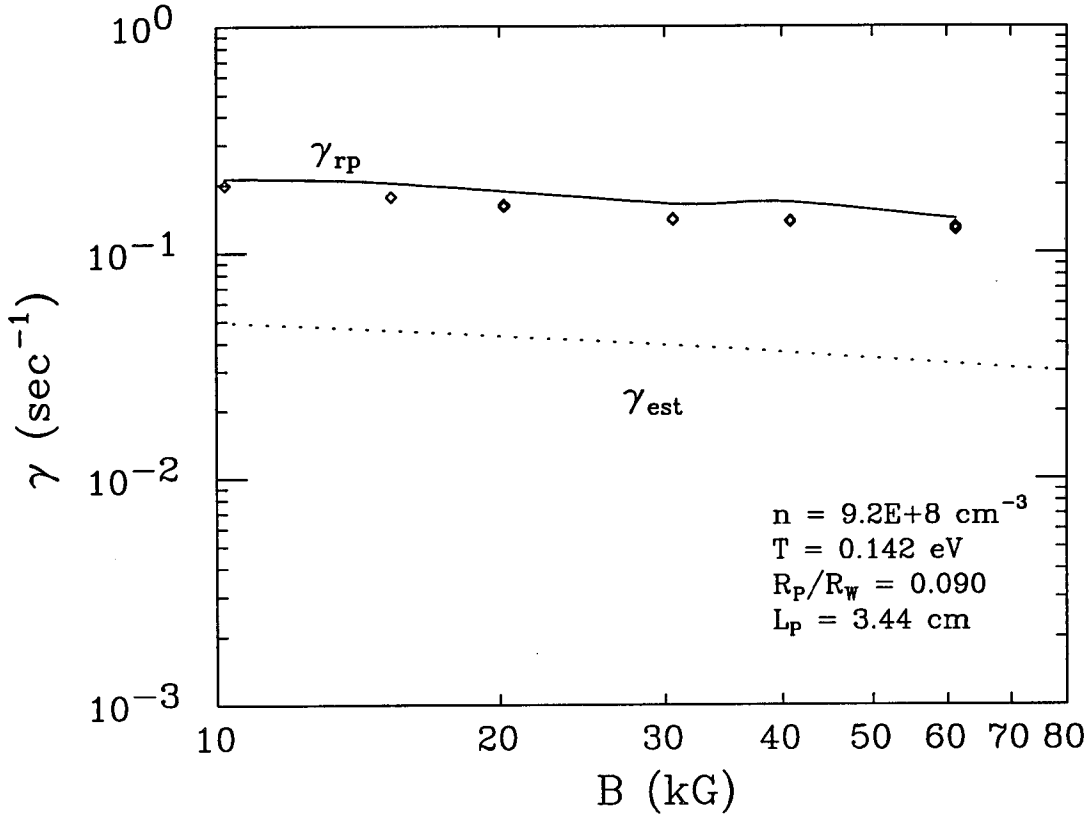


**Figure 4.7:** The damping rate of the $m = 1$ diocotron mode is nearly independent of $B$ for moderate temperatures. The dotted line is the estimated prediction from the Crooks and O'Neil theory; the solid line is the exact, numerically calculated prediction.

the scaling of $\gamma$ with temperature, as shown in Figure 4.8. The damping rate drops by 2 orders of magnitude as the temperature is decreased from 0.01 eV to 0.003 eV. In this regime, $r_c$ is smaller than the distance of closest approach, $b = e^2/T$. As discussed in Section 2.7, the anisotropic temperature equilibration rate, $\nu_{\perp\parallel}$, becomes exponentially small for $r_c \ll b$ because colliding electrons can't get close enough together to exchange perpendicular and parallel kinetic energy [2, 22]. This is a strong indication that $\gamma \propto \nu_{\perp\parallel}$. The decrease in $\gamma$ at temperatures above 0.1 eV is also consistent with this dependence, as $\nu_{\perp\parallel} \propto T^{-3/2}$ at high temperatures.

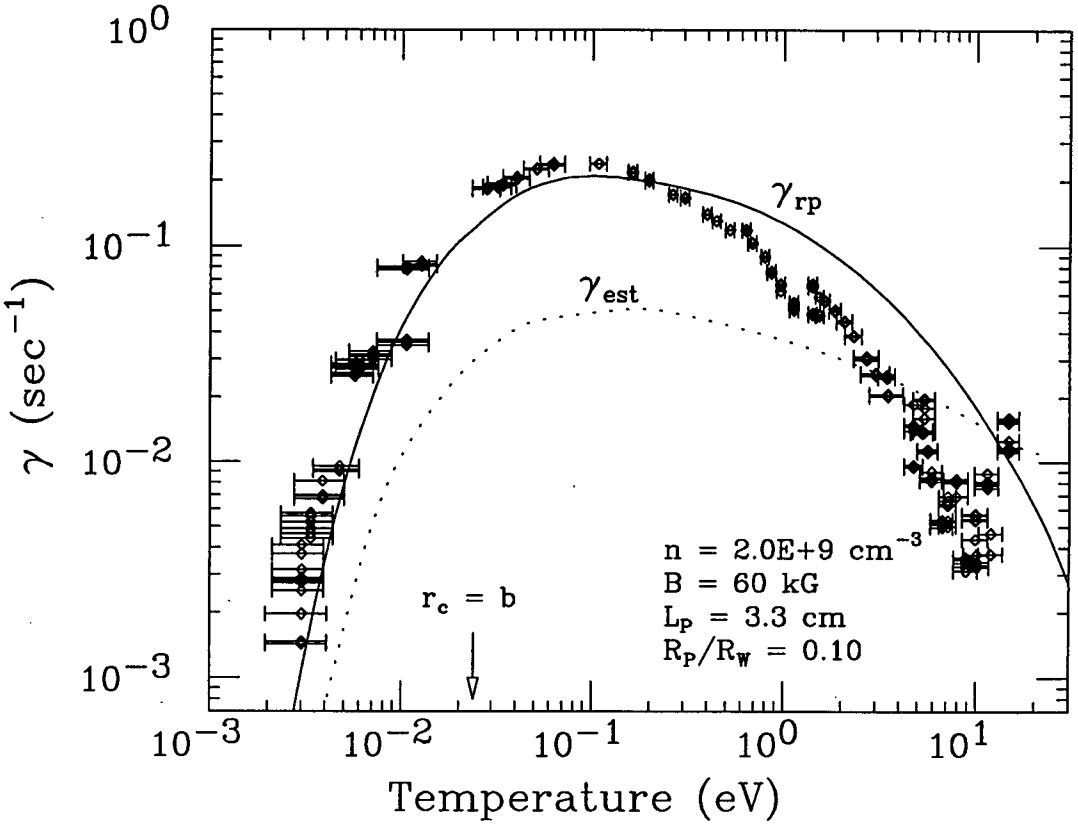


**Figure 4.8:** The damping rate of the $m = 1$ diocotron mode drops precipitously when the electrons becomes strongly magnetized, i.e. when $r_c < b$. The dotted line is the estimated prediction from the Crooks and O'Neil theory; the solid line is the exact, numerically calculated prediction.

## 4.4 Rotational Pumping Theory

The recent theory of rotational pumping by Crooks and O'Neil [7] proposes that the plasma expands because the potentials produced by the confining voltages on the end cylinders are not azimuthally symmetric about the *plasma* axis, as shown in Figure 4.1. Thus, a tube of plasma is alternately compressed and rarefied as it $\mathbf{E} \times \mathbf{B}$ drifts around the plasma axis, producing a modulation in its parallel temperature.

Crooks and O'Neil assume that the Debye length is small, i.e. $\lambda_D \ll L_p$. Thus, the potential along a field line is uniform inside the plasma and abruptly

increases at the ends, so that the bounce length of an electron is independent of its energy. The electrons move freely along the field lines, and specularly reflect off the "hard" ends of the plasma. The length of a tube of plasma at radius $\rho$ is then described by

$$L(\rho,t) = L_0(\rho) + \delta L(\rho)\,\cos\omega_R t, \tag{4.7}$$

where $\delta L \ll L_0$ and $\omega_R(\rho)/2\pi = f_E(\rho) - f_d$ is the rotation frequency of the plasma in the diocotron mode frame, where the center of charge of the plasma is stationary. Ignoring radiation, the evolution of $T_\perp$ and $T_\parallel$ in the tube of plasma are described by the equations

$$\frac{d}{dt}T_\perp(\rho,t) = \nu_{\perp\parallel}(\rho)\,(T_\parallel - T_\perp), \tag{4.8}$$

$$\frac{d}{dt}T_\parallel(\rho,t) = -2\nu_{\perp\parallel}(\rho)\,(T_\parallel - T_\perp) - \frac{2}{L}\frac{dL}{dt}T_\parallel. \tag{4.9}$$

The $-(2/L)(dL/dt)T_\parallel$ term is the rate of increase of internal energy of an ideal gas as it is compressed, i.e. $dW/dt = pdV/dt$. I solve these equations perturbatively, as was done by Beck [1]. To zeroth order in $\delta L/L_0$, Eqs. 4.7- 4.8 give ${T_\perp}^{(0)} = {T_\parallel}^{(0)} = T(\rho)$, where the superscript denotes the order. To 1st order, assuming $\nu_{\perp\parallel} \ll \omega_R$,

$$T_\perp^{(1)} = -2\,T\,\frac{\delta L}{L_0}\,\frac{\nu_{\perp\parallel}}{\omega_R}\,\sin\omega_R t, \tag{4.10}$$

$$T_\parallel^{(1)} = -2\,T\,\frac{\delta L}{L_0}\left(\cos\omega_R t - 2\frac{\nu_{\perp\parallel}}{\omega_R}\sin\omega_R t\right). \tag{4.11}$$

The modulation of $T_\parallel^{(1)}$ is nearly in phase with the modulation in $L$, but a fraction $2\nu_{\perp\parallel}/\omega_R$ of $T_\parallel^{(1)}$ is scattered into $T_\perp^{(1)}$. (Note that $\nu_{\perp\parallel}/\omega_R$ is always less than 1 in a nonneutral plasma.) The second term in Equation 4.11, multiplied by $dL/dt$ in Equation 4.9, gives an irreversible heating to second order. The rate of change of the $z$-integrated thermal energy density in the tube of plasma, averaged over a plasma rotation, is

$$\frac{1}{2}n_z k\left\langle\frac{d(T_\parallel + 2T_\perp)}{dt}\right\rangle_{rot} = 2n_z kT\nu_{\perp\parallel}\left(\frac{\delta L}{L_0}\right)^2, \tag{4.12}$$

where $n_z(\rho)$ is the $z$-integrated density and the brackets denote averaging over a rotation. Crooks and O'Neil assume that $2\pi\overline{f_B} \gg \omega_R$, so that the electron bounce action is an adiabatic invariant, and $T_{||}$ and $T_\perp$ are uniform along the magnetic field. Using conservation of energy to equate the rotation averaged rate of change in thermal energy to the rotation averaged Joule heating caused by radial transport,

$$\langle -e\Gamma_\rho(\rho)E_\rho(\rho)\rangle_{rot} = \frac{1}{2}n_z k\left\langle \frac{d(T_{||}+2T_\perp)}{dt}\right\rangle_{rot}, \tag{4.13}$$

one obtains an expression for the theoretical, $z$-integrated, rotation averaged, radial electron flux in the frame of an observer located at the center of charge of the plasma column,

$$\Gamma_\rho^{th}(\rho) = \frac{2n_z kT\nu_{\perp||}}{-eE_\rho}\left(\frac{\delta L}{L_0}\right)^2, \tag{4.14}$$

where $E_\rho(\rho)$ is the radial electric field in the $m = 1$ diocotron mode frame. (A derivation of Equation 4.14 from a dynamical model is given in Appendix F.)

## 4.5 Comparison between Theory and Experiment

### 4.5.1 Fluxes

I am able to directly compare the Crooks and O'Neil rotational pumping theory to my measurements, with no adjustable parameters, because all quantities on the right-hand side of Equation 4.14 can be determined experimentally. The temperature and $n_z$ are directly measured, and $\nu_{\perp||}$ can be calculated from the measured values of $T$, $n$, and $B$. The 3-D density and potential profiles which are obtained from the measured $n_z$ and $T_{||}$, by numerically solving the Poisson and Boltzmann equations are used to calculate the electric field. The radial electric field, density averaged along a field line, is defined by

$$\langle E_\rho(\rho)\rangle_z = \frac{1}{n_z}\int dz\; n(\rho,z)E_\rho(\rho,z). \tag{4.15}$$

The 2-D plasma length profile is defined by

$$L(x,y) = \frac{n_z(x,y)}{n(x,y,z=0)}, \tag{4.16}$$

where $z = 0$ is at the axial center of the plasma and $(x - D)^2 + y^2 = \rho^2$. The difference in $L(x,y)$ between two sides of the plasma determines $\delta L(\rho)$

$$\delta L(\rho) = \frac{1}{2}[L(\rho + D, 0) - L(\rho - D, 0)], \tag{4.17}$$

while $L_0(\rho)$ is defined as the average between the two sides

$$L_0(\rho) = \frac{1}{2}[L(\rho + D, 0) + L(\rho - D, 0)]. \tag{4.18}$$

Given 2 $z$-integrated density profiles, $n_z(\rho,t)$ and $n_z(\rho,t+\delta t)$, I define the rate of change of the $z$-integrated density by

$$\frac{\partial n_z(\rho,t)}{\partial t} = \frac{n_z(\rho,t+\delta t) - n_z(\rho,t)}{\delta t}. \tag{4.19}$$

By integrating the continuity equation, $\partial n/\partial t + \nabla \cdot \mathbf{\Gamma} = 0$, an experimental value of the radial flux can be obtained:

$$\Gamma_\rho^{exp}(\rho) = -\frac{1}{\rho}\int_0^\rho \rho' d\rho' \, \frac{\partial n_z(\rho')}{\partial t}. \tag{4.20}$$

Using the density profiles I measured for the 10 second evolution shown in Figures 4.2-4.5, I have calculated $\Gamma_\rho^{exp}(\rho,t)$ for each measurement time in that evolution. Figure 4.9 shows the ratio of $\Gamma_\rho^{th}$ to $\Gamma_\rho^{exp}$ plotted against $\rho/R_p$, for $t < 6$ seconds. (The change in $n(\rho)$ after $t = 6$ seconds was smaller than the measurement noise.) Around $\rho = R_p$, most of the $\Gamma_\rho^{exp}$ agree with the $\Gamma_\rho^{th}$ within a factor of 1.5, although some only agree within a factor of 4. The large discrepancies between theory and experiment around $\rho = 0$ and $\rho > 1.5R_p$ can be explained by ripples in the measured density profiles. These are the result of measurement noise which is amplified by the deconvolution process described in Section 2.4.2.

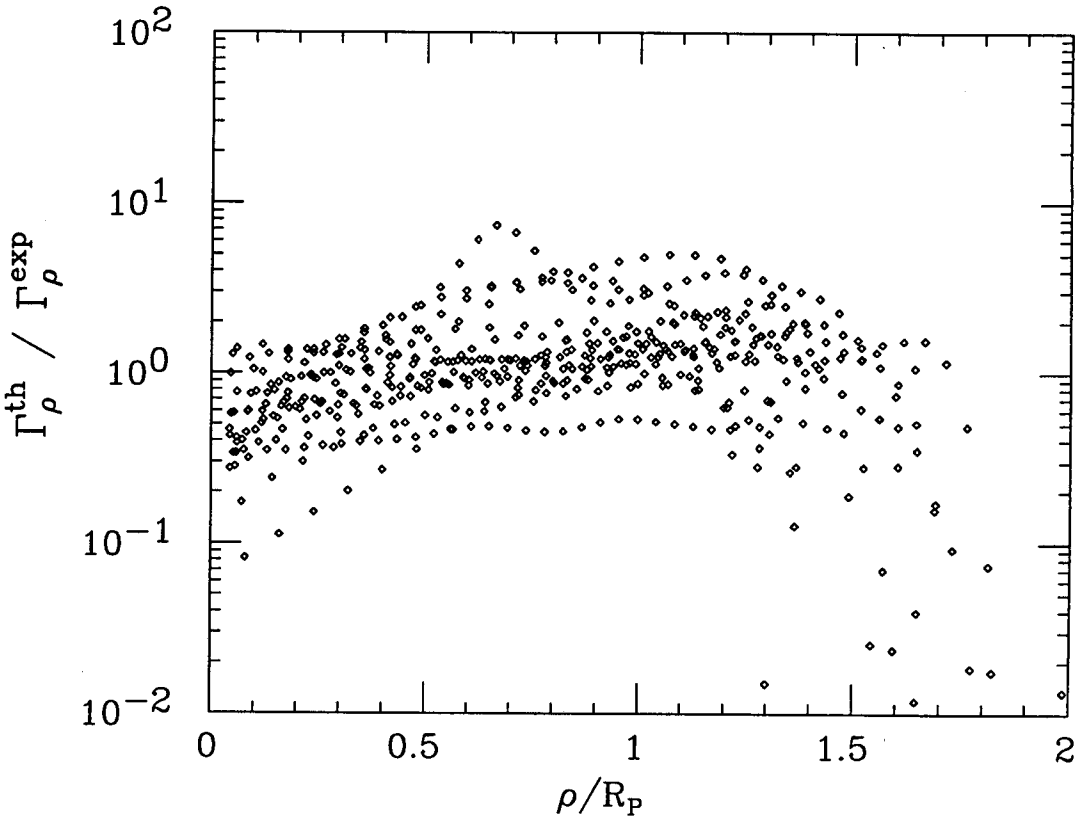


**Figure 4.9:** Ratio of theoretical to experimental radial flux from rotational pumping as a function of distance from the plasma axis for the evolution shown in Figure 4.2. Theory and experiment are in general agreement. The large scatter in the data is due to difficulties in measuring $n_z(\rho)$. For each plasma, $R_p$ is defined by Equation 4.1.

Examination of Equation 4.14, $n(x,y,z)$, and $\phi(x,y,z)$ reveals why rotational pumping caused the decrease in the slope of the radial density profile shown in Figure 4.3. Because the plasma was fairly short, i.e. $L_p \approx 2.5R_w$, $L_0$ decreased by factor of 2 from the center to the radial edge of the plasma. This caused an increase in $\Gamma_\rho^{th}$ at the plasma edge, which acted to "stretch out" the density profile. A longer plasma of the same density and temperature would have nearly the same $\nu_{\perp\parallel}$, $E_\rho$, and $\delta L$, but $L_0$ would be nearly uniform in $\rho$.

### 4.5.2 Damping Rates

The rotational pumping damping rate of the $m = 1$ diocotron mode, $\gamma_{rp}$, can be calculated from the theoretical radial flux by using the continuity equation and conservation of angular momentum:

$$\gamma_{rp} \equiv -\frac{1}{D}\frac{dD}{dt} = \frac{1}{D^2}\frac{d\langle\rho^2\rangle}{dt} \equiv \frac{1}{ND^2}\int 2\pi\rho d\rho\ \rho^2\ \frac{1}{\rho}\frac{\partial(\rho\Gamma_\rho^{th})}{\partial\rho}. \tag{4.21}$$

This integral can be solved easily if the plasma is a column of uniform density and temperature with radius $R_p$ and length $L_p$, and $\delta L$ is approximated by $\delta L = \kappa(D/R_w)\rho$, where $\kappa \approx 2.4$ [50] (See Appendix B). Using this approximation, a theoretical estimate of the $m = 1$ diocotron mode damping rate is given by

$$\gamma_{est} = 2\kappa^2\nu_{\perp\parallel}\left(\frac{\lambda_D}{L_0}\right)^2\frac{(R_p/R_w)^2}{1-(R_p/R_w)^2}, \tag{4.22}$$

where the factor $1-(R_p/R_w)^2$ appears in the denominator because the $m = 1$ diocotron mode is a negative energy mode. Less dissipation of electrostatic energy is required than if the mode energy was nonnegative. (The estimated damping rate in Equation 4.22 can also be derived from a dynamical model of rotational pumping; see Appendix F.)

The estimated damping rate is generally a factor of 5 smaller than the measured $\gamma$, but gives approximately the correct scalings with plasma parameters. Much closer agreement is obtained, however, by using the $n(x,y,z)$ and $\phi(x,y,z)$ which are numerically calculated from the measured $n_z$ and $T$ to obtain $\Gamma_\rho^{th}$ and then numerically integrating Equation 4.21. I denote the theoretical rotational pumping damping rates obtained in this way as $\gamma_{rp}$. The $\gamma_{rp}$ are in close agreement with the data; they are generally a factor of 5 larger than the $\gamma_{est}$. There are 2 reasons for this difference between $\gamma_{rp}$ and $\gamma_{est}$. One is that the $\gamma_{est}$ calculation underestimates $\delta L$. For the narrow columns used in these experiments, $\delta L = \kappa(D/R_w)\rho$ is better approximated by $\kappa \approx 5-7$ instead of 2.4, as shown in Appendix B. The other reason is that some

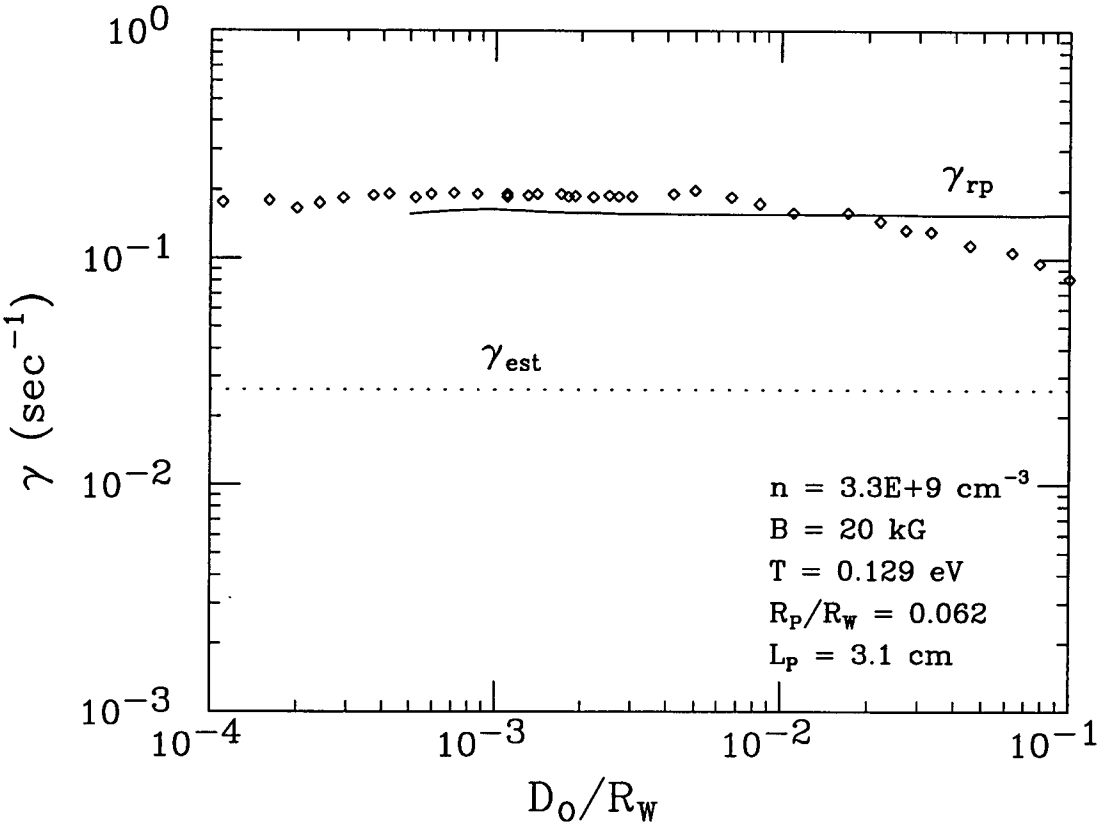


**Figure 4.10:** The damping rate of the $m = 1$ diocotron mode is independent of displacment. The dotted line is the estimated prediction from the Crooks and O'Neil theory; the solid line is the exact, numerically calculated prediction.

of the experimental density profiles are far from uniform, and have long, low density "tails." Hence, the effective radii of these plasmas is larger than the values used in calculating $\gamma_{est}$. The scalings of the measured and theoretical damping rates with plasma parameters are discussed below.

### Displacement

As noted in Section 4.3, the damping of the $m = 1$ diocotron mode is observed to be a linear process for $D_0 < R_p$. Thus, $\gamma$ is independent of $D$ in this regime, as shown in Figure 4.10. According to the rotational pumping theory, the damping is independent of $D$ because $\Gamma_\rho^{th} \propto \delta L^2 \propto D^2$, and $\gamma_{rp} \propto \Gamma_\rho^{th}/D^2$. The theory agrees

with the data to within 20% for $5 \times 10^{-4} < D_0/R_w < 10^{-2}$. The decrease in $\gamma$ at large $D_0$ occurs because Joule heating overwhelms cyclotron cooling, increasing the plasma temperature. [For $D_0 < 5 \times 10^{-4}$, $\delta L$ is smaller than the grid spacing used to numerically calculate $n(x,y,z)$ and $\phi(x,y,z)$.]

### Magnetic Field

Because $\omega_R \gg \nu_{\perp\parallel}$ in nonneutral plasmas and the plasma energy is dominantly electrostatic, the theoretical damping rate depends on $B$ only through $\nu_{\perp\parallel}$, which is consistent with the data in Figure 4.7. The plasma temperature for that data was 0.14 eV, so that $r_c$ was greater than $b$ for all the $B$. The equilibration rate then depends on $B$ only through the Coulomb logarithimn, i.e. $\nu_{\perp\parallel} \propto \ln(r_c/b)$.

### Temperature

The measured dependence of $\gamma$ on $T$ shown in Figure 4.8 is largely explained by the theoretical dependence $\gamma_{rp} \propto \nu_{\perp\parallel} T$. The difference in slope between $\gamma_{rp}$ and $\gamma_{est}$ in Figure 4.8 at temperatures above 1 eV is due to a decrease in $\delta L$ with temperature. As shown in Appendix B, high temperatures decrease the space charge enhancement of $\delta L$. Also, higher energy electrons see a smaller $\delta L$ because they penetrate farther towards the end cylinders where the vacuum equipotential surfaces have less curvature than those well inside the grounded confinement region, as shown in Figure 4.12.

The discrepancy between the data and the solid curve in Figure 4.8 at temperatures above 0.2 eV may be because at high enough temperatures $\lambda_D \sim \delta L$, so the ends of the plasma can no longer be considered "hard." Thus, the length of a tube of plasma is no longer well-described by Equation 4.7. The discrepancy may also be a sytematic error. If the plasma temperature increases with $\rho$, the damping rate

will be smaller than the measured value of $T_{\|}$ at the plasma center would indicate (assuming $r_c > b$). This could happen if actively heating the plasma preferentially heats its outer edge and the radial thermal conductivity of the plasma is low. Energy transport in CV plasmas is discussed in Section 2.7.

### End Shape

The central idea of the Crooks and O'Neil theory is that $\gamma_{rp}$ depends on an asymmetry in the shape of the plasma ends. A direct test of the theory is then provided by changing the end shape. Figure 4.11 shows the dependence of the measured damping rate on the confinment voltage $V_c$. As $|V_c|$ is lowered towards the plasma potential $|\phi_p|$, the ends of the plasma get closer to the "flat" equipotential surfaces at the boundaries between the end cylinders and the grounded cylinders, as shown in Figure 4.12. This decreases $\delta L$ and thus decreases $\gamma_{rp}$. The dotted curve in Figure 4.11 is flat because the calculation of $\gamma_{est}$ assumes the plasma is well inside the grounded cylinders.

### Density

Figure 4.13 shows $\gamma$ plotted against the plasma density averaged over the central collector P1, i.e. plotted against $-q_1/e$ as defined in Equation 2.3. The damping rate is nearly independent of $n$ because $\nu_{\perp\|} \propto n$ and $\lambda_D^2 \propto n^{-1}$, so the $n$ dependence cancels out in Equation 4.22. The data and theory may disagree at low densities for the same reason that they disagree at high temperatures in Figure 4.8; Equation 4.7 is not valid when $\lambda_D \sim \delta L$.

### Plasma Radius

The dependence of $\gamma$ on the plasma radius is shown in Figure 4.14. In this

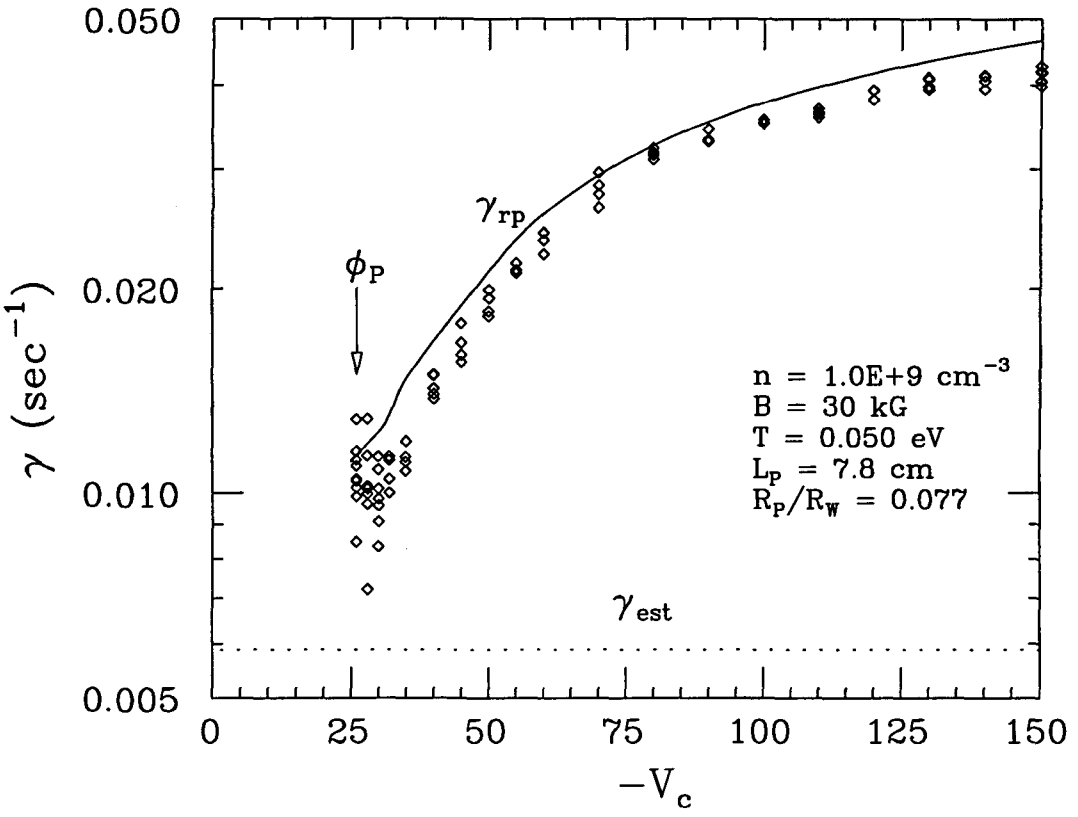


**Figure 4.11:** The damping rate of the $m = 1$ diocotron mode decreases as $V_c$ approaches the plasma potential $\phi_p$. The dotted line is the estimated prediction from the Crooks and O'Neil theory; the solid line is the exact, numerically calculated prediction.

experiment, the plasma radius was changed by expanding the plasma column while keeping the total number of electrons, $N$, constant. Thus, as the plasma radius increased, the density decreased. Since $\gamma$ is nearly independent of density, only the change in $R_p$ should affect the damping rate. [In this plot, $R_p$ is defined as the radius of a uniform density column required to give the measured $N$ and density averaged over P1.] The damping rate increases with $R_p$ because a wider plasma extends farther over the curvature of the confining equipotentials. The difference in slope between the dotted and solid curves in Figure 4.14 is due to a decrease in $\delta L$ with $R_p$ that is not accounted for in $\gamma_{est}$. The dependence of $\delta L$ on $R_p$ and $T$ is

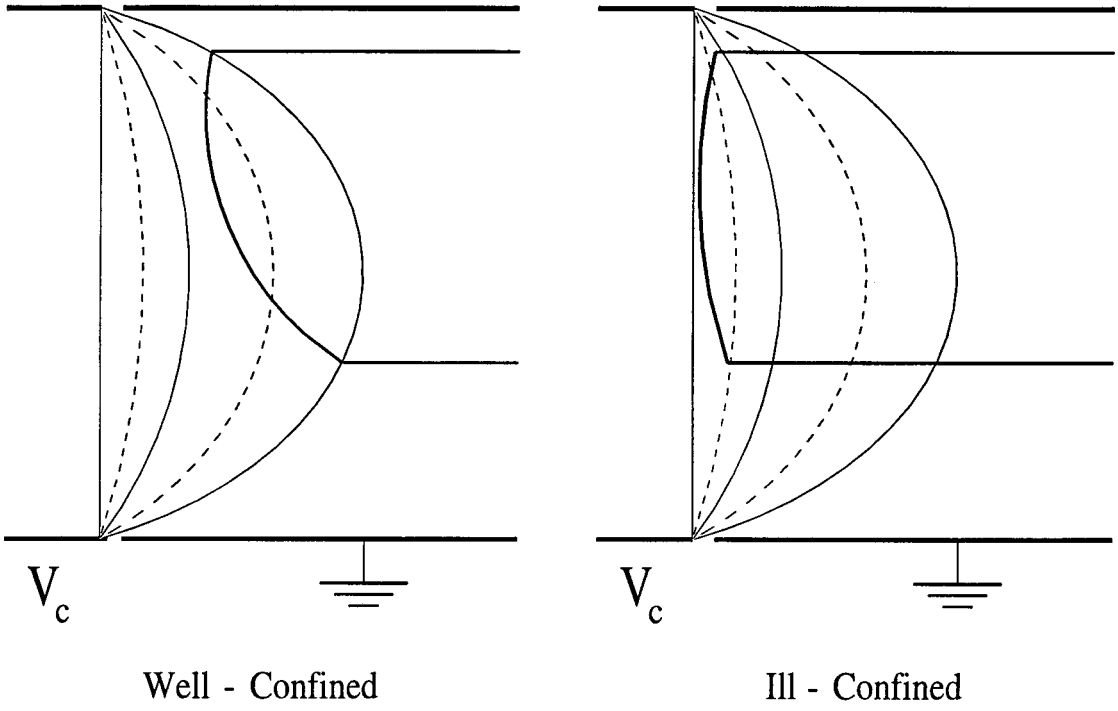


**Figure 4.12:** The decrease in the curvature of the confining equipotentials near the confinement boundary gives an ill-confined plasma ($V_c \sim \phi_p$) a smaller $\delta L$ than a well-confined plasma ($|V_c| \gg |\phi_p|$).

discussed in Appendix B.

### Plasma Length

The dependence of $\gamma$ on the mean plasma length, $L_p$ (defined in Equation 2.12), is shown in Figure 4.15. The decrease in $\gamma$ with $L_p$ is easily understood; the longer the plasma, the less the shape of its ends affects the electron orbits. The slight ripples in the data in Figure 4.15 are a systematic error; I was not able to keep the density profile exactly constant as I changed $L_p$. The fact that $\gamma_{rp}$ follows these ripples demonstates the accuracy of the numerically calculated 3-D density and potential profiles.

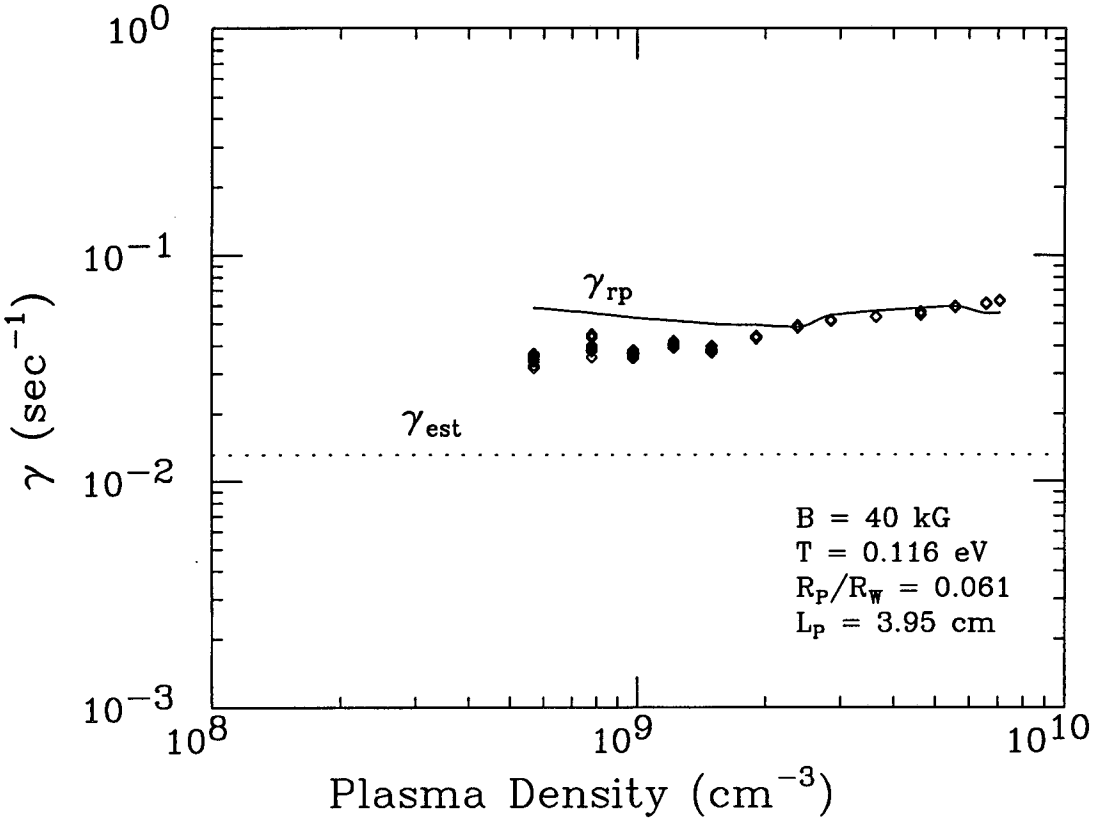


**Figure 4.13:** The damping rate of the $m = 1$ diocotron mode is nearly independent of density. The dotted line is the estimated prediction from the Crooks and O'Neil theory; the solid line is the exact, numerically calculated prediction.

## 4.6 Low Temperature Effects

### 4.6.1 Resonant Particles

Crooks and O'Neil predict that when the bounce frequency of a thermal electron is less than the rotation frequency, i.e. $2\pi\overline{f_B} \equiv \overline{\omega_B} < \omega_R$, the bounce motions of the electrons are no longer an adiabatic invariants, and $\gamma_{rp}$ is greatly enhanced by electrons whose bounce and rotation frequencies are resonant. If, for example, an electron's bounce frequency is one-half $\omega_R$, it will always hit each end of the plasma at the same place and increase (or decrease) in energy with each bounce. This causes a larger cyclic variation in $T_{||}$, which causes more energy to be scattered

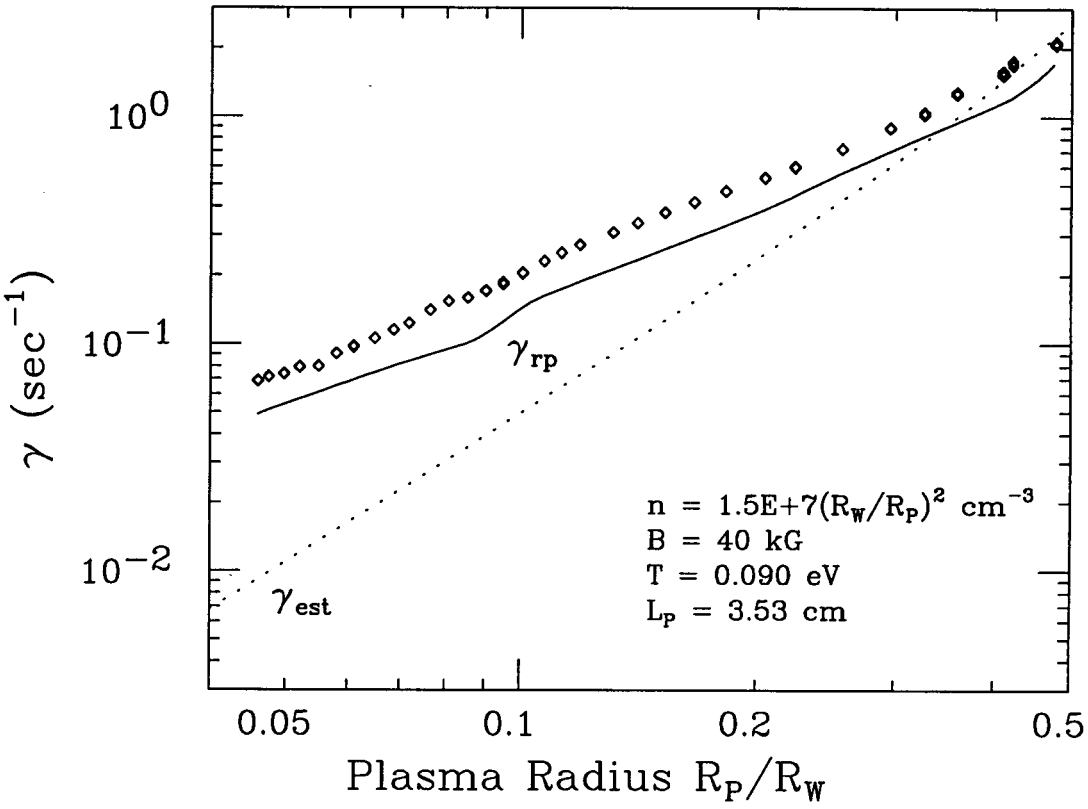


**Figure 4.14:** The damping rate of the $m = 1$ diocotron mode increases with plasma radius. The dotted line is the estimated prediction from the Crooks and O'Neil theory; the solid line is the exact, numerically calculated prediction.

into $T_\perp$ and increases the irreversible heating. The ratio of the resonant particle flux to the non-resonant, adiabatic flux in the Crooks and O'Neil theory is given by

$$\frac{\Gamma_\rho^{res}}{\Gamma_\rho^{adb}} = \sqrt{\frac{9\pi}{8}}\,\frac{\omega_R}{3\nu_{\perp\parallel}}\left(\frac{\omega_R}{2\overline{\omega_B}}\right)^5 \exp\left[-\frac{1}{2}\left(\frac{\omega_R}{2\overline{\omega_B}}\right)^2\right]. \tag{4.23}$$

The resonant particle flux is independent of $\nu_{\perp\parallel}$; it depends on collisions only to knock particles in and out of resonance. Note that resonance here means $\omega_R = 2\omega_B$. Electrons with $\omega_R = \omega_B$ will increase in energy at one end of the plasma but decrease at the other end.

The resonant particle contribution to the theoretical damping rate is small for most of the data in this thesis. This is because the ratio $\omega_R/\overline{\omega_B}$ has a maximum

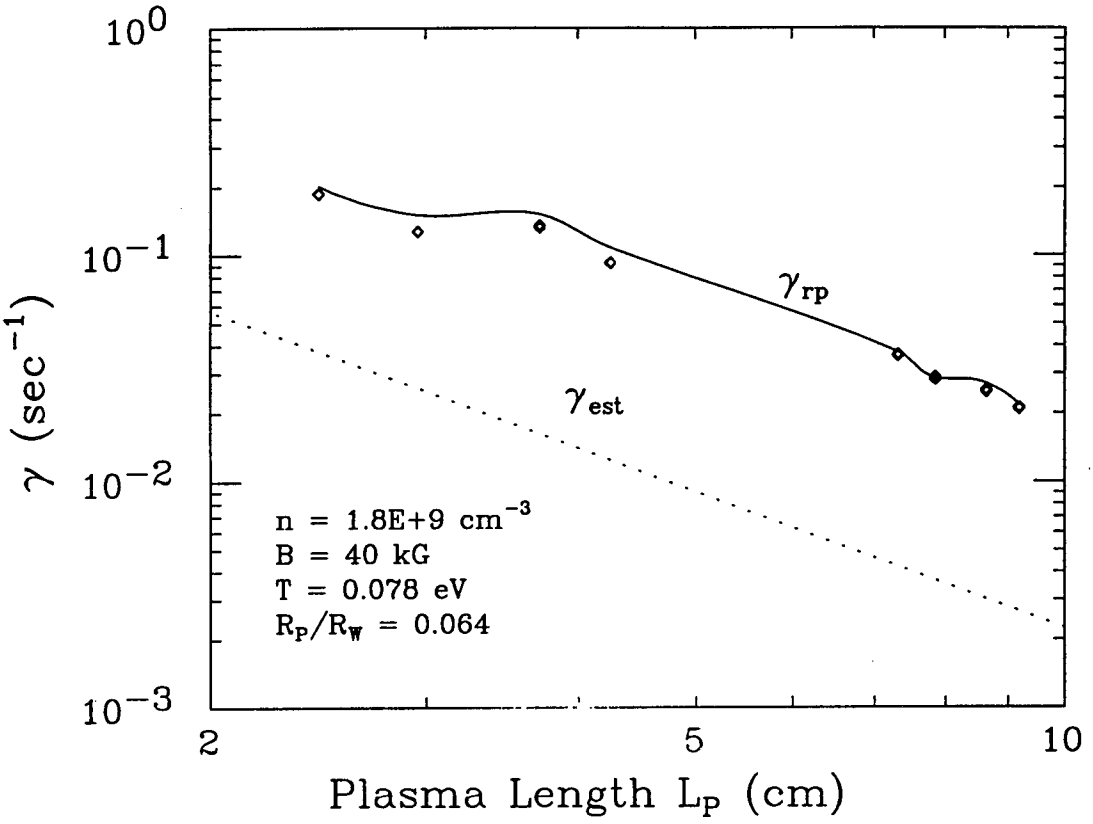


**Figure 4.15:** The damping rate of the $m = 1$ diocotron mode decreases with plasma length. The dotted line is the estimated prediction from the Crooks and O'Neil theory; the solid line is the exact, numerically calculated prediction.

value of about 1.5 in CV plasmas, so there are usually few resonant particles and they are near zero energy in the Maxwellian distribution. However, even when a large resonant particle enhancement to $\gamma$ is predicted, it is not observed experimentally. This is demonstrated in Figure 4.16, which shows the measured dependence of $\gamma$ on $T$ for 2 data sets taken at $B = 40$kG. (The data in Figure 4.8 was taken at $B =$ 60kG.) The measured damping rate decreases as $r_c$ becomes smaller than $b$, just as in Figure 4.8. Comparing the measured rates to $\gamma_{rp}$ indicates that the actual plasma temperature for the left-most points is given by the low temperature extreme of the error bars. The theoretical damping rate including the resonant particle contribution is shown by the dashed curve labeled $\gamma_{res}$. It diverges from the data at temperatures

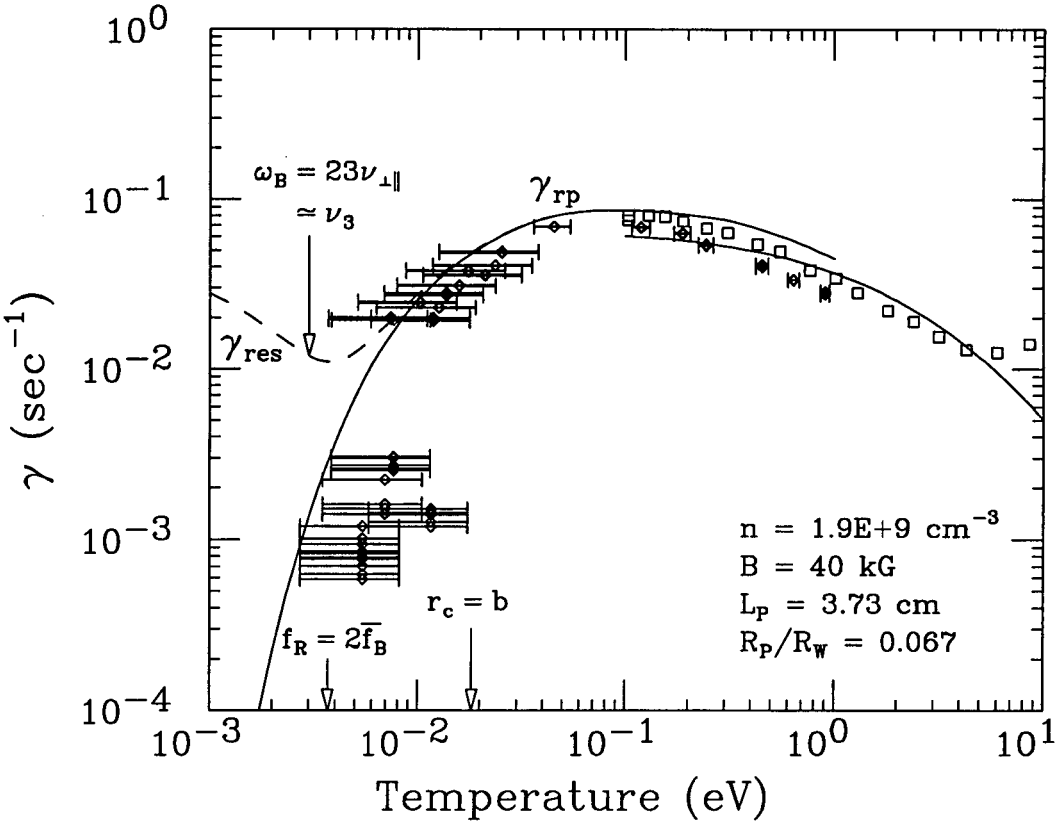


**Figure 4.16:** The damping rate is not enhanced by resonant particles due to the high collisionality of the plasma. The dashed line is the prediction of Crooks and O'Neil's resonant particle theory. It diverges from the data when $f_R > 2\overline{f_B}$. The 2 data symbols correspond to 2 different data sets. The plasma parameters are for the low temperature data.

below 0.05 eV; increasing with decreasing temperature while the data decreases. The reason for this discrepancy is probably due to the high collisionality of the plasma. The effective collision rate at which electrons are knocked out of resonance is given by

$$\nu_{eff} \approx \nu_{\perp\parallel} \left( \frac{\overline{\omega_B}}{\Delta\omega_B} \right)^2, \tag{4.24}$$

where $\Delta\omega_B$ is the width of the bounce-rotation resonance in velocity space. This width is determined by the effective colision rate, i.e.

$$2\Delta\omega_B \approx \nu_{eff}. \tag{4.25}$$

Combining these two equations yields an expression for $\nu_{eff}$

$$\frac{\nu_{eff}}{2\overline{\omega_B}} \approx \left(\frac{\nu_{\perp\parallel}}{\overline{\omega_B}}\right)^{1/3}. \tag{4.26}$$

The resonant particle transport theory applies only if $\nu_{eff} \ll 2\overline{\omega_B}$. For the data point at $T = 0.003$ eV in Figure 4.16, Equation 4.26 gives $\nu_{eff} \approx 0.7\overline{\omega_B}$. Thus, despite being strongly magnetized, the electrons probably collide often enough to destroy resonances. However, resonant particle rotational pumping may be important in less collisional plasmas in other experiments, such as those described in References [38] and [23]. (Measurements of plasma heating presented in Appendix A support this idea.)

### 4.6.2 Three Body Collisions

Three body collisions should destroy bounce-rotation resonances, even if binary collisions are too weak. The three body collision rate can be estimated [1] by

$$\nu_3 \approx g\, n b^2 \bar{v}. \tag{4.27}$$

The plasma parameter, $g$, is given by

$$g = \left(\frac{3b}{a}\right)^{3/2}, \tag{4.28}$$

where $a \approx n^{-1/3}$ is the mean inter-electron spacing. For the data point at $T = 0.003$ eV in Figure 4.16, Eqs. 4.28-4.27 give $g \approx 0.15$ and $\nu_3 \approx 23\nu_{\perp\parallel} \approx \overline{\omega_B}$. The 3 body collision rate is not suppressed at low temperatures as is $\nu_{\perp\parallel}$. Thus, the parallel velocity distribution relaxes to a Maxwellian through 3 body collisions much faster than through binary collisions. While 3 body collisions can wash out resonances, they do not change $\nu_{\perp\parallel}$, as is demonstrated by the agreement between the data and the adiabatic theory in Figure 4.8 and Figure 4.16.

### 4.6.3 The Fluid Limit

The close agreement between the adiabatic theory and the data in Figures 4.7-4.16 when $\overline{\omega_B} < \omega_R$ is unexpected for 2 reasons. First, the bounce motion of the electrons is not an adiabatic invariant as Crooks and O'Neil assume. Second, the bounce motion of the electrons is not rapid enough to keep the plasma in local thermal equilibrium along each magnetic field line, as is assumed in the numerical calculation of the $z$-dependence of $n$ and $\phi$. The adiabatic theory still works in this regime probably for the same reason that the resonant particle theory doesn't work. The high collisionality of the plasma prevents the rapid variation in the length of a tube of plasma from driving the plasma far from thermal equilibrium. In this regime, the plasma is better viewed as a fluid, and the transport and irreversible heating caused by rotational pumping can be viewed as dissipation of a compressible flow by a "second" or "bulk" viscosity. In the guiding center approximation, the cyclotron motion of the electrons is a "hidden" degree of freedom, like the vibrations and rotations of gas molecules [35]. Equilibration of hidden and translational degrees of freedom gives rise to a second viscosity [36]. The rate of dissipation by the second viscosity in a compressible fluid is given by

$$\frac{3}{2}\frac{d}{dt}(nT) = \zeta(\nabla\cdot\mathbf{v})^2. \tag{4.29}$$

The second viscosity coefficient, $\zeta$, can be obtained for a single species plasma by deriving Equation 4.12 without assuming $\omega_R \gg \nu_{\perp\parallel}$ and comparing it to the time average of Equation 4.29; $\zeta$ can then be expressed as

$$\zeta = \frac{4}{9}\frac{nT}{\nu_{\perp\parallel}}\frac{1}{1+(\omega_R/3\nu_{\perp\parallel})^2}. \tag{4.30}$$

In my experiments, $\gamma$ is independent of $\omega_R$ because $\omega_R \gg \nu_{\perp\parallel}$ and $\mathbf{v} \propto \omega_R$. In the inaccessible opposite limit where $\omega_R \ll \nu_{\perp\parallel}$, $\zeta$ resembles Braginskii's [3] parallel

electron viscosity coefficent, which can be written as

$$\eta_0 \approx \frac{nT}{\nu_{ee}}, \tag{4.31}$$

where $\nu_{ee}$ is the electron-electron collision rate. Braginskii derives $\eta_0$ in the fluid limit where $\nu_{ee}^{-1}$ is shorter than any macroscopic timescales. One may then naively wonder, since $\eta_0 \propto T^{5/2}$, if it is *this* viscosity which is responsible for the strong increase in $\gamma$ with $T$ at low temperatures in Figure 4.8 and Figure 4.16, where $\nu_{ee} > \omega_R$. Braginskii's calculation, however, is performed in the limit of weak magnetization, where $\lambda_D \ll r_c$. In confined nonneutral plasmas, the opposite condition holds, i.e., $\lambda_D \gg r_c$, and $\nu_{ee}$ in Equation 4.31 must be replaced by $\nu_{\perp\parallel}$. Thus, Braginskii's parallel viscosity is the low frequency limit of what I have called a second viscosity.

Braginskii worked in this limit so that he could assume that the distribution function was nearly Maxwellian. For the case of rotational pumping, however, this is unneccesarily restrictive as long as the plasma is cold enough that the Debye sheath at the plasma ends is very short, i.e. $\lambda_D \ll L_p$. The electrons then travel along the magnetic field lines as if they are in a square potential well. The rotation of the plasma through the confining potentials causes a cyclic variation in the length of the well, $\delta L$, but the variation is independent of the energies of the individual electron. Thus, if $\overline{\omega_B} > \omega_R$, the conservation of each electrons bounce adiabatic invariant keeps the parallel velocity distribution a Maxwellian even in the abscence of collisions. If $\overline{\omega_B} \leq \omega_R$ resonances can occur, but a high enough collision rate will destroy the resonances and keep the velocity distribution a Maxwellian.

## 4.7 High Temperature Effects

When the Debye length in the plasma becomes large, i.e. $\lambda_D \sim R_p$, the agreement between the rotational pumping theory and experiment begins to weaken. This can be seen at the highest measured temperatures in Figs. 4.8 and 4.16. The exper-

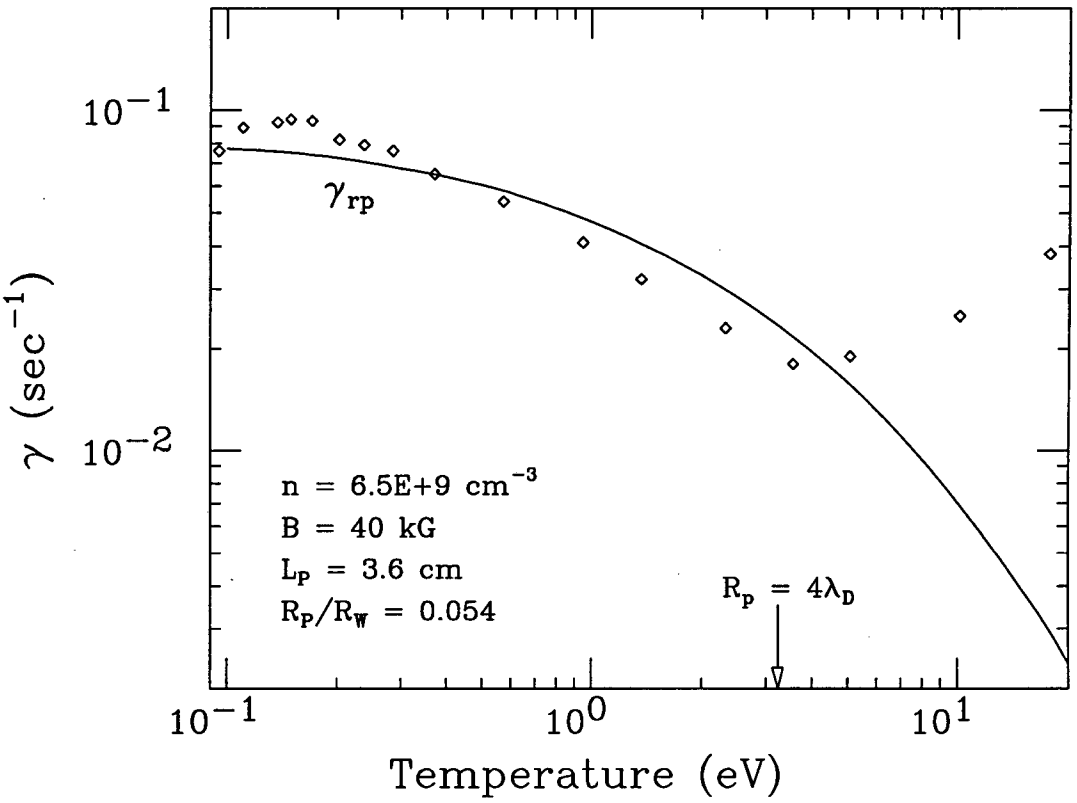


**Figure 4.17:** The measured damping rate increases with temperature, diverging from $\gamma_{rp}$, when $\lambda_D$ becomes comparable to $R_p$.

imental $\gamma$ starts to increase with temperature, while the theory predicts a continued decrease. This discrepancy is even more evident in Figure 4.17, which shows the dependence of $\gamma$ on high temperatures. The agreement with the Crooks and O'Neil theory is similar to that for the moderate temperature points in Figure 4.16, but the high temperature discrepancy is unmistakable. The measured value of $\gamma$ is a factor of 10 higher than the theory at 18 eV. For all three data sets, this discrepancy occurs when $\lambda_D \sim R_p$, i.e. when the kinetic and potential energies of the electrons are comparable.

Crooks and O'Neil's assumption that the plasma has "hard" ends (Equation 4.7) is inapplicable at high temperatures, where the Debye sheath at the plasma

ends is much larger than $\delta L$. A possible explanation of the increase in $\gamma$ in this regime comes from the dependence of the electrons' $\mathbf{E} \times \mathbf{B}$ orbits on their parallel energy, $E_{||}$. As noted in Section 4.5.2, a high energy electron will penetrate farther into the confining potentials, and be affected by different electric fields, than a low energy electron. Thus, the $\mathbf{E} \times \mathbf{B}$ rotation frequency of the plasma, $\omega_R$, and the $m = 1$ diocotron frequency, $\omega_d$, are functions of $T_{||}$. In addition, there is a thermal spread in the bounce-averaged $\mathbf{E} \times \mathbf{B}$ velocities of the individual electrons, and this spread becomes more pronounced as $T_{||}$ increases.

Despite the thermal spread in the $\mathbf{E} \times \mathbf{B}$ velocities, the rapid rotation of the plasma prevents the "smearing out" of the plasma which was observed by Peurrung [49]. For example, the measured $m = 1$ diocotron frequency, $\omega_d$, for the T=18 eV data point in Figure 4.17 is about 5% higher than at T=0.2 eV. The thermal spread in $\omega_d$ is presumably about 5% as well. The damping time is still greater than $10^5$ diocotron periods, however, indicating that the thermal spread in $\omega_d$ averages out to zero over a plasma rotation.

Although the plasma does not smear out, the thermal spread in $\omega_R$ may still effect the rotational pumping damping rate. I can obtain $\omega_R(\rho)$ from the $\phi(x, y, x)$ calculated from the measured $n_z(\rho)$ and $T_{||}$. For the data in Figure 4.17, I find that $\omega_R$ decreases with temperature, indicating that $\omega_R$ for individual electrons decreases with $E_{||}$. This means that electrons with $E_{||} > kT_{||}/2$ will drift slower than a tube of plasma $\mathbf{E} \times \mathbf{B}$ drifting at the thermal $\omega_R$ while electrons with $E_{||} < kT_{||}/2$ will drift faster. Thus, if the tube $\mathbf{E} \times \mathbf{B}$ drifts up a gradient in $T_{||}$, the electrons drifting into the tube have more energy than those drifting out. This effect would tend to amplify the variation in $T_{||}$ in the tube during rotational pumping, causing a larger exchange in energy between $T_\perp$ and $T_{||}$, and thereby increasing $\gamma$.

Modeling the the thermal spread in $\omega_R$ is beyond the scope of Crooks and

O'Neil's theory. While the 3-D plasma density and potential profiles can be found numerically, calculating the bounce-averaged $\mathbf{E} \times \mathbf{B}$ drifts as a function of $E_{||}$ would be extremely difficult. Calculating the effect of collisions on the electron orbits would then add another level of difficulty. Hence, the cause of the high temperature increase in $\gamma$ remains unknown.

## 4.8 Nonlinear Effects

All the damping rates presented so far in this Chapter were measured using small displacements, such that $D_0 \ll R_p$. When the initial displacement is large, i.e. $D_0 \geq R_p/2$, the damping is no longer exponential in time; the damping rate changes as $D$ decreases, as in Figure 4.2. However, this behavior is still explainable by Crooks and O'Neil's rotational pumping theory. Figure 4.18 shows the evolution of the measured damping rate $\gamma$ for the plasma evolution shown in Figure 4.2. The damping rate is initially small, increases by an order of magnitude over 7 sec, and then rapidly decreases over the final 3 sec. The fluctuations in $\gamma$ for $t < 2$ sec are due to measurement noise: the measurement period is much smaller than $\gamma^{-1}$. The solid curve is again $\gamma_{rp}$, calculated using the measured $D$, $n_z(\rho)$, and $T$. The measured rates are well-explained by the theory, indicating that the change in $\gamma$ is due to changes in $n(x,y,z)$, $\phi(x,y,z)$, and $T$.

The damping rate decreases after 7 seconds because the plasma has become strongly magnetized, i.e. $r_c \leq b$, as a result of cooling from cyclotron radiation. In this regime, $\gamma$ decreases strongly with the decreasing temperature. This dependence provides the only mechanism for a decrease in $\gamma$, as can be seen from the expression for $\gamma_{est}$ in Equation 4.22. As the plasma evolves, $D$ decreases, $R_p$ increases, while $B$ and $L_p$ remain nearly the same. Thus, any decrease in $\gamma$ must come from a decrease in $\nu_{\perp||}T$. Cyclotron cooling ensures that after a few radiation times, $dT/dt$

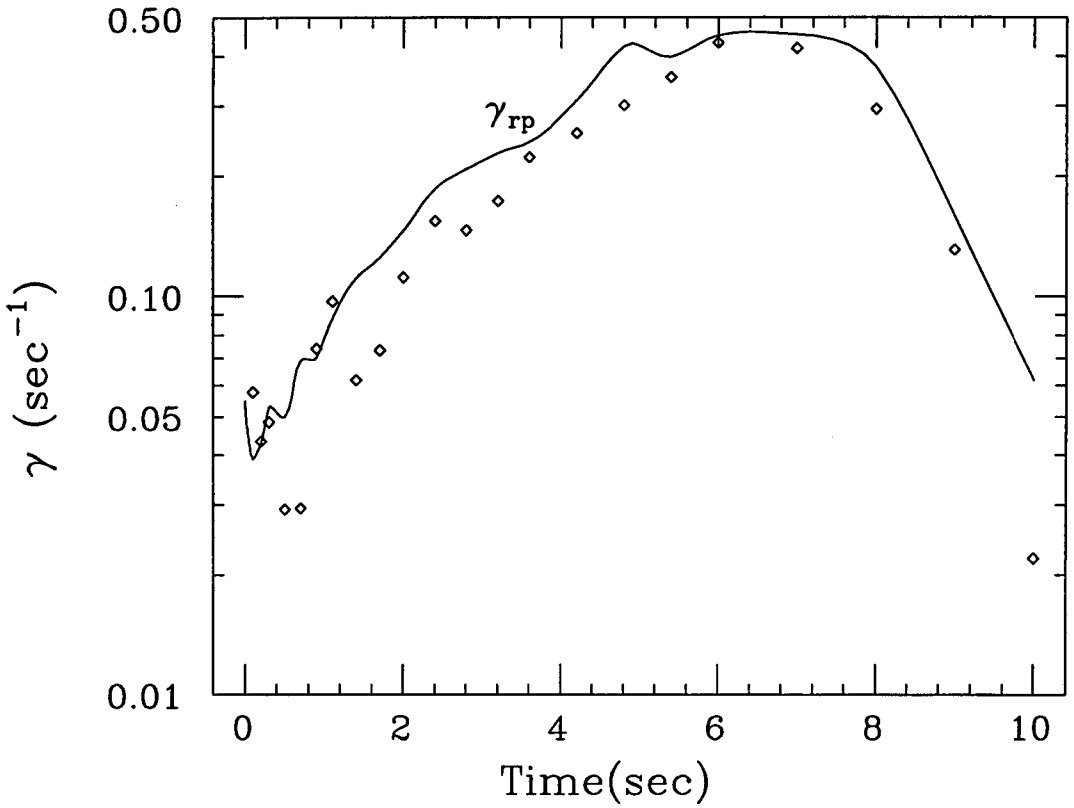


**Figure 4.18:** The damping rate for the evolution shown in Figure 4.2 changes with time but is still explainable by the rotational pumping theory. The damping rate rapidly decreases when the elecrons become strongly magnetized.

is negative. Therefore, $\nu_{\perp\|}T$ decreases only at temperatures where $d(\nu_{\perp\|}T)/dT$ is positive.; i.e. temperatures on the left-hand side of the peak in Figure 4.8. Thus, the change in $d\gamma/dt$ from positive to negative provides a signature, in the time evolution of $D$, of the transition to the strongly magnetized regime.

The transition to the strongly magnetized regime produces a nonlinear instability in the evolution of the plasma temperature. The rate of change of the temperature at a given radius $\rho$ is given by

$$\frac{dT}{dt} = \left[\frac{4}{3}\nu_{\perp\|}\left(\frac{\delta L}{L_0}\right)^2 - \frac{1}{\tau_{rad}}\right] T, \tag{4.32}$$

where the first term in the brackets is the heating from rotational pumping given by

Equation 4.12 and the second term is the cooling from cyclotron radiation. (Here I have assumed that $T_{\|} \approx T_{\perp} \approx T$.) The radiative cooling time, $\tau_{rad}$, is independent of temperature (as long as $T$ is large comnpared to the wall temperature), while $\nu_{\perp\|}$ peaks at the temperature where $r_c \approx b$ (as indicated by Figure 4.8). Therefore, there are two equilibrium temperatures where $dT/dt = 0$.

The stability of these equilibrium temperatures can be examined by linearizing Equation 4.32. Defining $T_0$ as an equilibrium temperature and $T_1 \ll T_0$ as a perturbation away from equilibrium, the rate of change of $T_1$ is given by

$$\frac{dT_1}{dt} = \left[\frac{4}{3} T \frac{d\nu_{\perp\|}}{dT} \left(\frac{\delta L}{L_0}\right)^2\right]_{T_0} T_1. \tag{4.33}$$

This equation shows that the high temperature equilibrium is stable because $d\nu_{\perp\|}/dT$ is negative for $r_c > b$. That is, increasing the plasma temperature decreases the rotational pumping heating rate, so the plasma cools back to the equilibrium temperature. Similarly, decreasing the temperature increases the rotational pumping heating rate, which also drives the plasma back to the equilibrium temperature.

Conversely, the lower equilibrium temperature is unstable because $d\nu_{\perp\|}/dT$ is positive when $r_c < b$. Increasing the temperature increases the heating rate, so that the plasma heats until the stable equilibrium temperature is reached. Similarly, if the temperature is decreased, the plasma unstably cools down to the minimum possible temperature, which is set either by the 4.2K wall temperature or by low-level heating from anomalous transport.

This nonlinear temperature instability can result in a bifurcation in the possible plasma evolutions, such as that shown in Figure 4.19. Two different observed time evolutions of $D$ are shown. The injection conditions for both evolutions were nearly identical, and the initial displacements differed by less than 1%. The two evolutions are the same over the first 16 seconds, but then diverge, until the displacement at $t = 50$ sec in branch A is over twice the displacement in branch B.

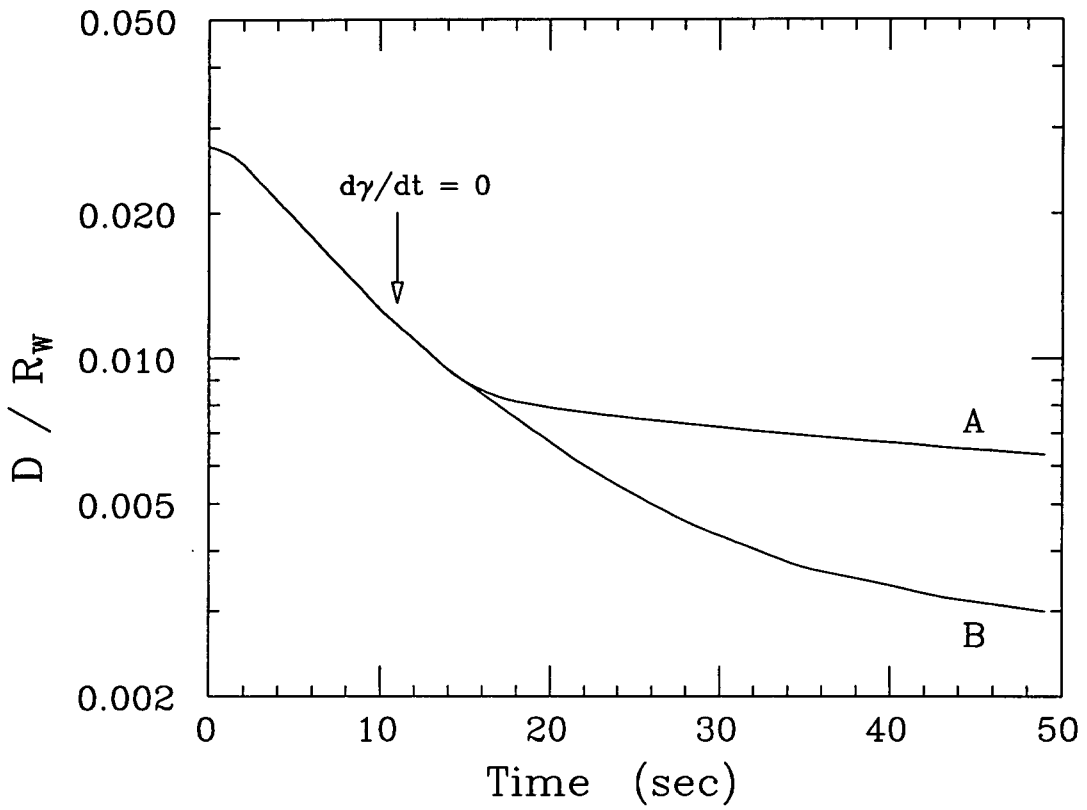


**Figure 4.19:** Bifurcation in the evolution of $D$ caused by temperature instability. Slightly different initial conditions result in 2 widely separated final states. The arrow shows where $\gamma$ starts decreasing.

The change in sign of $d\gamma/dt$ at $t = 11$ sec indicates that the electrons are becoming strongly magnetized.

The bifurcation presumably occurs because the plasmas following branch A reach the unstable temperature regime earlier than those following branch B. In branch A, $T$, and hence $\gamma$, unstably decreased at the branch point. The fact that the instability saturated before $\gamma$ went to zero is probably due to the weak Joule heating from anomalous transport. In branch B, the slightly different initial conditions presumably resulted in slightly stronger Joule heating at the branch point. Since $dT/dt$ is small in the stable temperature regime, this slight increase in heating caused $\gamma$ to remain large for a longer time, resulting in a smaller final displacement

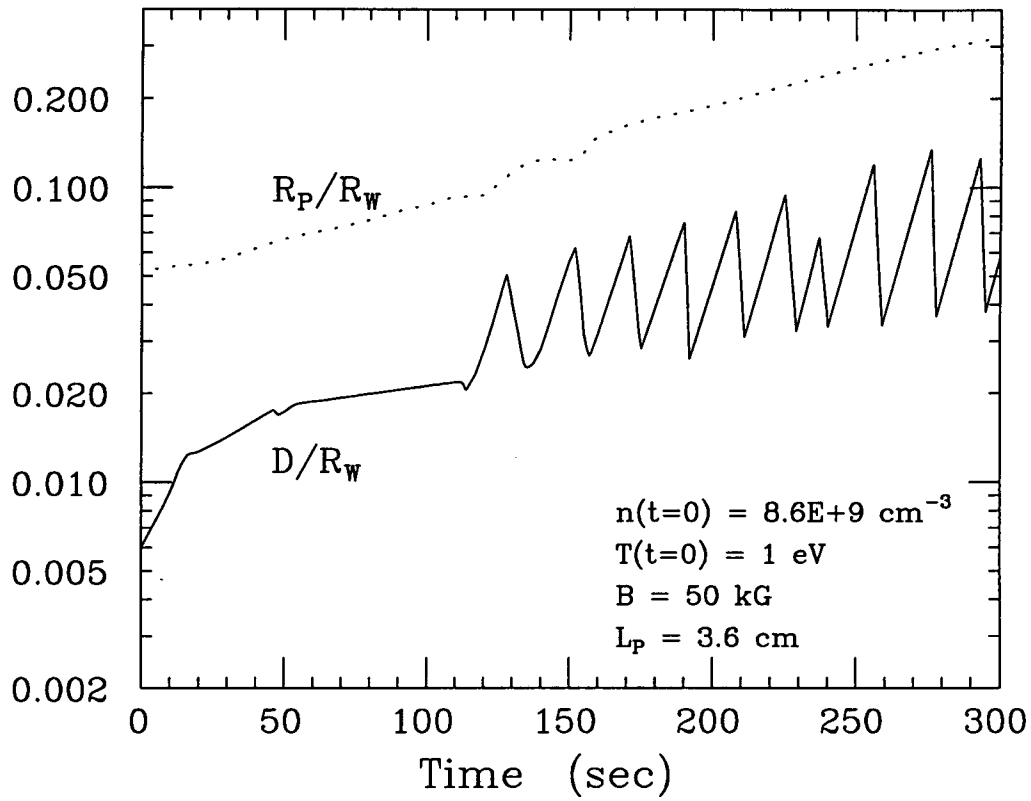


**Figure 4.20:** The evolution of the plasma displacment and radius during the "Dance of the Diocotron." The mode is driven by a 30 kΩ resistor attached to a sector probe. Electrons start being lost at 275 seconds, indicating the plasma is scraping the wall.

than branch A.

The nonlinear temperature instability also explains previously observed "saw-tooth" oscillations in the amplitude of a destabilized $m = 1$ diocotron mode [26]. Here, the diocotron mode is destabilized by attaching a resistor to a sector probe. The image charge currents in the sector probe dissipate energy in the resistor, causing the negative energy mode to grow [63]. The growth rate is nearly independent of changes in the plasma parameters caused by the evolution of the plasma.

Figure 4.20 shows the evolution of $D$ and $R_p/R_w$ that the results from the competition between rotational pumping damping and resistive growth. Initially,

the mode grows exponentially in time. This growth saturates after 20 seconds, and is followed by 90 seconds of much slower increase in $D$. At 110 seconds, the mode amplitude undergoes "sawtooth" oscillations, which have a period of about 20 seconds. These oscillations, sometimes called the "Dance of the Diocotron," can continue for thousands of seconds. The plasma radius slowly increases during the "Dance;" eventually, $D$ and $R_p$ become so large that electrons start being lost to the walls. This occurs at 275 seconds in Figure 4.20.

Despite its complexity, the basic features of the "Dance of the Diocotron" can be explained by the rotational pumping theory. To demonstrate this, I developed a simple computer program which models the evolution of a uniform density and temperature plasma under the influence of resistive growth [63], rotational pumping transport [Eqs. 4.12,4.14, and 4.22], and cyclotron cooling. This program includes the finite-length increase in the diocotron mode frequency [17], the effect of a finite wall temperature on radiation [1], and the dependence of the plasma end shape on $R_p$ [Figure B.3]. The program also includes the independently measured anomalous transport.

Given the initial conditions shown in Figure 4.20, the program calculates the plasma evolution shown in Figure 4.21. This simulation shows that the electrons become strongly magnetized within the first few seconds. Thus, the initial damping rate is small and $D$ increases at the resistive growth rate. Saturation occurs when $D$ has increased enough that the Joule heating term in Equation 4.32 overcomes the cyclotron cooling, increasing the temperature and the damping rate. (The decrease in $D$ from 20 to 30 seconds does not appear in the measured evolution shown in Figure 4.20, but was seen in many similar evolutions.) The slowness of the subsequent growth of $D$ indicates that the resistive growth is nearly balanced by rotational pumping damping. At the temperatures shown for this part of the evolution, both

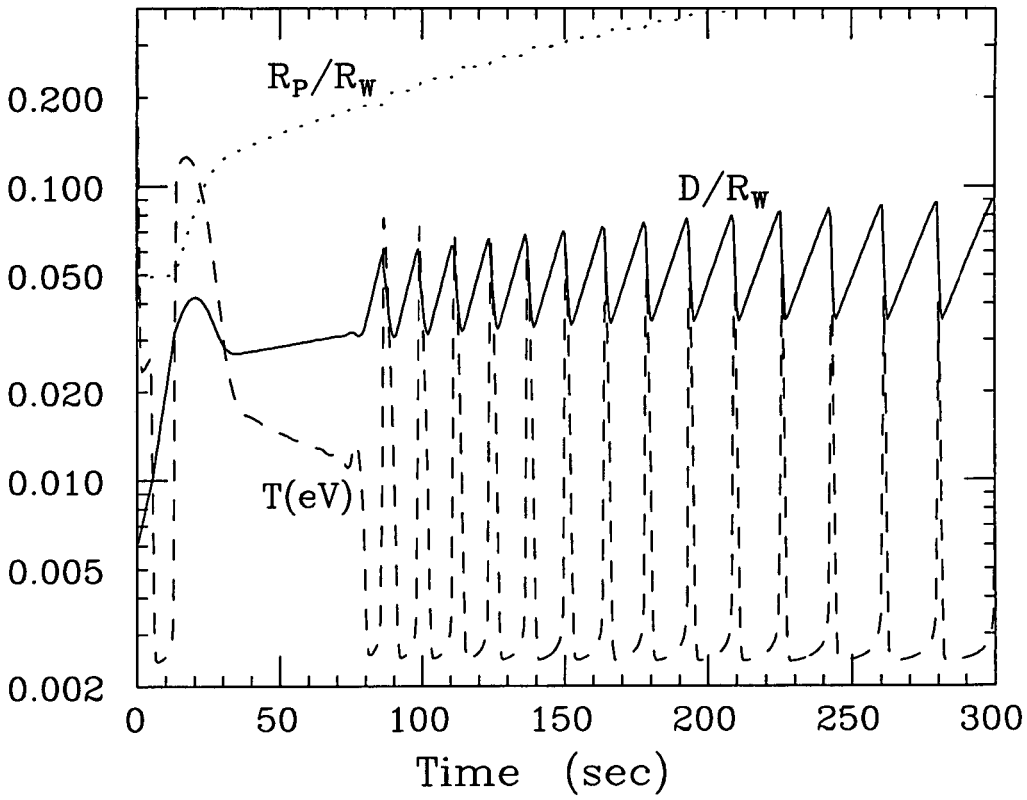


**Figure 4.21:** Computer simulation of the "Dance of the Diocotron," given the initial conditions shown in Figure 4.20. The basic features of the measured evolution are reproduced. The sawtooth oscillations are caused by unstable oscillations in the plasma temperature.

$dT/dt$ and $d\nu_{\perp\parallel}/dT$ are small because $r_c \approx b$, so that $\gamma$ stays nearly constant from 30 to 75 seconds, at which time the sawtooth oscillations begin.

The oscillations occur because the temperature can unstably grow as well as decrease. The damping rate is small when the plasma is at a low temperature such that $r_c \ll b$. The displacement $D$ then increases at the resistive growth rate. Eventually, $\delta L \propto D$ becomes large enough that the rotational pumping heating rate at the lowest possible temperature is larger than the cooling rate, causing the temperature to unstably increase. The accompanying increase in $\gamma$ causes $D$ to decrease until the plasma cools off again. This cycle is then repeated.

The form of the "Dance of the Diocotron" is strongly dependent on the minimum possible plasma temperature. If the minimum temperature is too low, the damping rate becomes so small that the diocotron mode simply grows until the plasma hits the wall. In Figure 4.21, the minimum temperature is set by the low-level heating caused by slow anomalous transport. In the simulation, the minimum temperature can also be set by changing the wall temperature, $T_w$. Figure 4.22 shows the evolution of $D/R_w$ at wall temperatures of 17K, 29K, and 45K, with the anomalous transport rate set to zero. As $T_w$ increases, the height of the initial rise in $D$ decreases; also, the sawtooth oscillations become weaker, increase in frequency, and start later in time.

Raising $T_w$ increases the minimum $\nu_{\perp\|}$, which decreases the time required for the temperature to unstably increase to the point at which rotational pumping damping overcomes resistive growth. Thus, the period of the sawtooth oscillations decreases. Since the resistive growth rate is independent of $T_w$, the amplitude of the oscillations decreases as the period increases.

Similarly, the initial rise in $D$ gets damped out earlier as $T_w$ increases, which reduces the amount of radial expansion which occurs. The narrower plasmas stay hotter because they have larger $\delta L$ at a given $\rho$, as shown in Figure B.3; this causes the plasma to stay in the stable temperature regime longer, as indicated by the increase in the slow growth section of the evolution as $T_w$ increases. At high enough $T_w$, the temperature never reaches the unstable regime again, and the sawtooth oscillations never occur.

## 4.9 Alternative Theories

The close agreement between my measurements of $\gamma$ and the predictions of Crooks and O'Neil's theory, both in terms of the magnitude of $\gamma$ and its param-

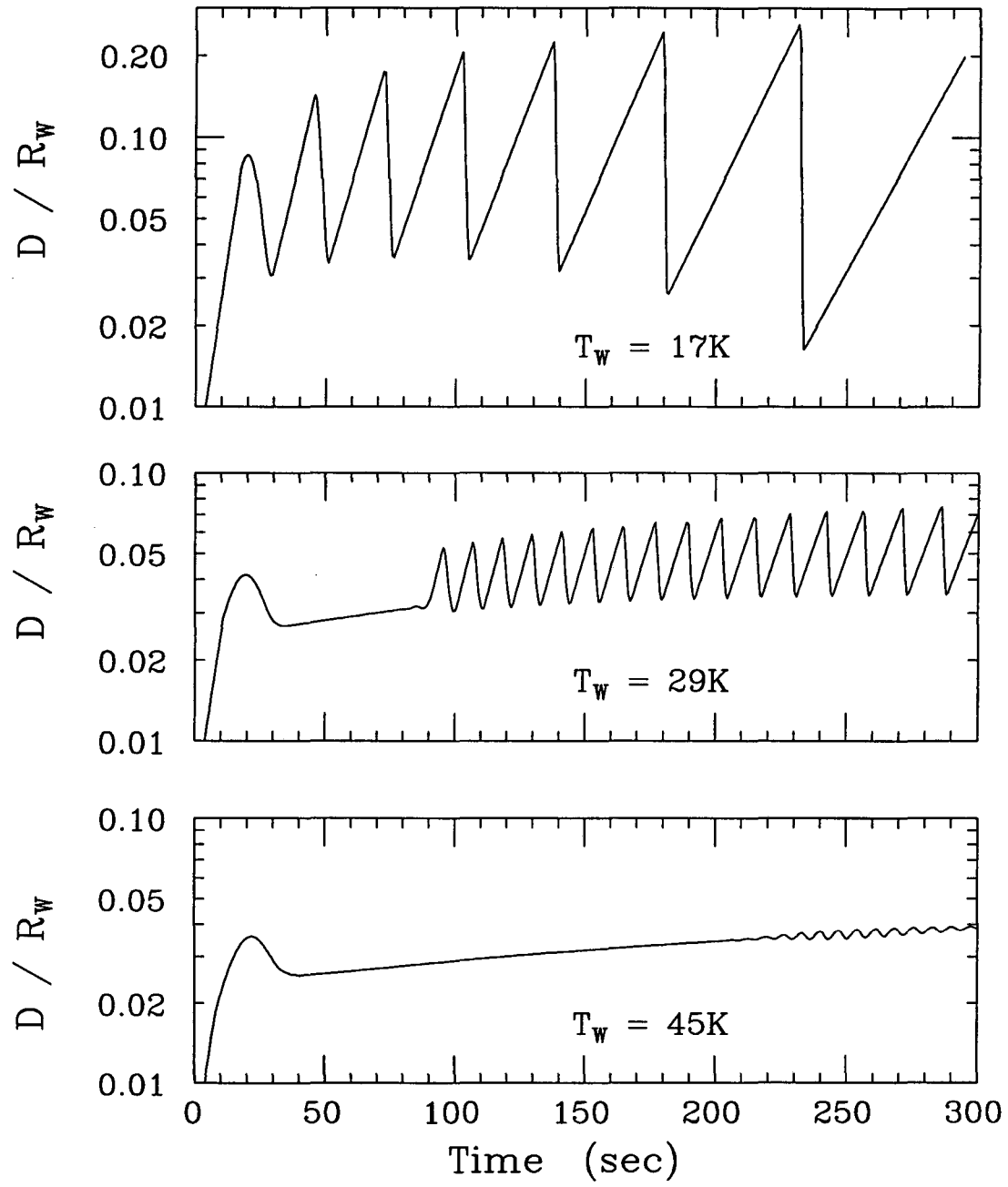


**Figure 4.22:** Simulations of the "Dance of the Diocotron" at 3 different wall temperatures, $T_w$, with the anomalous transport rate set to zero. As $T_w$ increases, the sawtooth oscillations become weaker, increase in frequency, and start later in time.

eter dependence, leaves little doubt that rotational pumping is responsible for the transport and damping which I observe. It is worthwhile, however, to examine other ideas about the damping of the $m = 1$ diocotron mode. The earliest theory, by Prasad and O'Neil [53], postulates that in a finite length plasma where $\overline{\omega_B} \ll \omega_R$, the $m = 1$ diocotron mode can couple to an $m = 1$ plasma mode. The plasma mode will Landau damp, providing a sink for the energy released by the damping of the diocotron mode. The predicted damping rate is approximately

$$\gamma \approx \frac{{\omega_p}^2}{{\omega_c}^2}\,\overline{\omega_B}\,\ln(\frac{2\omega_c}{\omega_p}) \sim \frac{nT^{1/2}}{B^2}, \tag{4.34}$$

where $\omega_c$ is the cyclotron frequency and $\omega_p$ is the plasma frequency. Besides the disagreement with the observed magnetic field scaling, this theory predicts values of $\gamma$ which are 2 to 3 orders of magnitude above the measured values. However, the condition $\overline{\omega_B} \ll \omega_R$ is never satisfied in CV plasmas, so this mode coupling probably never occurs.

Another possible damping mechanism is the shear, or "first", viscosity. As shown by Fine [18, 20], the electric fields from the image charges in the wall cause an off-axis plasma column to distort from a circular cross-section into an elliptical one. This causes shears in the $\mathbf{E} \times \mathbf{B}$ flow, which are acted upon by the shear viscosity, resulting in irreversible heating and a dissipation of electrostatic energy through expansion of the plasma. Conservation of $P_\theta$ results in the damping of the mode. In Appendix E, I calculate the damping rate from shear viscosity for an isothermal, uniform density plasma. This shear-driven transport is much smaller than rotational pumping, for 2 reasons. First, the elliptical distortions scale as $D^2$, while $\delta L$ scales as $D$. Second, theoretical [45, 46] and experimental [13] estimates of the shear viscosity coefficient show it to be much smaller than the second viscosity coefficient.

It has also been speculated that trap asymmetries may damp the $m = 1$ diocotron mode. I have found no evidence to support this idea. Except in the strongly

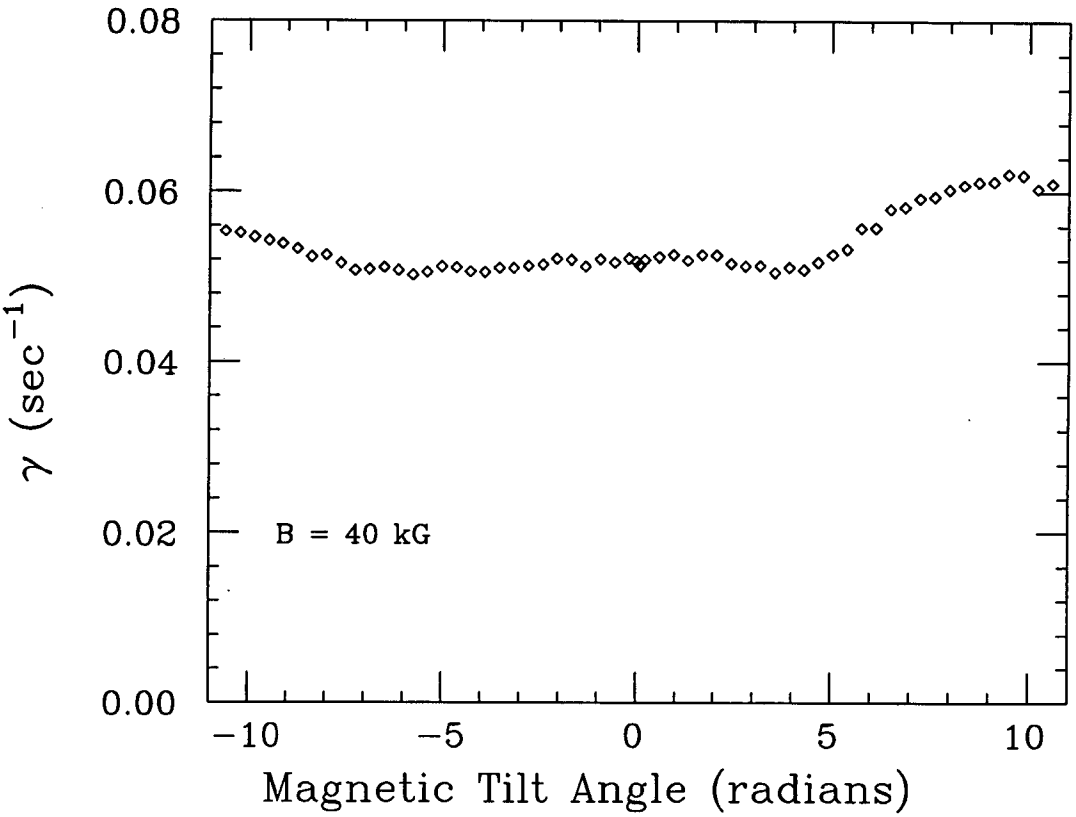


**Figure 4.23:** The damping rate of the $m = 1$ diocotron mode is insensitive to magnetic field tilt.

magnetized regime, $\gamma$ is nearly independent of magnetic field, whereas anomalous transport from inherent trap asymmetries decreases strongly with magnetic field. Externally induced asymmetries, such as misalignment between the magnetic field and the confinement cylinders, do not seem to affect $\gamma$ either. Figure 4.23 shows that the measured damping rate varies by less than 10% as the angle of magnetic field tilt varies over 10 milliradians, whereas the magnetic field in CV is aligned within 1 milliradian.

## 4.10 Further Consequences of Rotational Pumping

The damping of the $m = 1$ diocotron mode may be only the simplest effect caused by the rotational pumping mechanism. In Appendix D, I show how rotational pumping should also damp the $m \geq 2$ diocotron modes at nearly the same rate as the $m = 1$. It may also cause the dissipation of several otherwise stable nonneutral plasma configurations, including 2 electron vortex equilibria [40], vortex crystals [19], asymmetric equilibria [41, 42], and toroidal plasmas [34]. Rotational pumping may also damp asymmetric $\mathbf{E} \times \mathbf{B}$ flows in certain *neutral* plasma traps, such as non-axisymmetric magnetic mirrors [23, 28, 54]. Because the electrostatic and mechanical energy in neutral plasmas is small compared to their thermal energy, the effect of rotational pumping may be quite strong. The analagous process of "magnetic pumping" [60] is suspected to damp the poloidal rotation in tokamaks in an ion-ion collision time [59].

It is interesting to note that at temperatures around 0.1 eV, the damping rate of the $m = 1$ diocotron mode is nearly independent of $n$, $T$, and $B$, which are the usual parameters used to describe a plasma. The damping rate only depends on $R_p$ and $L_p$, parameters which describe the shape of the plasma's boundary. This points up the difference between the rotational pumping theory and the resonant particle transport theories described in Chapter 3. In both types of theories, the transport is caused by field asymmetries. The resonant particle transport theories describe these field asymmetries as extending over the entire plasma; the rotational pumping theory, on the other hand, assumes that the plasma shields out the field asymmetries, so that they only affect the shape of the plasma boundary.

# Chapter 5

# Squeeze Damping of the $m = 1$ Diocotron Mode

## 5.1 Overview

In this chapter, I present measurements of the damping of the $m = 1$ diocotron mode caused by the "squeeze" perturbation. The squeeze perturbation is an azimuthally symmetric, $z$-dependent electrostatic field asymmetry. It was originally observed by Fine [16] to strongly damp the diocotron mode. The reason for this damping is still unknown. In Section 5.2, I discuss how the squeeze pertubation is created and Fine's measurements of the damping of the diocotron mode.

In section 5.3, I present my own measurements of the squeeze damping of the diocotron mode and compare them to Crooks and O'Neil's rotational pumping theory [7]. I find, as did Fine, that for long enough plasmas, the damping is exponential in time and that the damping rate increases with the amplitude of the squeeze perturbation. Furthermore, I find that, for moderate to high temperatures, the damping rate decreases with temperature, increases with plasma radius, and scales only weakly with density. While the scalings with plasma parameters are predicted by rotational pumping theory, the scaling with squeeze voltage is not. In fact, the theory predicts that the squeeze perturbation decreases the damping rate of the $m = 1$ diocotron mode. This directly contradicts the experimental results. Finally, I

show that a squeeze perturbation can decrease the measured damping rate of short a plasma; this decrease is correctly predicted by the rotational pumping theory.

In section 5.4, I show that rotational pumping theory predicts a decrease in the damping rate because the squeeze perturbation decreases the cyclic variation in the length of a tube of plasma as it $\mathbf{E} \times \mathbf{B}$ drifts around the plasma axis. The squeeze voltage acts to reduce the curvature of the vacuum equipotentials, which reduces the radial electric fields at the plasma ends.

In section 5.5, I discuss how the squeeze perturbation may create non-Maxwellian variations in the parallel electron energy distribution. These variations are not included in the Crooks and O'Neil theory, and dissipation of these variations by collisions may be responsible for squeeze damping. I show numerical calculations of the plasma end shape which indicate that the effect of the squeeze perturbation on an electron depends on that electron's energy. Also, I find experimentally that squeeze damping is unaffected by the decrease in the anisotropic temperature equilibration rate, $\nu_{\perp\|}$, in the strong magnetization regime. This indicates that the collsions do more than just equilibrate the parallel and perpendicular temperatures $T_{\|}$ and $T_{\perp}$.

In section 5.6, I compare my data to two resonant particle transport theories. First, I show that the resonant particle contribution to rotational pumping does not improve the agreement of the Crooks and O'Neil theory with my data. I also discuss a "beat-wave" damping theory by Crawford and O'Neil [6, 5], to which Fine compared his results. I show that the assumptions of this theory are not in agreement with the experimental data; however, my data is not strong enough to totally disprove the theory.

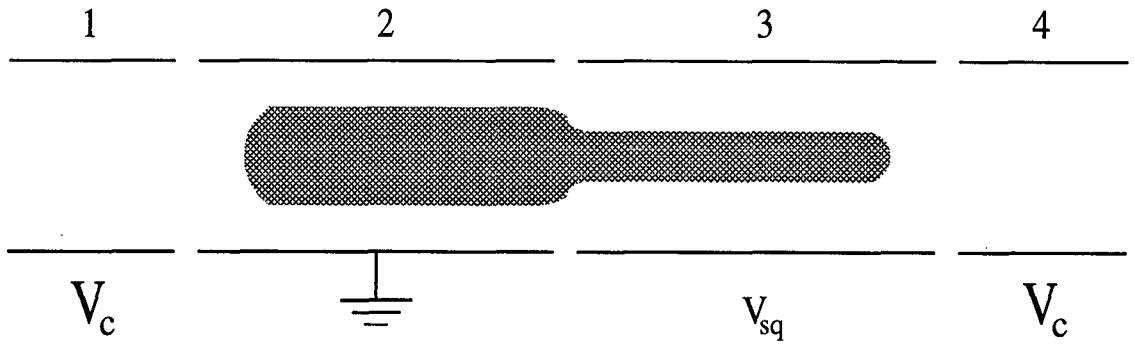


**Figure 5.1:** The "squeeze" perturbation. Applying $V_{sq}$ to one-half the plasma length squeezes the outer edge of the plasma into the grounded cylinder.

## 5.2 The Squeeze Perturbation

The squeeze perturbation is a static voltage applied to an azimuthally symmetric cylinder, shown schematically in Figure 5.1. A negative voltage, $V_{sq}$, is applied to the "squeeze cylinder" which contains half the length of the plasma. The electrons move to shield out the applied voltage, and the outer edge of the plasma is "squeezed" into the remaining grounded cylinder. Fine [16] discovered that when the squeeze perturbation is applied while an $m = 1$ diocotron mode is present, the mode rapidly damps. He observed that the total angular momentum, $P_\theta$, is conserved during the damping by an expansion of the plasma column. This is consistent with the fact that the squeeze perturbation is azimuthally symmetric. Fine also found that the displacement, $D$, decreased exponentially in time, i.e.

$$D(t) = D_0 \exp(-\gamma_{sq} t). \tag{5.1}$$

Finally, Fine observed that, for small amplitudes, the squeeze damping rate, $\gamma_{sq}$, scaled as

$$\gamma_{sq} \propto V_{sq}^2 B^{-2}, \tag{5.2}$$

and ranged between 0.1 $sec^{-1}$ and 1000 $sec^{-1}$ for the plasmas he studied on the EV machine at UCSD.

I have investigated squeeze damping of the $m = 1$ diocotron mode on the CV machine in order to compare it to the damping caused by rotational pumping. In my experiments, I confined the plasma in the cylinders L3-L5 shown in Figure 2.2; the length of this confinement region is $L_c = 10.16$ cm. The P5 collector plate was used to shield the P1-P4 collector plates from the ramping of the dump gate. This decreased the resolution of the radial profiles of wide plasmas. The squeeze voltage was applied to the L5 cylinder, which is 5.207 cm long. The plasma was injected, manipulated to the desired initial condition, and then moved off axis. The squeeze voltage was ramped to the desired magnitude over 50 msec, which is more than 100 diocotron orbits. The squeeze voltage then remained constant for the entire measurement period of 2-10 seconds. The temperature, $T$, of the plasma was maintained at a constant value by using only small displacements, i.e. $D \ll R_w$, and by applying a modulating voltage to cylinder L3 to balance cyclotron cooling. For each set of initial conditions, the damping rate of the $m = 1$ diocotron mode was measured both with the squeeze voltage applied to L5 and with L5 grounded.

## 5.3 Damping Rates

I have measured the dependence of the squeeze damping rate, $\gamma_{sq}$, on various plasma parameters. The damping rates are plotted in Figures 5.2-5.6 as squares. The measured damping rates with no squeeze, $\gamma_{ns}$, are plotted as diamonds. The dot-dash curves show the predictions of Crooks and O'Neil's rotational pumping theory for the damping rate of the squeezed plasmas, $\gamma_{rp}$.

The predictions of the rotational pumping theory for the squeezed plasmas were calculated in exactly the same way as they were for unsqueezed plasmas in Chap-

ter 4. Using the 3D Poisson-Boltzmann code described in Section 2.4.3, the density $n(x,y,z)$ and potential $\phi(x,y,z)$ were calculated from the measured $z$-integrated density $n_z(\rho)$, parallel temperature $T_{||}$, and displacement $D$, given the confinement voltage $V_c$ and the squeeze voltage $V_{sq}$. (Due to the lack of resolution caused by using P5 as a voltage shield, I assumed that $n_z(\rho)$ was a constant out to some $R_p$, except for the data shown in Figure 5.4.) These profiles were then put into the Crooks and O'Neil theory, and Equation 4.21 was numerically integrated to obtain the predicted rotational pumping damping rate $\gamma_{rp}$. I also performed this analysis for $V_{sq} = 0$ V. As expected, the theory correctly predicts the parametric dependence of $\gamma_{ns}$. However, the magnitude of the the predicted rates only agrees with the $\gamma_{ns}$ to within a factor of 2. This slight discrepancy is probably due to using a square density profile to approximate $n_z(\rho)$.

### 5.3.1 Displacement

I have found, like Fine, that the damping caused by the squeeze perturbation is exponential in time for small displacements. That is, $\gamma_{sq}$, like $\gamma_{ns}$, is independent of $D_0$, as shown in Figure 5.2. For this data, the squeeze voltage was $V_{sq}$= -16V, while the confinement voltage on the end cylinders was $V_c$ = -200V. For comparison, the space charge potential at the center of the plasma, $\phi_p$, was about -33V. These parameters give a squeeze damping rate $\gamma_{sq} \approx 0.2$ sec$^{-1}$, about an order of magnitude greater than the damping rate without squeeze.

While rotational pumping theory correctly predicts that the damping rate of the squeezed plasma should be independent of $D$, it gives the wrong damping rate. In fact, the Crooks and O'Neil theory predictes that the squeeze perturbation should reduce the damping rate by a factor of 5.

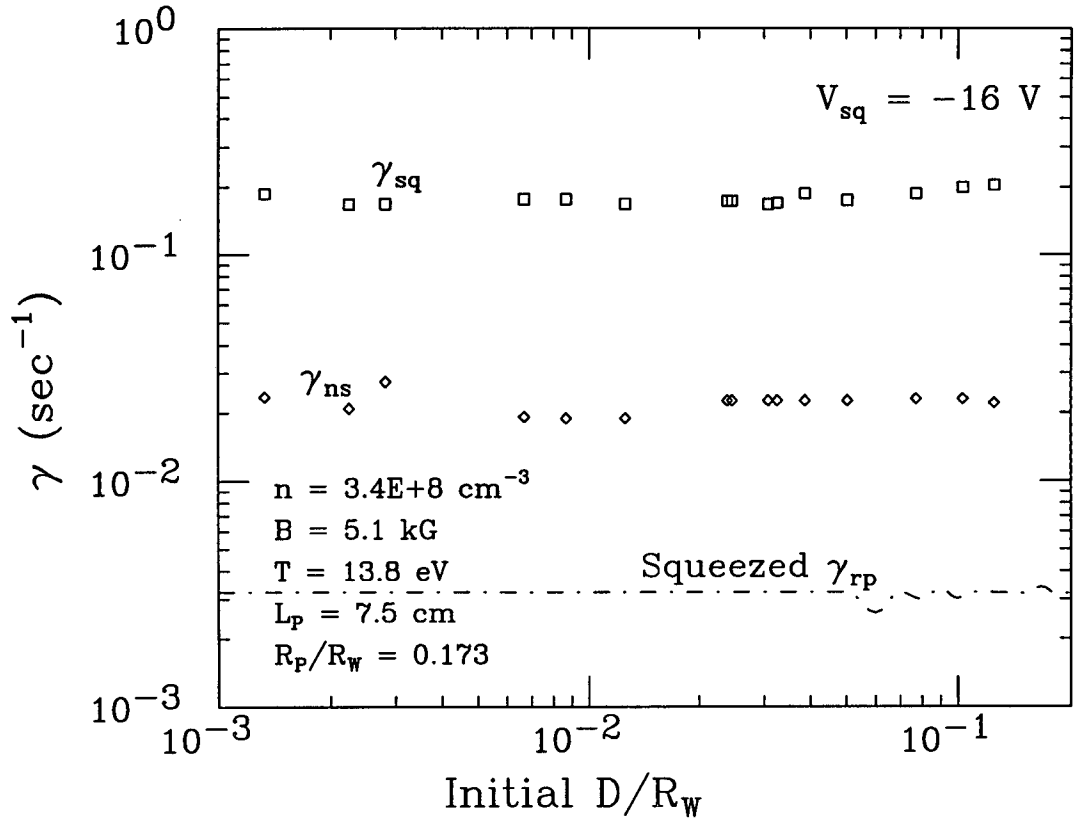


**Figure 5.2:** The squeeze damping rate is independent of displacement. The dot-dashed curve is the rotational pumping theory prediction for the squeezed plasma.

### 5.3.2 Squeeze Voltage

I find that the squeeze damping rate increases with the magnitude of the squeeze voltage, as shown in Figure 5.3. The plasma parameters of the plasma measured for this data were the same as those shown in Figure 5.2. As $|V_{sq}|$ is increased from 2V to 54V, $\gamma_{sq} - \gamma_{ns}$ increases by 2 orders of magnitude. The arrow on the left indicates the magnitude of $\gamma_{ns}$, while the arrow at the bottom shows the magnitude of $\phi_p$. For small squeeze voltages, the increase in the damping rate due to squeeze, $\gamma_{sq} - \gamma_{ns}$, increases as $V_{sq}^2$, as shown by the dashed line. This is consistent with Fine's measurements. When $V_{sq}$ becomes more negative than the space charge

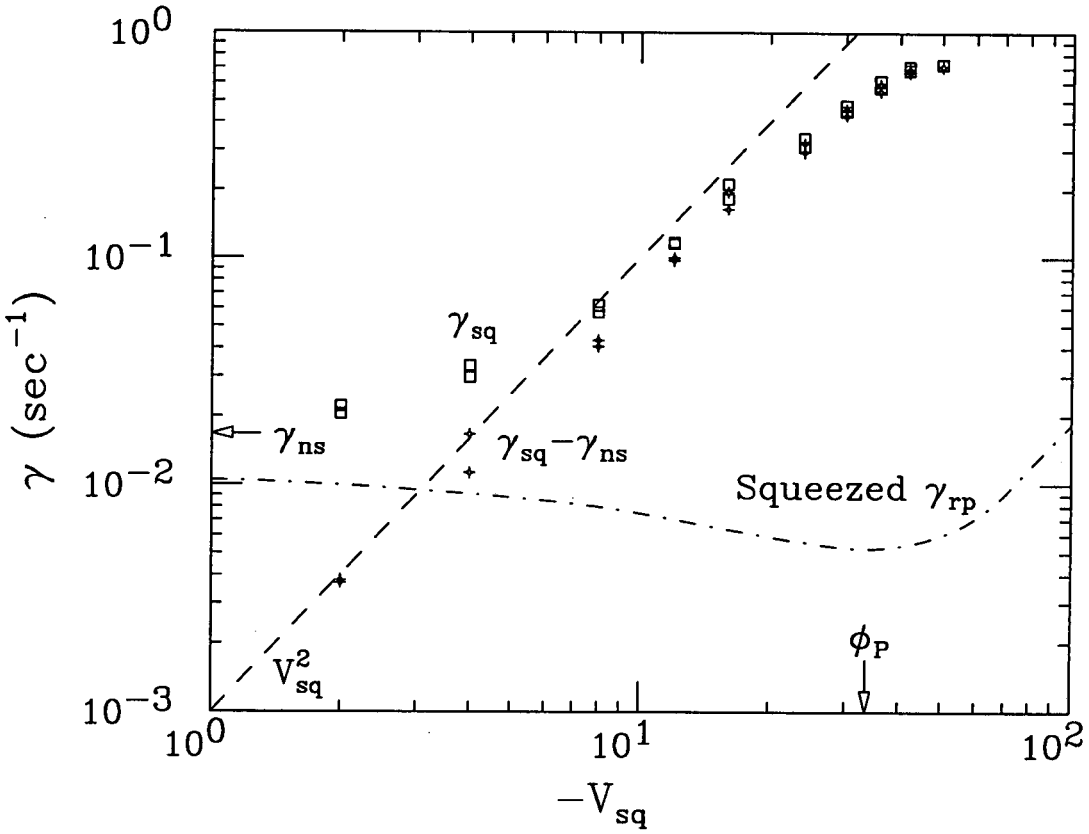


**Figure 5.3:** The change in damping rate induced by squeeze, $\gamma_{sq}$-$\gamma_{ns}$, increases as $V_{sq}^2$. The dependence of $V_{sq}$ weakens as $V_{sq}$approaches $\phi_p$. The dot-dashed curve is the rotational pumping theory prediction for the squeezed plasma. The plasma parameters are the same as in Figure 5.2.

potential, the squeeze damping rate scales less strongly with $V_{sq}$. At these squeeze voltages the plasma is getting squeezed out of the L5 cylinder. When $V_{sq}$ becomes comparable to $V_c$, the plasma should be entirely excluded from L5, and the squeeze damping rate presumably goes to zero. Fine also saw a similar decrease in the scaling of $\gamma_{sq} - \gamma_{ns}$ with $V_{sq}$, but at a lower magnitude of $V_{sq} \sim$ -1V.

The $V_{sq}^2$ scaling is consistent with linear perturbation theory. This is because, for $|V_{sq}| \ll |V_c|$, the damping rate cannot depend on the sign of the squeeze voltage. This can be seen by changing the definition of ground in Figure 5.1 by increasing all voltages by -$V_{sq}$. This does not change any of the physics, but now cylinder 3 is

grounded while cylinder 2 is at the positive voltage of -$V_{sq}$. Therefore, $\gamma_{sq}$ cannot scale as $V_{sq}$, and thus scales as $V_{sq}^2$, the next lowest order.

While the measured $\gamma_{sq}$ increase with -$V_{sq}$, rotational pumping theory predicts a decrease for all but the largest values of $|V_{sq}|$. The theoretical rate increases for $|V_{sq}|$ greater than 30V because the plasma is being pushed out of the L5 cylinder. Thus, the overall plasma length is decreasing, which increases the effect of rotational pumping. This is consistent with the measured decrease in the dependence of $\gamma_{sq}$ on $V_{sq}$ when $|V_{sq}| > |\phi_p|$. At large enough -$V_{sq}$, the squeeze perturbation is pushing the plasma out of the squeeze cylinder more than it is squeezing the plasma.

### 5.3.3 Temperature

I have also measured the dependence of $\gamma_{sq}$ on the plasma temperature, $T$, for moderate to high temperatures. Figure 5.4 shows that as $T$ is increased from 0.3 eV to 20 eV, the squeeze damping rate decreases about an order of magnitude, giving a scaling of $\gamma_{sq} \propto T^{-1/2}$. This is the same scaling as $\gamma_{ns}$ for 0.3 eV $< T <$ 4 eV. At higher temperatures, however, $\gamma_{ns}$ starts to increase with $T$ while $\gamma_{sq}$ continues to decrease, just as in Figure 4.17. Above $T$ = 10 eV, the squeeze perturbation actually decreases the damping rate. This indicates that the squeeze perturbation may somehow suppress the thermal spread in bounce averaged $\mathbf{E} \times \mathbf{B}$ drifts that was discussed in Section 4.7.

The decrease in $\gamma_{sq}$ with temperature may explain the decrease in $\gamma_{sq}$ at large displacements that was seen by Fine. As the diocotron mode damps, the plasma column expands in order to conserve angular momentum. This expansion causes Joule heating, and the larger the displacement the more the plasma must expand. Hence, $\gamma_{sq}$ should decrease with $D$ at large displacements, due to an increase in temperature. The same effect occurs in damping from rotational pumping, as shown in Figure 4.10.

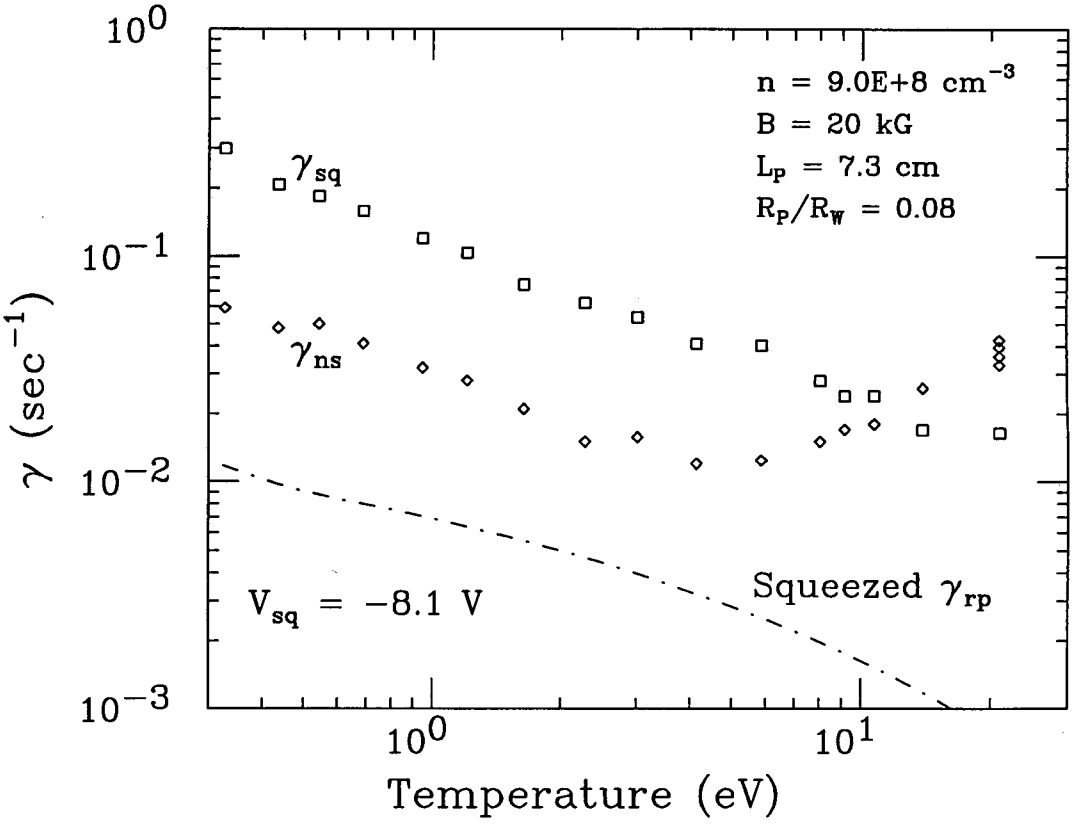


**Figure 5.4:** The squeeze damping rate decreases with temperature with same scaling as $\gamma_{ns}$ for temperatures below 4 eV. Squeeze suppresses the high temperature increase in the damping rate seen in $\gamma_{ns}$. The dot-dashed curve is the rotational pumping theory prediction for the squeezed plasma.

While Crooks and O'Neil's theory predicts the correct scaling of $\gamma_{sq}$ with temperature, it again predicts that the squeeze perturbation should reduce the damping rate. For this data, the theory prediction is a factor of 30 lower than the measured $\gamma_{sq}$.

### 5.3.4 Plasma Radius

To measure the dependence of $\gamma_{sq}$ on the plasma radius, $R_p$, I used the same method (described in Section 4.5.2) that I used to measure the dependence of $\gamma_{ns}$ on $R_p$. That is, I expanded the plasma column while keeping the total number of

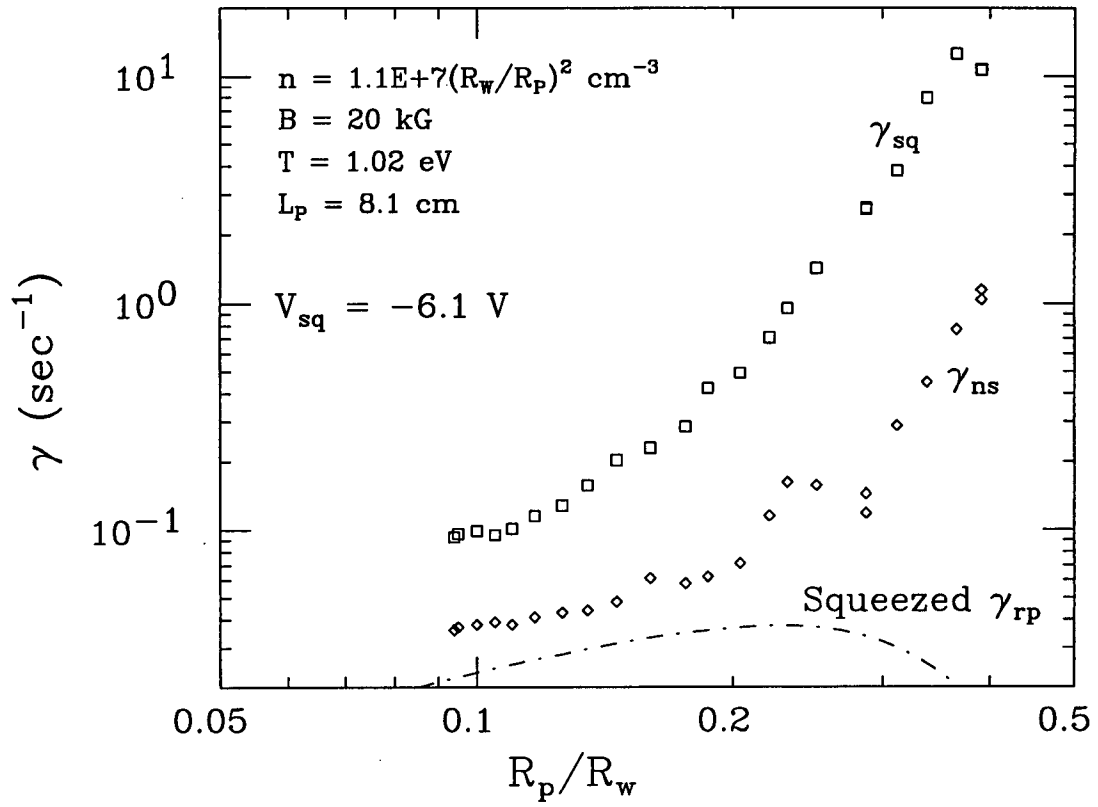


**Figure 5.5:** The squeeze damping rate increases strongly with $R_p$, as does $\gamma_{ns}$. The dot-dashed curve is the rotational pumping theory prediction for the squeezed plasma.

electrons, $N$, constant. Thus, as $R_p$ increases, the density decreases. [Here, $R_p$ is defined as the radius of a uniform density column required to give the measured $N$ using the density averaged over P1.]

As $R_p$ is increased in this manner, both $\gamma_{sq}$ and $\gamma_{ns}$ increase, as shown in Figure 5.5. A factor of 4 increase in the plasma radius causes $\gamma_{sq}$ to increase by nearly 2 orders of magnitude, which is even stronger than the dependence of $\gamma_{ns}$ on $R_p$ through rotational pumping. Presumably, $\gamma_{sq}$ increases strongly with $R_p$ because the radial electric fields created by the squeeze perturbation have a scale length of about a wall radius, $R_w$. Thus, the closer $R_p$ is to $R_w$, the more the plasma should be influenced by the squeeze perturbation. The strong increase in $\gamma_{sq}$ with $R_p$ also

indicates that $\gamma_{sq}$ probably decreases with density or is independent of density. The points in Figure 5.5 with the largest $R_p$ have the lowest density. Thus, if $\gamma_{sq}$ increased with density, this would tend to cancel the dependence on $R_p$.

The prediction of the theory for the data in Figure 5.5 is similar to those for Figures 5.2-5.4. The theory agrees with the measured damping rates without squeeze to within a factor of 2, but predicts that the squeeze perturbation should decrease the damping rate. Furthermore, the theory predicts that $\gamma_{sq}$ should decrease at the largest $R_p$, in contradiction with the measured increase.

### 5.3.5 Plasma Length

I have not thoroughly investigated the scaling of $\gamma_{sq}$ with the plasma length, $L_p$. I have, however, measured $\gamma_{sq}$ for a shorter plasma. Figure 5.6 shows the dependence of $\gamma_{sq}$ on $V_{sq}$ for a plasma confined in cylinders L3-L4, which was the typical confinement region for the experiments described in Chapter 4. The length of this confinement region is $L_c = 4.953$ cm; the squeeze voltage was applied to the L3 cylinder, which is $L_{sq} = 2.159$ cm long. Surprisingly, with this geometry, the squeeze perturbation *decreases* the damping rate of the $m = 1$ diocotron mode, which is the opposite of the increase observed for long plasmas. The space charge potential of this plasma was -65V, which is more negative than the applied $V_{sq}$.

In contrast with the predictions for long plasmas, Crooks and O'Neil's theory correctly predicts that squeeze reduces the $m = 1$ diocotron mode damping rate for a short plasma. The theory predicts that $\gamma_{sq}$ should be independent of $V_{sq}$ for $-V_{sq} < 3$ V, and that $\gamma_{sq}$ decreases strongly as $V_{sq}$ becomes more negative than -8 V, in agreement with the measurements. The theory also predicts the magnitude of the $\gamma_{sq}$ to within a factor of 2 for all but the strongest $V_{sq}$. The theoretical damping rate increases at the largest $-V_{sq}$ for the same reason it increases in Figure 5.3; the plasma is being excluded from the squeeze cylinder and its overall length is decreasing.

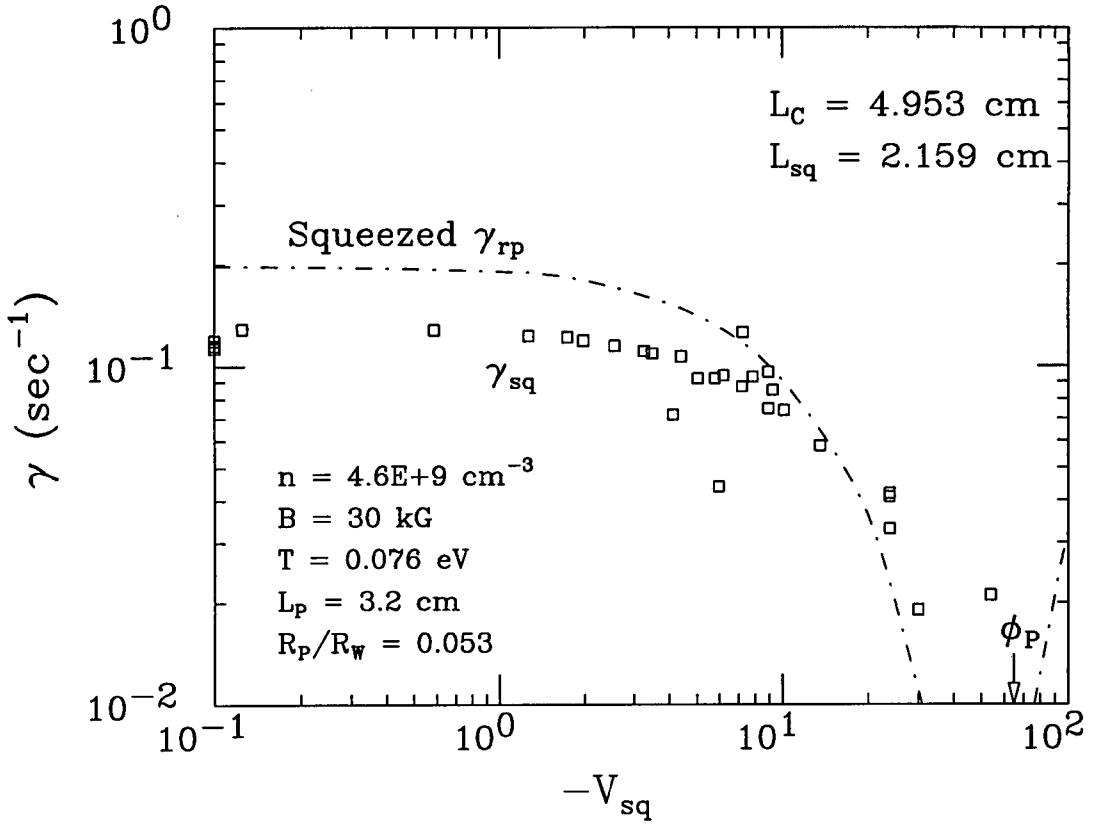


**Figure 5.6:** Squeeze reduces the damping rate of a short plasma, as predicted by rotational pumping theory. The arrow indicates the plasma potential, $\phi_p$, with no squeeze.

## 5.4 End Shape of Squeezed, Off-axis Plasmas

I have found from the solutions of the 3-D Poisson-Boltzmann code that the squeeze perturbation decreases the plasma-averaged $\delta L$, for both long and short plasmas. Here, as in Chapter 4, $\delta L$ is the amplitude of the azimuthal variation in the plasma length. Rotational pumping theory predicts that squeeze decreases the damping rate of the $m = 1$ diocotron mode because of this reduction in $\delta L$. To understand why this is so, one must consider the the vacuum potential created by a finite length cylinder when a voltage is applied to it. In Figure 5.1, the vacuum potential in the grounded cylinder due to the applied voltages $V_c$ and $V_{sq}$ is most

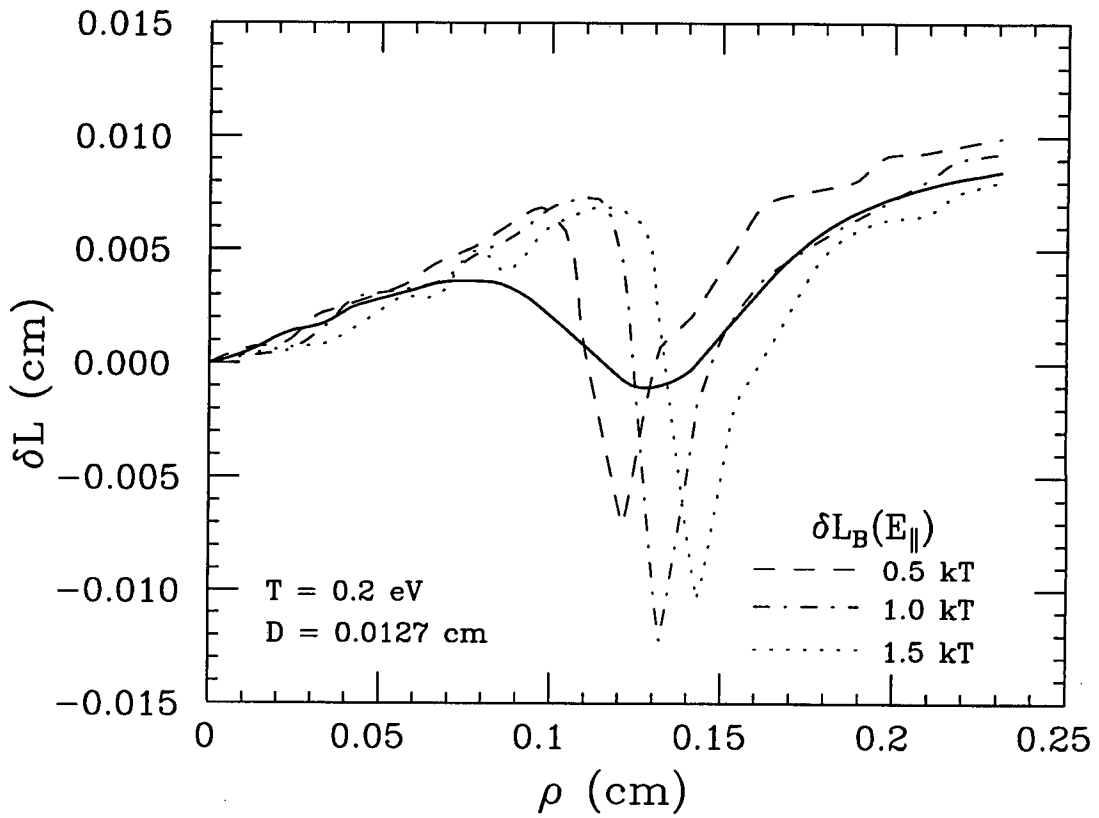


**Figure 5.7:** The squeeze perturbation cancels the curvature of the vacuum equipotentials, giving $\delta L \sim 0$ at $\rho = 0.13$ cm. However, the $\delta L_B$ of individual electrons are still large.

negative along the cylinder axis and goes to zero at the grounded wall. This difference in potential gives curvature to the vacuum equipotentials, resulting in a deformation of the plasma shape, $\delta L$, when the plasma is off axis. In the squeeze cylinder, however, the vacuum potential from the applied voltage $V_{sq}$ is *least* negative along the cylinder axis and goes to $V_{sq}$ at the wall. This counteracts the change in the confining potential due to the applied voltage $V_c$, giving less curvature to the vacuum equipotentials. The result is a smaller $\delta L$.

This competition between the squeeze voltage and the confinement voltages in shaping the plasma is demonstrated in Figure 5.7 and Figure 5.8. The radial profiles of the the length variation $\delta L(\rho)$ (Figure 5.7) and plasma length $L_0(\rho)$ (Figure 5.8)

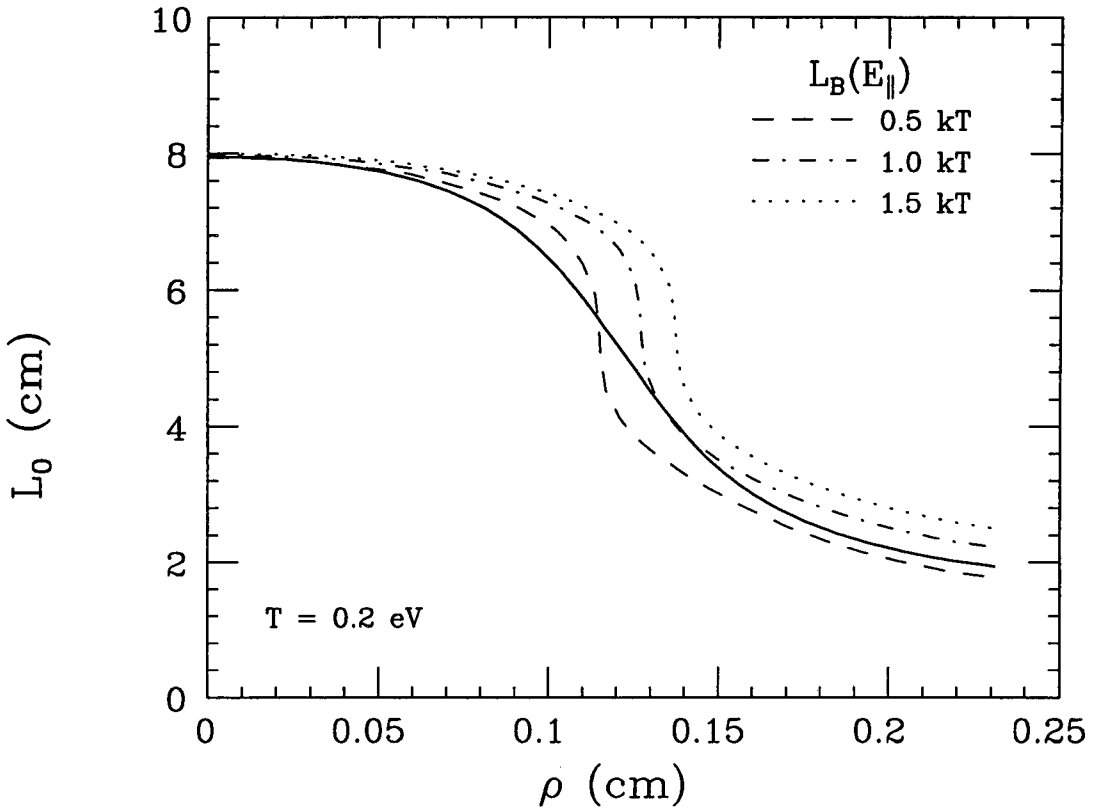


**Figure 5.8:** The squeeze perturbation causes a decrease in $L_0(\rho)$ around $\rho = 0.13$ cm, where $\delta L \sim 0$. However, the $L_B(\rho)$ of individual electrons depend on $E_\parallel$.

are shown for the same plasma as in Figure 5.4 at a temperature of 0.2 eV. The length and length variation are defined by Eqs. 4.17 and 4.18. In Figure 5.7, the length variation $\delta L$ is shown by the solid curve. Near the plasma axis, $\delta L$ increases linearly with $\rho$, just as if there were no squeeze perturbation. This is because the electrons move to shield out the squeeze voltage from the plasma center. At larger $\rho$, however, $\delta L$ decreases with $\rho$, actually becoming negative around $\rho = 0.125$ cm. Here, the the plasma is getting shorter, as shown by the solid curve of $L_0$ in Figure 5.8. Electrons at $\rho \sim 0.1$ cm do not penetrate as far towards the confinement rings as electrons on axis. Hence, they are affected more by the squeeze voltage than by the confinement voltage, which reduces $\delta L$. At the largest $\rho$, the length variation again increases with

$\rho$. At these radii, the plasma length is less than 1/2 its central value. Hence, electrons at $\rho > 0.13$ cm are entirely contained in the grounded cylinders, where the vacuum equipotentials from $V_c$ and $V_{sq}$ both have the same curvature. These electrons do not contribute much to the rotational pumping damping, however, because the density is so low at the plasma edge.

The decrease in the curvature of the vacuum equipotentials caused by applying a squeeze voltage decreases the vacuum radial electric fields. (Here, "radial" is referenced to the trap axis.) This presumably acts to decrease the confining field contribution to the $\mathbf{E} \times \mathbf{B}$ rotation frequency $\omega_R$. This, in turn, suggests a mechanism by which the squeeze perturbation might suppress the increase in $\gamma_{ns}$ with $T$ at high temperatures which is shown in Figure 5.4. The thermal spread in $\mathbf{E} \times \mathbf{B}$ drifts discussed in Section 4.7 comes about because higher energy electrons penetrate farther in to the confining potentials at the plasma ends. A decrease in the radial vacuum electric fields should then decrease this thermal spread, which in turn may decrease its contribution to the damping of the $m = 1$ diocotron mode.

## 5.5 Non-Maxwellian Distributions

I have found numerical and experimental evidence that the squeeze pertubation drives non-Maxwellian variations in the distribution of electron parallel energies, $E_{||}$. The Crooks and O'Neil theory includes only dissipation caused by the collisional equilibraton of $T_{||}$ and $T_{\perp}$, and thus ignores dissiaption caused by the relaxation of the $E_{||}$ and $E_{\perp}$ distributions separately. If the squeeze perturbation drives non-Maxwellian distributions, this may explain why the Crooks and O'Neil theory underestimates the transport rate.

The numerical evidence for non-Maxwellian distributions is shown in Figure 5.7. The dashed, dot-dashed, and dotted curves show the amplitude of the varia-

tion in the bounce lengths $\delta L_B(E_{||})$, for electrons with parallel energies of $E_{||} \doteq 0.5\ kT$, 1 $kT$, and 1.5 $kT$. ($T = 0.2$ eV in Figure 5.7.) Due to the finite Debye length, the cyclic variation in the turning points is not the same for electrons with different $E_{||}$. For example, at $\rho = 0.013$ cm, $\delta L_B$ for an electron with $E_{||} = 1\ kT$ is $-0.010$ cm, whereas $\delta L_B$ for an electron with $E_{||} = 1.5\ kT$ is $+0.004$ cm. This indicates that cyclic variation in the parallel energy of the electrons does not maintain a Maxwellian distribution of $E_{||}$. Conceivably, electron-electron collisions which attempt to relax the $E_{||}$ distribution may cause enough dissipation to cause squeeze damping of the $m = 1$ diocotron mode. This dissipation is ignored by the Crooks and O'Neil theory, since that theory only uses the solid curve in Figure 5.7, $\delta L$, which is the $E_{||}$-average of the $\delta L_B(E_{||})$.

Experimental evidence that the squeeze perturbation causes non-Maxwellian $E_{||}$ distributions is given by Figure 5.9, which shows that $\gamma_{sq}$ does not decrease when the electrons become strongly magnetized, i.e. when $r_c < b$. This plot again shows measured squeeze damping rates, $\gamma_{sq}$, and damping rates without squeeze, $\gamma_{ns}$, plotted against $R_p/R_w$. The data for $R_p/R_w < 0.2$ apparently contradicts the data in Figures 5.5 and 4.14 and the rotational pumping theory; $\gamma_{ns}$ decreases with $R_p$. The explanation of this contradiction is that the temperature was not held constant as this data was taken. The larger $R_p$ have lower densities and thus less Joule heating due to anomalous transport. Thus, cyclotron cooling decreased $T$ as $R_p$ increased. This means that the temperature in Figure 5.9 decreases from left to right. The magnetic field for this data set was $B = 40$ kG, and the temperature of the leftmost points was 0.05 eV, giving $r_c/b \approx 5$. Comparing to Figure 4.16 shows that $\gamma_{ns}$ should decrease as $T$ decreases. This decrease in $\gamma_{ns}$ with decreasing $T$ overwhelms the increase due to increasing $R_p$, giving the overall decrease with $R_p$ shown in Figure 5.9 for $R_p/R_w < 0.2$. The squeeze damping rate, however, does

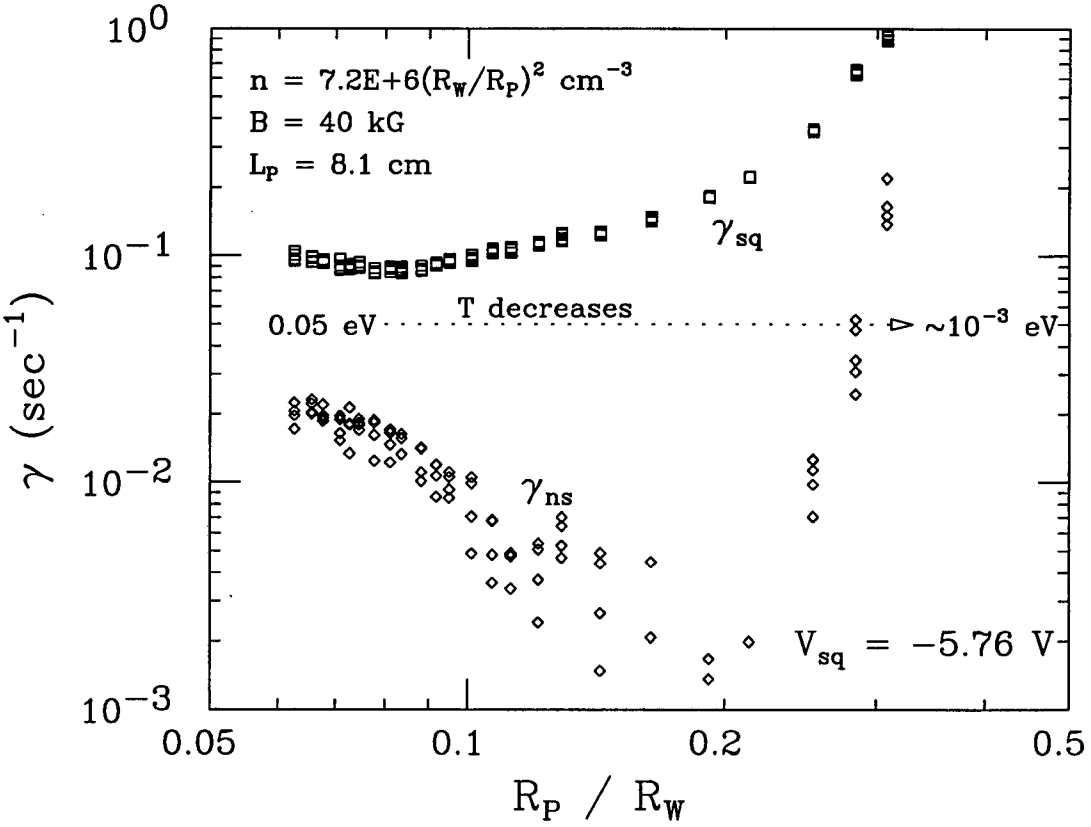


**Figure 5.9:** Squeeze damping is not inhibited by strong magnetization. As $R_p$ increases, $T$ decreases, which decreases $\gamma_{ns}$ because $r_c < b$. However, the squeeze damping rate, $\gamma_{sq}$, is not effected. The reason for the increase in $\gamma_{ns}$ at the largest $R_p$ is not known.

not decrease; the ratio $\gamma_{sq}/\gamma_{ns}$ goes from 5 to 100 as $R_p/R_w$ increases from 0.06 to 0.2. This indicates that $\gamma_{sq}$ is not affected by the reduction in the equilibration rate, $\nu_{\perp\|}$, in the strongly magnetized regime. Hence, the collisions must cause dissipation by some other means than equilibrating $T_\perp$ and $T_\|$. This can only occur if the $E_\|$ distribution is non-Maxwellian. Note that in the strongly magnetized regime, 3 body collisions, rather than binary collisions, are the primary $E_\|$ relaxation mechanism. Three body collisions are discussed in Section 4.6.2.

Conceivably, the lack of dependence of $\gamma_{sq}$ on $\nu_{\perp\|}$ could mean that squeeze damping does not depend on collisions. However, for the leftmost points in Fig-

ure 5.9, $\nu_{\perp\parallel} \approx 3.3 \times 10^5$ sec$^{-1}$ is over one-half the mean bounce frequency $\overline{f_B}$. This high collisionality argues against any non-collisional mechanisms such as resonant particles.

I do not know why $\gamma_{ns}$ increases at the largest $R_p$ in Figure 5.9. The very strong dependence on $R_p$ in this regime indicates that $R_p$ is breaking some threshhold. One explanation is that the edge of the density profile is reaching to the wall, which could cause an increase in the damping rate.

## 5.6 Comparison with Theory

The dot-dashed curves in Figures 5.2-5.6 show the predictions of the *adiabatic* rotational pumping theory. These predictions clearly do not agree with the data. Including the contributions of the resonant particle rotational pumping theory discussed in Section 4.6.1 does not improve the agreement. Most of the data presented here is for plasmas with rotation frequencies, $f_R = \omega_R/2\pi$, smaller than the electrons' mean bounce frequency $\overline{f_B}$, giving a negligible resonant particle contribution. Those plasmas where $f_R > \overline{f_B}$ are too collisional for resonant particles.

Fine compared his measurements to a theory of "beat-wave" damping by Crawford and O'Neil [6, 5]. From the perspective of this theory, the squeeze perturbation is an an azimuthally symmetric ($m = 0$), zero frequency wave in the $z$-direction. Its lowest wavenumber component is $k_z = \pi/L_p$. The diocotron mode is an $m = 1$, $k_z = 0$ wave traveling in $\theta$ at frequency $\omega_d$. The beating of these two waves makes an $m = 1$, $k_z = \pi/L_p$ wave with frequency $\omega_d$. Crawford and O'Neil then assume that the electrons travel in orbits unperturbed by this beat wave; i.e. they assume the plasma is on axis and that its shape is not affected by the squeeze perturbation. Certain electrons will then have orbits which are resonant with the beat wave. These electrons absorb energy from the beat wave through Landau damping,

which damps the $m = 1$ diocotron mode mode.

The beat-wave model probably oversimplifies squeeze damping. The assumption that the electrons travel along "unperturbed orbits" is not consistent with experimental results. My numerical calulations of the 3-D plasma density profile when a squeeze voltage is applied show that the squeeze potential is largely shielded out of the bulk of the plasma by large perturbations to the plasma shape, as shown by Figure 5.1 and Figure 5.8. This means that the squeeze region is inaccessible to electrons with low enough energy.

My results are do not disprove Crawford and O'Neil's theory, but do shed some doubt on it. Equation 6.3 in Fine's thesis states that the beat-wave damping theory predicts that $\gamma_{sq}$ scales as

$$\gamma_{sq} \propto \frac{V_{sq}^2}{B} \frac{f_R}{\overline{f_B}} \exp\left[-\frac{1}{2}\left(\frac{f_R}{\overline{f_B}}\right)^2\right], \tag{5.3}$$

where I have substituted $\pi/L_p$ for $k_z$. The scaling with $f_R$ disagrees with my data. In Figure 5.5, $f_R$ is smaller than $\overline{f_B}$ and decreases as $R_p$ increases. The theory predicts that $\gamma_{sq}$ should decrease, but instead it increases. Note also that some of my data is in a parameter regime that precludes resonant particles. As noted at the end of the previous section, the data in Figure 5.9 was taken on a highly collisional plasma. Hence any resonances would be washed out by collisions, and Crawford and O'Neil's theory should not apply.

# Appendix A

# Non-adiabatic Compressional Heating

In this Appendix, I present data on plasma heating caused by modulating the plasma length. The plasma length is modulated by applying azimuthally symmetric, oscillating voltages to the confinement cylinders. I find that the most efficient heating occurs when the frequency of the applied voltage $f_{mod}$ is near the mean bounce frequency $\overline{f_B}$, i.e. when the applied voltage oscillates non-adiabatically. For $f_{mod} \leq \overline{f_B}$, the heating rate strongly increases with $f_{mod}$ and strongly decreases with $\overline{f_B}$. The scalings of the heating rate with $f_{mod}$ and $\overline{f_B}$ show some agreement with a heating rate derived from the Crooks and O'Neil resonant particle rotational pumping theory [7]. This agreement implies that resonant particles may enhance rotational pumping transport in plasmas that are not too collisional.

In taking the data in this Appendix, the plasma was confined as shown in Figure 2.2. The length of the confinement region is $L_c = 4.953$ cm, and the confinement voltage was $V_c = -100$ V. The unperturbed plasma length was $L_p = 3.73$ cm. This length was modulated by applying a sinusoidally varying voltage to the 1.4 cm L4 cylinder. The plasma density was $n = 2.7 \times 10^9$ cm$^{-3}$, the plasma radius was $R_p/R_w = 0.06$, and the magnetic field was $B = 20$ kG. The background Joule heating rate for these plasma parameters was negligible compared to the heating rate

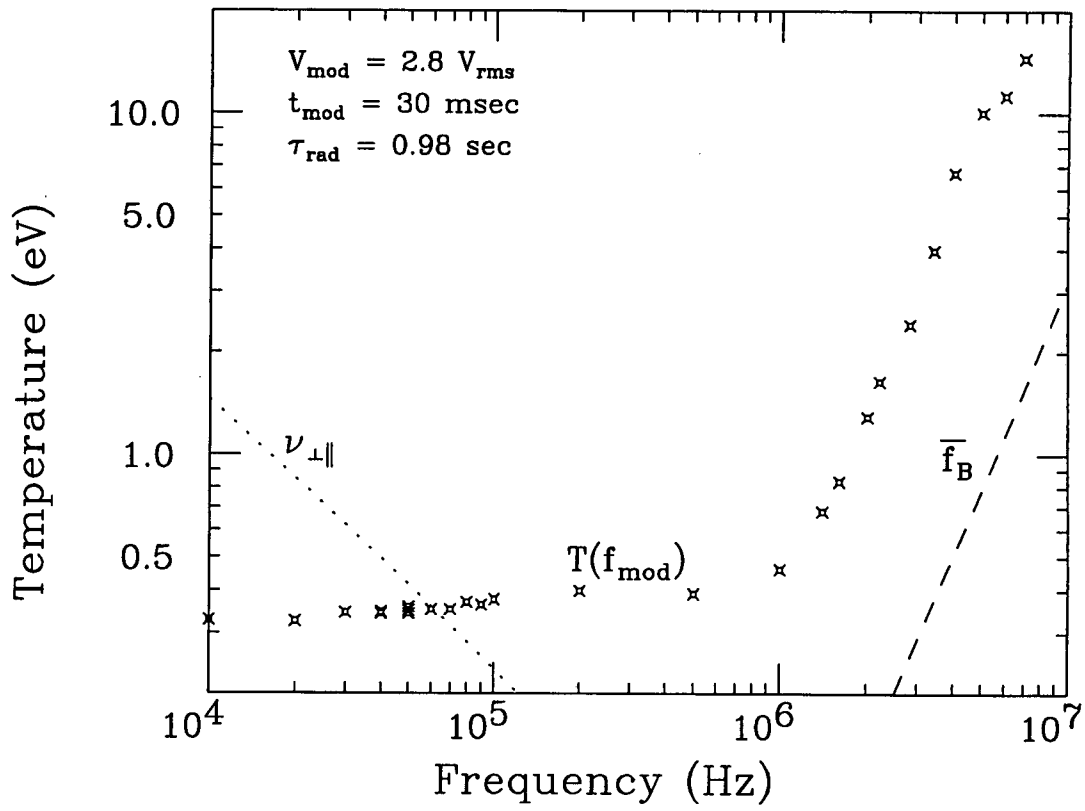


**Figure A.1:** Final temperature after 30 msec of modulating the plasma length plotted against modulation frequency. The intial temperature was 0.32 eV. The dotted line shows $\nu_{\perp\parallel}$ and the dashed line shows $\overline{f_B}$. The small increase in temperature when $f_{mod}$ becomes larger than $\nu_{\perp\parallel}$ is due to adiabatic, collisional heating. Non-adiabatic heating ($f_{mod} \sim \overline{f_B}$) is much more effective.

from the applied voltage. Similarly, cyclotron radiation was negligible in these experiments, as the radiation time, $\tau_{rad} = 1$ sec, was much longer than the measurement times.

Figure A.1 shows the plasma temperature, $T$, after modulating the plasma length for 30 msec, plotted against the modulation frequency, $f_{mod}$. The dotted line shows the collisional equilibration rate $\nu_{\perp\parallel}$ as a function of temperature, and the dashed line shows $\overline{f_B}$. (For the dashed and dotted lines, temperature is the *dependent* variable and frequency is the *independent* variable.) The measured temperature in-

creases slightly with the modulation frequency for $f_{mod} = 10$ kHz to $f_{mod} = 200$ kHz, and is independent of of the modulation frequency for 200 kHz $< f_{mod} <$ 500 kHz. This is consistent with Beck's [2, 1] measurements of plasma heating caused by adiabatically modulating the plasma length. Here, "adiabatic" means that the modulation frequency is small compared to the thermal electron bounce frequency, $\overline{f_B}$. The modulation in $L_p$ causes a modulation in the parallel temperature, $T_{||}$; collisions tend to equilibrate $T_\perp$ with $T_{||}$, causing an irreversible increase in both. Beck showed that the heating rate is given by

$$\frac{dT}{dt} = \frac{4}{3}\nu_{\perp||} T \left(\frac{\delta L}{L_p}\right)^2 \frac{\beta^2}{1+\beta^2}, \tag{A.1}$$

where $\beta = 2\pi f_{mod}/3\nu_{\perp||}$ and $\delta L$ is the amplitude of the length variation. When $f_{mod} \gg \nu_{\perp||}$, the fraction on the right equals 1 and the heating rate is independent of $f_{mod}$. This collisional equlibration between $T_\perp$ and $T_{||}$ is the same mechanism which causes the dissipation in rotational pumping.

The plasma heats much faster when the plasma length is modulated non-adiabatically, as shown on the right hand side of Figure A.1. As $f_{mod}$ is increased towards $\overline{f_B}$, the measured temperature rapidly increases with $f_{mod}$. At $f_{mod} = 7$ MHz, the increase in temperature is 250 times the adiabatic increase. I used this highly efficient heating method to balance cyclotron cooling in many of the experiments described in this thesis.

Note that while rotation of an off-axis plasma modulates the plasma length, causing rotational pumping heating and transport, modulating the plasma length with oscillating applied voltages does not cause transport, even if the plasma is off-axis. This is because the applied voltages are not in phase with the plasma rotation. Consequently, any effect produced by the applied voltages is quickly phased mixed by the plasma rotation, so that the heating by the applied voltages is azimuthally symmetric around the plasma axis.

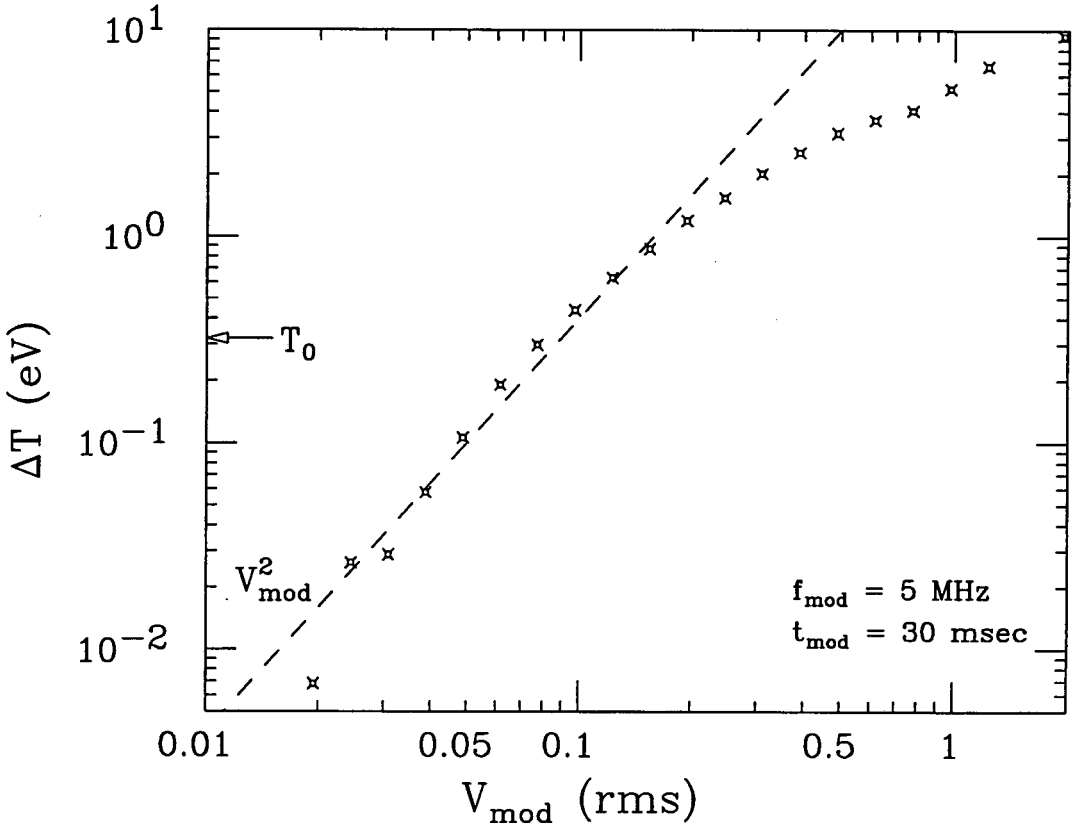


**Figure A.2:** Increase in temperature after 30 msec of modulating the plasma length plotted against the modulation voltage. The change in temperature scales as $V_{mod}^2$ for small $V_{mod}$. When the increase in temperature makes $\overline{f_B}$ larger than $f_{mod}$, the dependence on $V_{mod}$ decreases.

The dependence of the temperature increase on the amplitude of the modulation voltage is shown in Figure A.2. The modulation voltage was applied for 30 msec at frequency $f_{mod} = 5$ MHz. At small amplitudes, the change in temperature is proportional to $V_{mod}^2$. This scaling indicates that the non-adiabatic heating presented here is *not* a form of "cascade heating" [38]. Cascade heating occurs when a pure electron plasma is allowed to freely expand along the magnetic field. The unbalanced space charge electric fields accelerate the electrons at the end of the plasma as the plasma expands. The plasma temperature increases when these electrons collisionally equilibrate with the rest of the plasma. The increase in thermal energy is equal

to the decrease in electrostatic energy, and so is first order in $V_{mod} \propto \delta L$, which is not consistent with the $V_{mod}^2$ scaling seen here. Furthermore, the variation in the plasma length in these experiments is too small to allow the plasma to freely expand. That is, $\bar{v}/\delta L \gg f_{mod}$, so that space charge electric field at the end of the plasma is always balanced by the confining fields.

The arrow in Figure A.2 indicates the point at which the temperature increase is as large as the original temperature. As the plasma is heated further, the increase in temperature depends less strongly on $V_{mod}$, indicating that the applied voltage is heating the plasma less efficiently. Comparing the temperature increase in Figure A.1 to that in Figure A.2 indicates that a smaller $V_{mod}$ should be used in order to obtain the dependence of the heating on $f_{mod}$. Figure A.3 shows the result of using a smaller $V_{mod}$. This data was taken the same way as that in Figure A.1 except that the 2 symbols in Figure A.3 correspond to $V_{mod} = 0.14$ and 0.049 $V_{rms}$. Using these smaller voltages, and increasing $f_{mod}$ all the way to 50 MHz reveals a peak in the measured temperature. This suggests that $f_{mod}$ is resonant with some motion of the electrons. The width of the peak and its location indicate that the heating is not due to the excitation of a plasma mode; these modes are observed to have narrow resonances and mode frequencies of at least 10 MHz for these plasma parameters. Rather, $f_{mod}$ is probably resonant with the electron's bounce motion, as indicated by the dashed line. The width of the peak is consistent with the thermal spread in electron bounce frequencies.

The peak in Figure A.3 suggest a resonance between $f_{mod}$ and the bounce motion of the electrons. However, there are two problems with this data. First, it does not give the dependence of the heating rate on $\overline{f_B}/f_{mod}$. This is because the temperature of the plasma changes over the 30 msec measurement period, which changes $\overline{f_B}$. Also, the coaxial cables which carry the modulation voltage are termi-

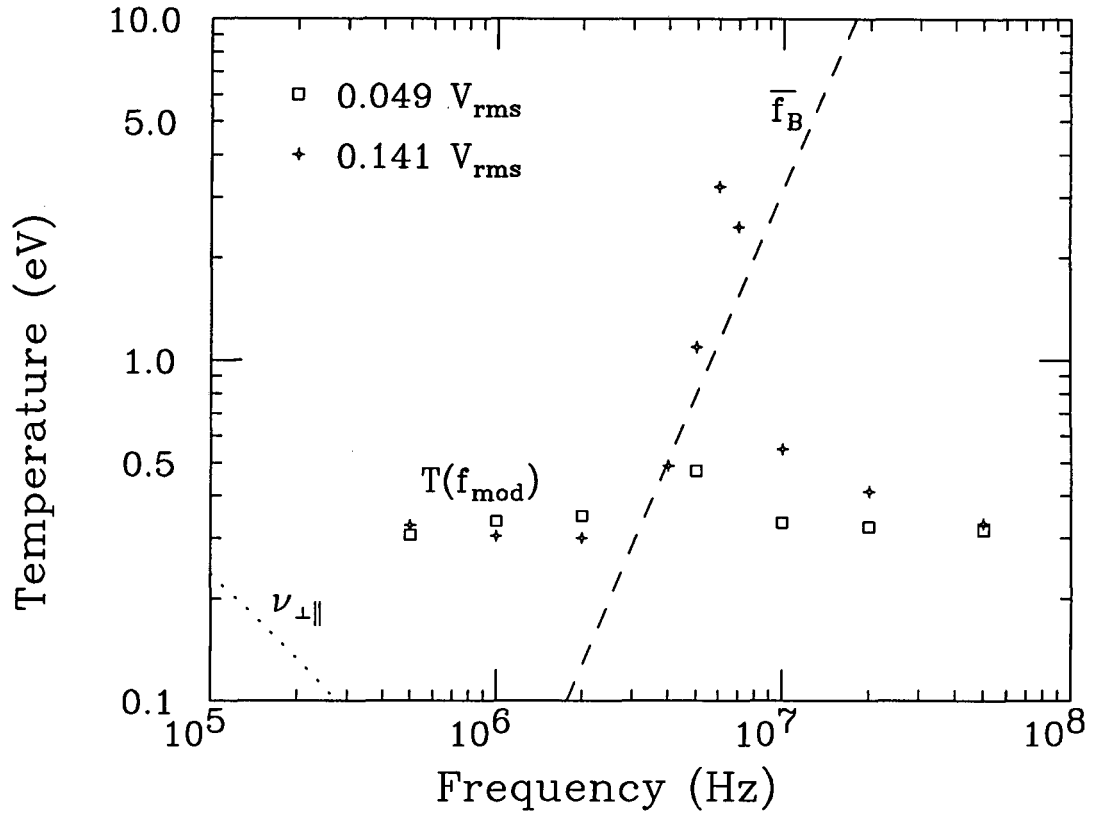


**Figure A.3:** Final temperature after 30 msec of heating plotted against the modulation frequency. Heating peaks where $f_{mod} \sim \overline{f_B}$. These data sets each had a smaller $V_{mod}$ than the data in Figure A.1.

nated only with the capacative load of the confinement cylinders. Consequently, at frequencies above about 5 MHz, the voltages on the cylinders are frequency dependent and may have been different than the voltages measured outside the cryostat. Experimental testing and theoretical calculation show that for $f_{mod} \leq 10$ MHz, this difference is at most a 25% attenuation of $V_{mod}$. However, at higher frequencies the transmitted $V_{mod}$ exhibits large variations with $f_{mod}$.

The solution to these problems is to measure the instantaneous heating rate as a function of $\overline{f_B}$ at a fixed $f_{mod}$. To do this, I measured $T$ as a function of time at 4 different frequencies, as shown in Figure A.4. The 4 symbols correspond to $f_{mod}$ = 2, 3, 4, and 10 MHz; the modulation voltage amplitude was $V_{mod}$ = 0.566 $V_{rms}$.

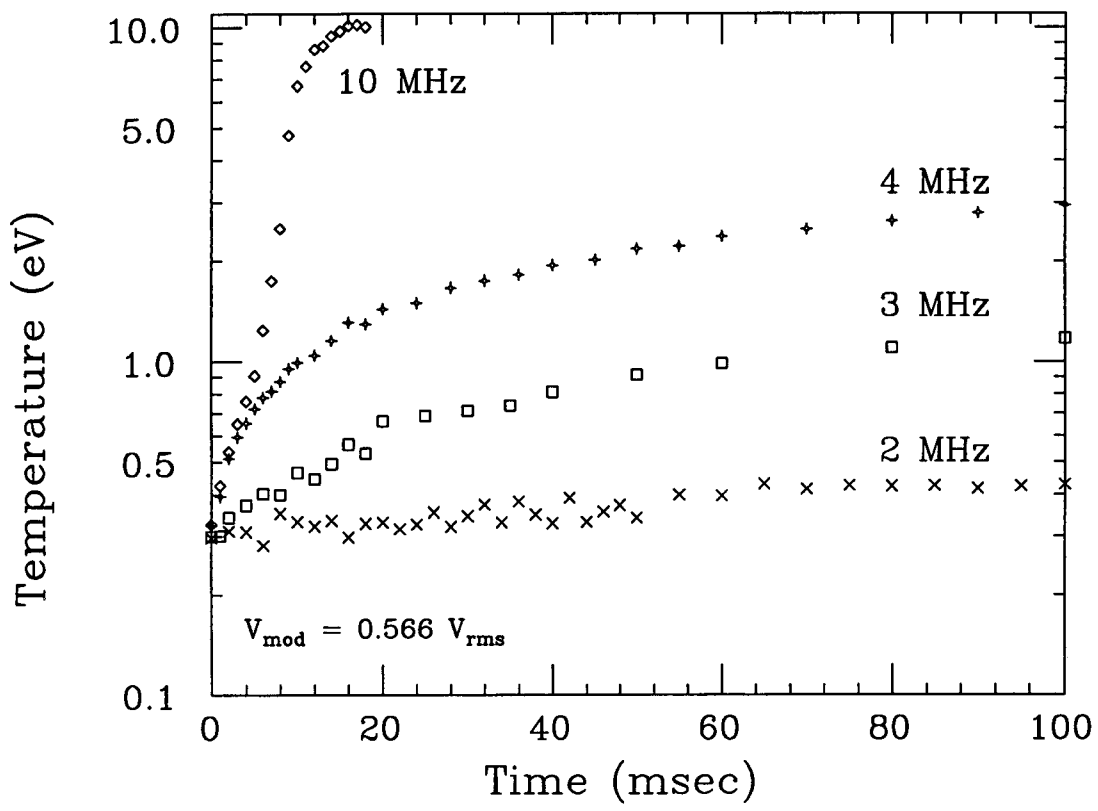


**Figure A.4:** Evolution of temperature at $f_{mod}$ = 2, 3, 4, and 10 MHz.

I fit this data with slightly smoothed cubic splines and evaluated $dT/dt$ at each data point. The 2 MHz data is too noisy to get a smooth spline fit, so I calculated $dT/dt$ at 4 different points by hand. The measured heating rates are plotted against the scaled thermal bounce frequency, $\overline{f_B}/f_{mod}$, in Figure A.5. At each frequency, the heating rate decreases strongly with $\overline{f_B}$ when the bounce frequency is larger than the modulation frequency. Furthermore, at modulation frequencies of 4 and 10 MHz, the maximum $dT/dt$ is at $\overline{f_B} \approx f_{mod}$. The heating rate also appears to increase strongly with $f_{mod}$ at fixed $\overline{f_B}/f_{mod}$. This effect is too strong to be explained by the frequency dependence of transmission of the applied voltage through the coaxial cables.

The 4 theory curves in Figure A.5 show heating rates derived from Crooks and O'Neil's resonant particle rotational pumping theory for the 4 experimental

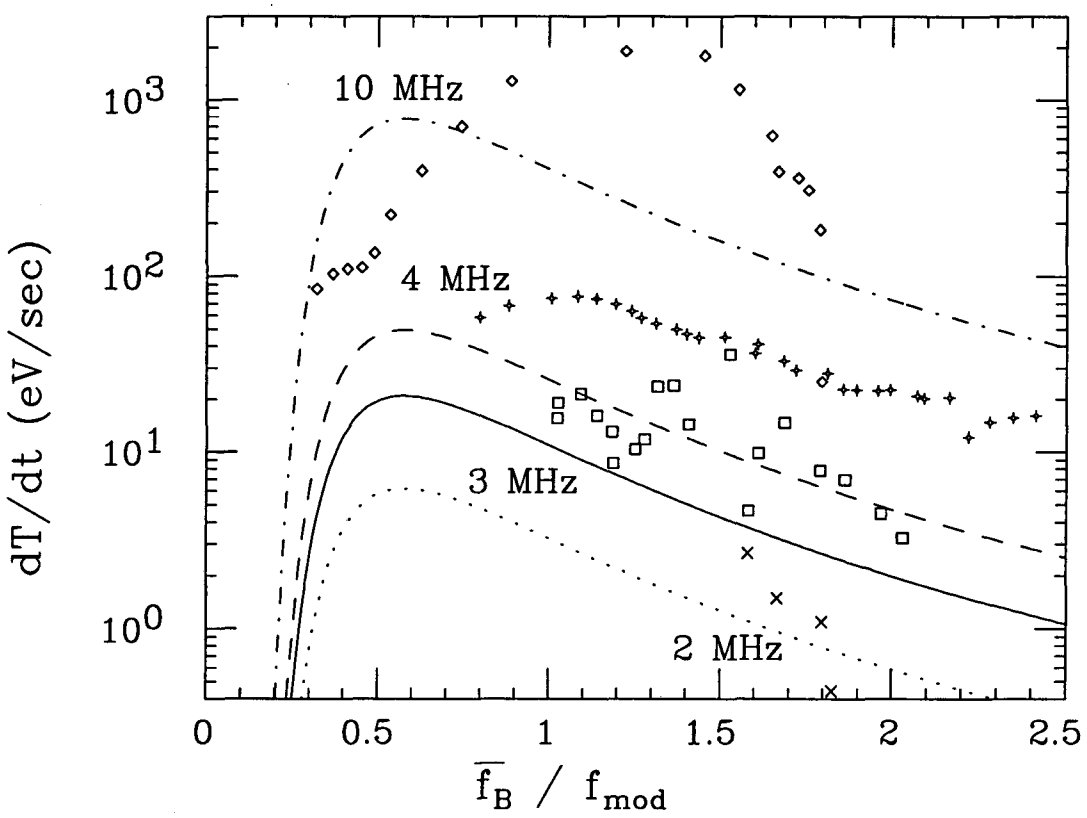


**Figure A.5:** Heating rate as a function of $\overline{f_B}/f_{mod}$ for $f_{mod}$ = 2, 3, 4, and 10 MHz. The heating rates peak at $f_{mod} \approx \overline{f_B}$, and then decrease strongly with $f_{mod}/\overline{f_B}$. The heating rate also increases strongly with $f_{mod}$ at a given $f_{mod}/\overline{f_B}$. The curves show the predictions of resonant particle theory. The dotted, solid, dashed, and dot-dashed curves correspond to 2, 3, 4, and 10 MHz, respectively.

$f_{mod}$. Here, the plasma length is modulated by the applied voltages, rather than the rotation of the plasma through asymmetric potentials. Using Equation 4.23, this theory predicts

$$\frac{dT}{dt} = \frac{\sqrt{128\pi^3}}{3} m_e f_{mod}^3 (\delta L)^2 \left(\frac{f_{mod}}{\overline{f_B}}\right)^3 \exp\left[-\frac{1}{2}\left(\frac{f_{mod}}{\overline{f_B}}\right)^2\right], \qquad \text{(A.2)}$$

where $m_e$ is the electron mass. The amplitude of the plasma length modulation was estimated, using $\delta L \propto V_{mod}$ and the data in Figure A.1, to be $\delta L/L_p = 0.002$. The scalings of the predicted heating rate with $\overline{f_B}$ and $f_{mod}$ both show some agreement with with the 2, 3, and 4 MHz data for $\overline{f_B} \geq f_{mod}$. The magnitude of the measured

rates are 2 to 5 times the predicted rates, but this could easily be a systematic error in the calculation of $\delta L$. However, the theory predicts that the maximum heating rate is for $f_{mod} \approx 2\overline{f_B}$, in contrast with the peak in the data at $f_{mod} \approx \overline{f_B}$. Nor is the dependence of the 10 MHz data on $\overline{f_B}$ well predicted by the theory. Thus, this data is inconclusive is confirming the Crooks and O'Neil resonant particle heating theory.

Note that in deriving Equation A.2, I divided $\overline{\omega_B} = 2\pi\overline{f_B}$ by 2 in Equation 4.23. In the resonant particle rotational pumping theory, the lowest order resonance is $\omega_R = 2\omega_B$ because the asymmetric potentials are at both ends of the plasma, which doubles the effective bounce frequency. Here, the modulation voltage is applied at only one end, so the resonance condition is $f_{mod} = f_B$.

As noted in Section 4.6.1, I do not observe any resonant particle enhancement of rotational pumping transport. This is probably because CV plasmas are too collisional, when $f_R \sim \overline{f_B}$. In this regime, the collision rate is the same order of magnitude as the bounce frequency, and any bounce-rotation resonances are destroyed by collisions. The data in Figure A.5, however, suggests that resonant particle rotational pumping may be important in plasmas where the collision rate is small when $f_R \sim \overline{f_B}$. The mechanism which causes the adiabatic heating shown in Figure A.1 is the same as that which causes dissipation in adiabatic rotational pumping. Thus, the mechanism which causes the much faster non-adiabatic heating may cause much faster dissipation and hence much faster rotational pumping transport.

# Appendix B

# End Shapes of Off-Axis Plasma Columns

## B.1 Overview

In this Appendix, I present analytical and numerical calculations of the end shapes of plasma columns which have been displaced from the trap axis. As shown in Figure 4.1, the length of a displaced plasma column is not azimuthally symmetric around the plasma axis. Here, as in Chapters 4 and 5, I define $\delta L(\rho)$ as the amplitude of the azimuthal length variation at a distance $\rho$ from the plasma axis. I find that $\delta L$ is well-approximated by an analytical estimate for wide and/or hot plasmas. However, perturbation of the space charge fields increases $\delta L$ in cold, narrow plasmas. The end shapes of these plasmas must be calculated numerically.

In Section B.2, I estimate $\delta L(\rho)$ for a uniform density, "well-confined" plasma. By well-confined, I mean that the magnitude of the space-charge potential of the plasma, $\phi_p$, is small compared to the confining potential $V_c$. The calculation of $\delta L$ gives the length variation due to the curvature of the confining and image charge potentials, but neglects changes in the space charge fields caused by the change in the plasma end shape. The estimated $\delta L$ is proportional to both $\rho$ and the displacement $D$.

In section B.3, I compare this estimate to numerical calculations of $\delta L$ for

well-confined, uniform density plasmas. I find that while the estimate is a good approximation to $\delta L$ for wide and/or hot plasmas, it underestimates $\delta L$ for cold, narrow plasmas. In these plasmas, the change in the plasma end shape creates space charge fields which further increase $\delta L$.

In section B.4, I present numerical calculations of $\delta L$ for 2 experimental plasmas. I find smaller $\delta L$ for these plasmas than for the simulated plasmas because the experimental plasmas are not as "well-confined." Weakening the confinment, by increasing the temperature or decreasing $V_c$, further decreases $\delta L$. Finally, I show that $\delta L$ for ill-confined plasmas can depend nonlinearly on $\rho$.

## B.2 Estimate of $\delta L$

The zero order contribution to $\delta L$ comes from the curvature of the vacuum equipotentials. If a plasma is confined entirely in the grounded cylinders, the confining force on the plasma is weakest at the walls and strongest on the trap axis. Hence, a plasma which is displaced from the trap axis is longer near the wall than near the axis. An estimate of this length difference can be derived by assuming that the plasma has zero temperature and that a tube of plasma always terminates on the same confining equipotential as it $\mathbf{E} \times \mathbf{B}$ drifts around the plasma axis.

Consider 2 half-infinite cylinders, one grounded and one held at voltage $V_c$, as shown in Figure 4.1. Defining $z = 0$ as the boundary between the 2 cylinders, the vacuum potential in the grounded cylinder from $V_c$ can be written as

$$V(r,z) = V_c \sum_{i=1}^{\infty} \frac{\exp(-j_{0i} z/R_w)\, J_0(j_{0i} r/R_w)}{j_{0i}\, J_1(j_{0i})} \tag{B.1}$$

where $J_0$ and $J_1$ are Bessel functions of the first kind, and $j_{0i}$ is the $i$th zero of $J_0$.

Now consider a half-infinite plasma confined in the grounded cylinder. I define a "well-confined" plasma as one whose end is so far from the negatively biased cylinder that the confining potential in the plasma is well described by the first term

in the summation in Equation B.1, i.e.

$$V(r,z) \approx V_c \frac{\exp(-j_{01}z/R_w)\, J_0(j_{01}r/R_w)}{j_{01}\, J_1(j_{01})}. \tag{B.2}$$

In this case, the confining equipotentials are described by the equation

$$z_{eq}(r) = \frac{R_w}{j_{01}} \ln[J_0(j_{01}r/R_w)] + \text{constant} \tag{B.3}$$

Assuming $r \ll R_w$, I can approximate $\ln[J_0(j_{01}r/R_w)]$ by $-(j_{01}r/2R_w)^2$. The amplitude of the azimuthal variation in the length of a tube of plasma which terminates on the equipotential is then given by gives

$$\delta L(\rho) \equiv \frac{1}{2}\left[ z_{eq}(D-\rho) - z_{eq}(D+\rho) \right] = \frac{j_{01}}{2} \frac{D}{R_w} \rho, \tag{B.4}$$

where $D$ is the plasma displacement and $\rho$ is the distance from the plasma axis. Note that for a finite length plasma, $\delta L$ should be doubled because the plasma has 2 ends.

This estimate of $\delta L$ neglects the image charge potential and plasma temperature. A slightly more complicated model takes these effects into account. This model assumes that the the plasma space charge potential $\phi_p$ and the image charge potential $\phi_i$ at the end of the plasma are proportional to their value at the plasma center, where the proportionality factor, $F$, is a funtion of $D$ and $\rho$ only. Thus, conservation of energy defines the turning point of a thermal electron, $z_{TP}(r,\theta)$, by

$$\begin{aligned} &\frac{1}{2}kT(r,\theta) - e[\phi_p(r,\theta,\infty) + \phi_i(r,\theta,\infty)] = \\ &\quad -eF(\rho,D)[\phi_p(r,\theta,\infty) + \phi_i(r,\theta,\infty)] - eV(r,z_{TP}) \end{aligned} \tag{B.5}$$

where the left-hand side is the energy of a thermal electron at $z = \infty$ and the right-hand side is the energy of the electron at its turning point. The vacuum potential $V$ is defined by Equation B.2. The plasma potential at $z = \infty$ of a uniform density plasma column displaced from the trap axis is given by

$$\phi_p(r,\theta) = \phi_p(\rho) = -N_L e \left( 2 \ln \frac{R_w}{R_p} + 1 - \frac{\rho^2}{R_p^2} \right), \tag{B.6}$$

where $N_L$ is the number of electrons per unit length, and $R_p$ is the plasma radius. Similarly, the image charge potential is

$$\phi_i(r,\theta) = N_L e \ln\left(\frac{R_w^2}{R_w^2 + r^2(D/R_w)^2 - 2Dr\sin\theta}\right). \tag{B.7}$$

Combining Equations B.5-B.7 and solving for $z_{TP}$ gives

$$z_{TP}(r,\theta) = -\frac{R_w}{j_{01}} \ln\left[j_{01}J_1(j_{01})\frac{kT/2 - e(1-F)(\phi_p+\phi_i)}{-eV_c\, J_0(j_{01}r/R_w)}\right]. \tag{B.8}$$

Defining the length variation by

$$\delta L(\rho) = \frac{1}{2}\left[z_{TP}(D-\rho,\pi/2) - z_{TP}(D+\rho,\pi/2)\right], \tag{B.9}$$

gives

$$\delta L(\rho) = \frac{R_w}{2j_{01}} \times \ln\left\{\frac{kT/2 - e(1-F)[\phi_p(\rho) + \phi_i(D+\rho,\pi/2)]}{kT/2 - e(1-F)[\phi_p(\rho) + \phi_i(D-\rho,\pi/2)]}\frac{J_0(j_{01}(D-\rho)/R_w)}{J_0(j_{01}(D+\rho)/R_w)}\right\}. \tag{B.10}$$

Assuming that $D \ll R_w$ and $\rho \ll R_w$, the image charge potential can be approximated by

$$\phi_i(D \pm \rho, \pi/2) \approx 2N_L e \frac{D}{R_w}\,\frac{D \pm \rho}{R_w}, \tag{B.11}$$

and the Bessel functions can be approximated by

$$J_0(\, j_{01}(D \pm \rho)/R_w\,) \approx 1 - \left(\frac{j_{01}}{2}\frac{D \pm \rho}{R_w}\right)^2. \tag{B.12}$$

Combining these equations and using the approximation $\ln(1+x) \approx x$, gives, to first order in $D$ and $\rho$,

$$\delta L(\rho) = \left(\frac{j_{01}}{2} - \frac{2/j_{01}}{1 - 2\ln(R_w/R_p) + [2{\lambda_D}^2/R_p^2]/[1 - F(\rho,D)]}\right)\frac{D}{R_w}\rho, \tag{B.13}$$

where $2{\lambda_D}^2/R_p^2 = kT/2N_Le^2$. The first term in this equation is the same as Equation B.4. The decrease in $\delta L$ from the second term comes from the image charge

potential, which tends to cancel out the plasma potential most strongly near the wall.

This derivation of $\delta L$ is similar to a derivation by Peurrung and Fajans [50], except that they assume the plasma is zero temperature and that the end of the plasma is flat. Peurrung and Fajans defined an end "slant coefficient" as $C_s = \delta L/(D/R_w)/\rho$. For a zero temperature plasma, Equation B.13 gives the same slant coefficient as Peurrung and Fajans', without the flat end assumption. However, for the finite temperature plasmas discussed in the next section, I must assume the end is flat in order to use $F(\rho, D) = 1/2$ in Equation B.13.

## B.3 Numerical Calculations of $\delta L$ for Well-Confined Plasmas

As noted in Section 4.5.2, the value of $\delta L(\rho)$ obtained from Equation B.13 does not always agree with the $\delta L$ calculated from the 3-D Poisson-Boltzmann code. This discrepancy occurs partly because experimental plasmas are not always "well-confined", and partly because the model in Section B.2 does not take into account changes in the plasma space-charge potential when a plasma is displaced from the trap axis. In this section, I present numerical calculations of $\delta L$ for simulated, well-confined plasmas.

All of the simulated plasmas have uniform temperatures and $z$-integrated density profiles, i.e. $T$ and $n_z(\rho)$ are constant out to the plasma radius $R_p$. The plasmas are also "ideally well-confined." This was accomplished by leaving the confining potentials out of the solution to Poisson's equation. The plasma and image charge potentials were numerically calculated assuming the given electron distribution was in an infinite length, grounded cylinder. A confining potential of the form

$$V(r,z) = V_c\, J_0(j_{01} r/R_w) \left\{ \exp\left[ -j_{01} \frac{z + L_c/2}{R_w} \right] + \exp\left[ j_{01} \frac{z - L_c/2}{R_w} \right] \right\}, \qquad \text{(B.14)}$$

was then added to the calculated potential in order to calculate a new electron Boltzmann distribution along each magnetic field line. (Here, as in the remainder of this Appendix, $z = 0$ is at the center of the plasma and $L_c$ is the length of the "confinement region.") This is the form of the confining potential seen by a plasma which is far from the 2 confining cylinders, i.e. only the first term in Equation B.1 contributes to Equation B.14. The Poisson and Boltzman equations were iteratively solved in this manner to obtain a self-consistent equilibrium, $n(x, y, z)$ and $\phi(x, y, z)$.

The plasma length along each field line, $L$, and the length variation, $\delta L$, were then defined as in Equations 4.16 and 4.17, i.e.

$$L(x, y) = n_z(x, y)/n(x, y, z = 0), \tag{B.15}$$

$$\delta L(\rho) = \frac{1}{2}[L(\rho + D, 0) - L(\rho - D, 0)]. \tag{B.16}$$

I then defined the slant coefficient as

$$C_s \equiv \frac{R_w}{D} \left.\frac{d}{d\rho}\delta L(\rho)\right|_{\rho=0}. \tag{B.17}$$

Thus, $C_s$ is the normalized slope of $\delta L$ at $\rho = 0$. For $\delta L \propto \rho$, this definition of the slant coefficient is the same as Peurrung and Fajans'.

To numerically calculate the dependence of $C_s$ on the plasma parameters, I kept the plasma density and length constant by adjusting $V_c$. Unless otherwise noted, all plasmas simulated for the data in this section have $z$-integrated density $n_z/L_c = 10^7$ cm$^{-3}$, density $n \approx 1.3 \times 10^7$ cm$^{-3}$ and length $L_p/R_w \approx 7$. Except for Figure B.1, all of the plasmas have $D/R_w = 0.1$ or $D/R_w = 0.125$. The dependence of the numerically calculated $C_s$ on plasma temperature, radius, and displacement is discussed below. Note that changing the plasma temperature is equivalent to changing the density. That is, if I multiply $T$ by 2, the Poisson and Boltzmann equations give the same equilibrium electron distribution as if I had divided $n_z$ and $V_c$ by 2.

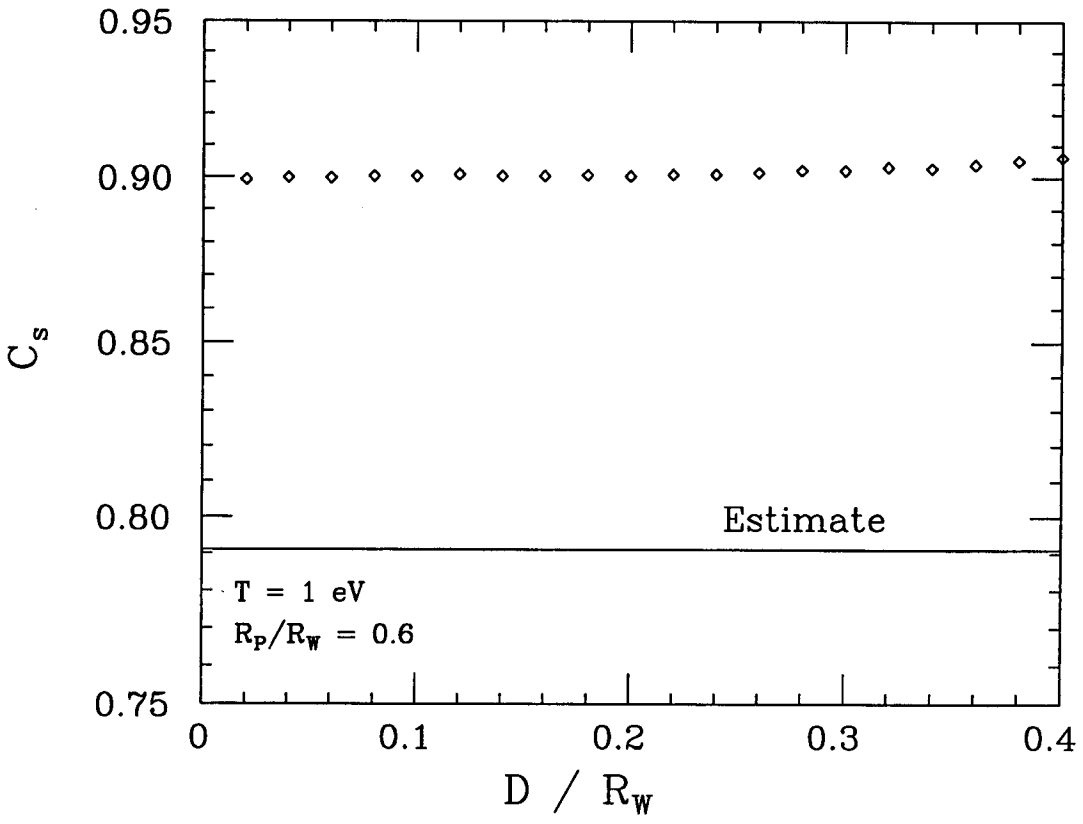


**Figure B.1:** The slant coefficient is independent of the plasma displacement. The solid line shows the estimate from Equation B.13.

### B.3.1 Displacement

The slant coefficient is independent of the displacement of the plasma column, as shown by Figure B.1. This plasma had radius $R_p/R_w = 0.6$ and a temperature $T = 1$ eV. As $D/R_w$ increases from 0.02 to 0.4, the slant coefficient $C_s$ increases less than 1%. The solid line in Figure B.1 shows the prediction of the Equation B.13, which is about 15% smaller than the numerical value.

### B.3.2 Temperature

The slant coefficient for this plasma is also nearly independent of temperature, as shown in Figure B.2. As $T$ increases by a factor of 40, $C_s$ for $R_p/R_w = 0.6$

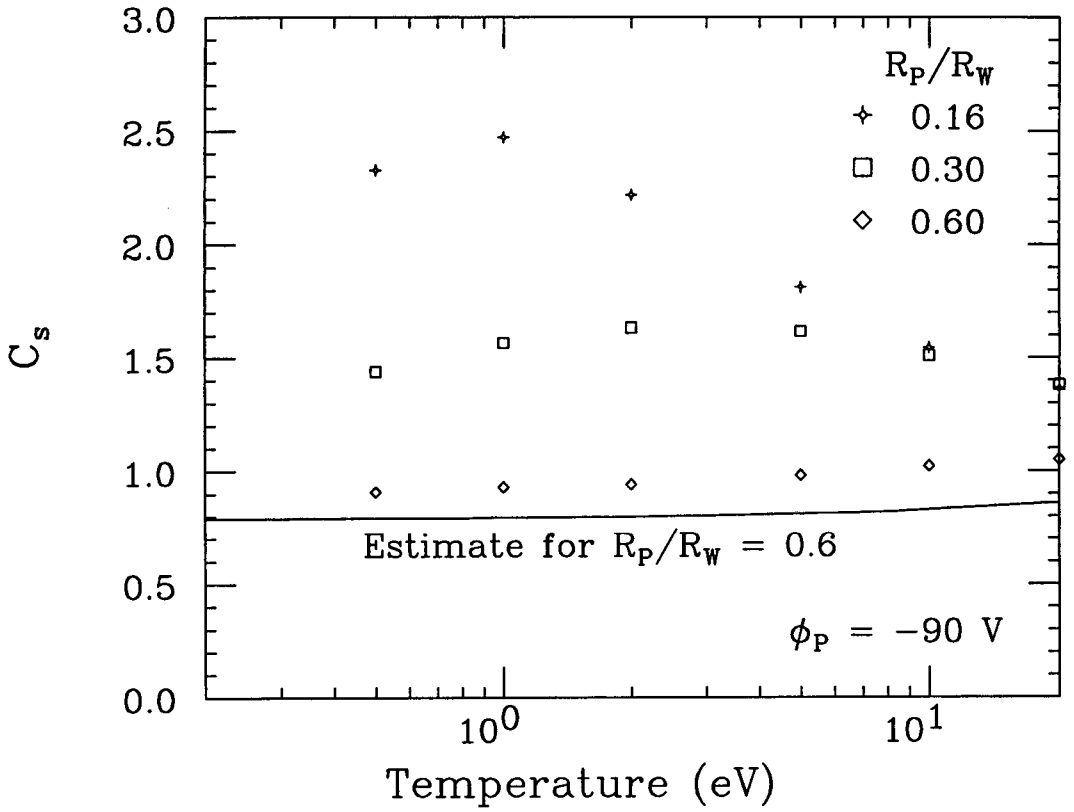


**Figure B.2:** The slant coefficient is independent of the plasma temperature for wide plasmas, but decreases with temperature for narrow plasmas. The solid line shows the estimate from Equation B.13.

increases only about 15%. This increase is predicted by Equation B.13, as shown by the solid curve, even though the predicted values are only about 85% of the numerical values. The kinetic energy of the electrons increases with temperature, which makes the azimuthal asymmetry of the image charge potential becomes less significant. The estimate for the narrower plasmas is nearly the same as for the plasma with $R_p/R_w = 0.6$. However, the numerically calculated slant coefficient of the narrower plasmas has a strong temperature dependence. For $R_p/R_w = 0.16$, $C_s$ decreases from 2.5 to 1.4 as $T$ increases from 1 to 20 eV. This is probably due to a decrease in space charge effects as the Debye length increases, as discussed below.

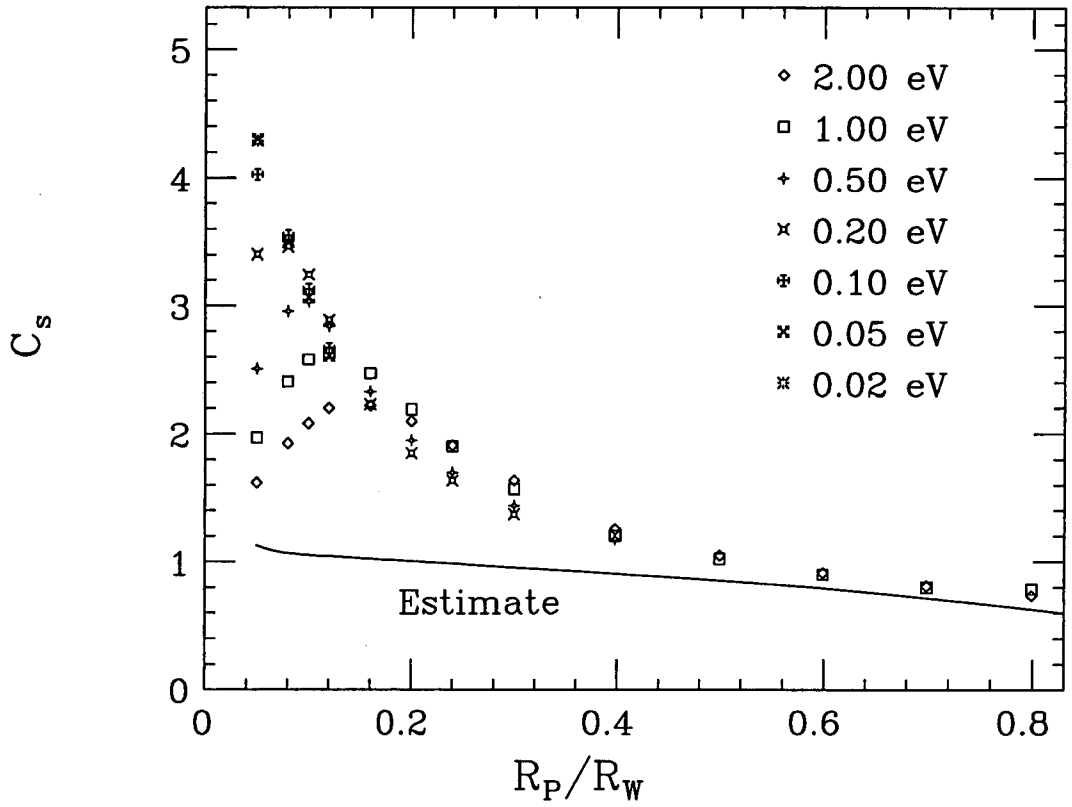


**Figure B.3:** Equation B.13 correctly predicts the slant coefficient of wide plasmas, but underestimates it for narrow plasmas. The discrepancy decreases as the temperature increases.

### B.3.3 Plasma Radius

As is evident from Figure B.2, the slant coefficient depends strongly on $R_p/R_w$. This is better shown by Figure B.3. At large $R_p/R_w$, the numerical $C_s$ at any given temperature agree fairly well with the prediction of Equation B.13, but as $R_p/R_w$ decreases, the numerical values of $C_s$ start to increase, diverging from the estimate. Finally, at even smaller $R_p/R_w$, the numerical $C_s$ start to decrease again. The point at which this decrease occurs depends on temperature; the lower the temperature, the smaller the value of $R_p/R_w$ at which $C_s$ starts decreasing. For small enough temperature or large enough $R_p$, the slant coefficient is nearly independent

of temperature for all $R_p$.

The lowest temperature points in Figure B.3 give the same dependence of $C_s$ with $R_p/R_w$ as Peurrung and Fajans found numerically for a zero temperature plasma, though my data has less noise. Peurrung and Fajans speculated that the anomalous increase in $C_s$ at small $R_p/R_w$ occurs because the end of the plasma becomes more rounded as $R_p$ decreases. This reasoning is valid, since the anomalous increase is presumably due to the change in the space-charge potential caused by the displacement of the plasma column. The axial component of the space-charge electric fields at the plasma end is larger for plasmas with rounded ends than plasmas with flat ends. Therefore, changing the space-charge electric fields causes a larger $\delta L$ in plasmas with rounded ends than in those with flat ends. This explains why $C_s$ decreases with $R_p$ at large $T$; hotter plasmas have flatter ends [48].

## B.4 Numerical Calculations of $\delta L$ for Ill-Confined Plasmas

Near the boundary between a confining cylinder and a grounded cylinder, the vacuum equipotentials have less curvature than well within the grounded cylinder, as is shown in Figure 4.12. This can cause $C_s$ to deviate from the behavior shown above for well-confined plasmas.

Figure B.4 shows $C_s$ as a function of temperature calculated for the data in Figure 4.8. The two different symbols correspond to two different confinement potentials. The "ill-confined" data points show $C_s$ for a plasma confined by the actual confinement potentials used in the experiment, whereas the "well-confined" points show $C_s$ for the same plasma confined by potentials of the form given by Equation B.14. The solid line shows the estimate of $C_s$ for a well-confined plasma from Equation B.13. At low temperatures, $C_s$ for the ill-confined plasma is 1.3 times

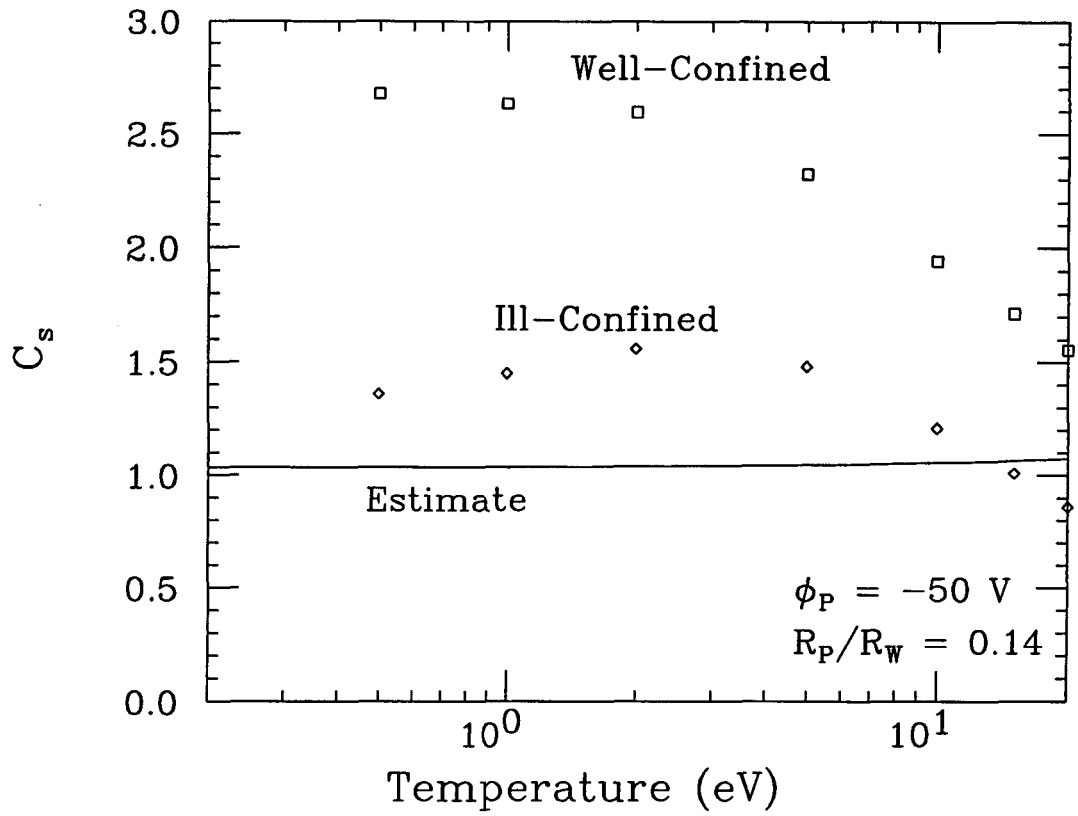


**Figure B.4:** The slant coefficient for a narrow plasma decreases with temperature because the Debye length increases. The slant coefficient of an ill-confined plasma also decreases because it becomes more ill-confined. The solid line shows the estimate from Equation B.13.

the estimate, indicating that space charge effects are acting to increase $\delta L$. The slant coefficient of the well-confined plasma is twice that of the ill-confined plasma, indicating that the well-confined vacuum equipotentials have more curvature than those in the actual experiment. At temperatures above 2 eV, the slant coefficient of both plasmas decreases, indicating that this decrease is mainly due to a decrease in space charge effects. However, $C_s$ decreases more, relative to its low temperature value, for the ill-confined plasma than for the well-confined one. This is because the high energy electrons in the experiment are penetrating farther into the confining potentials towards the end cylinders, where the vacuum equipotentials have less

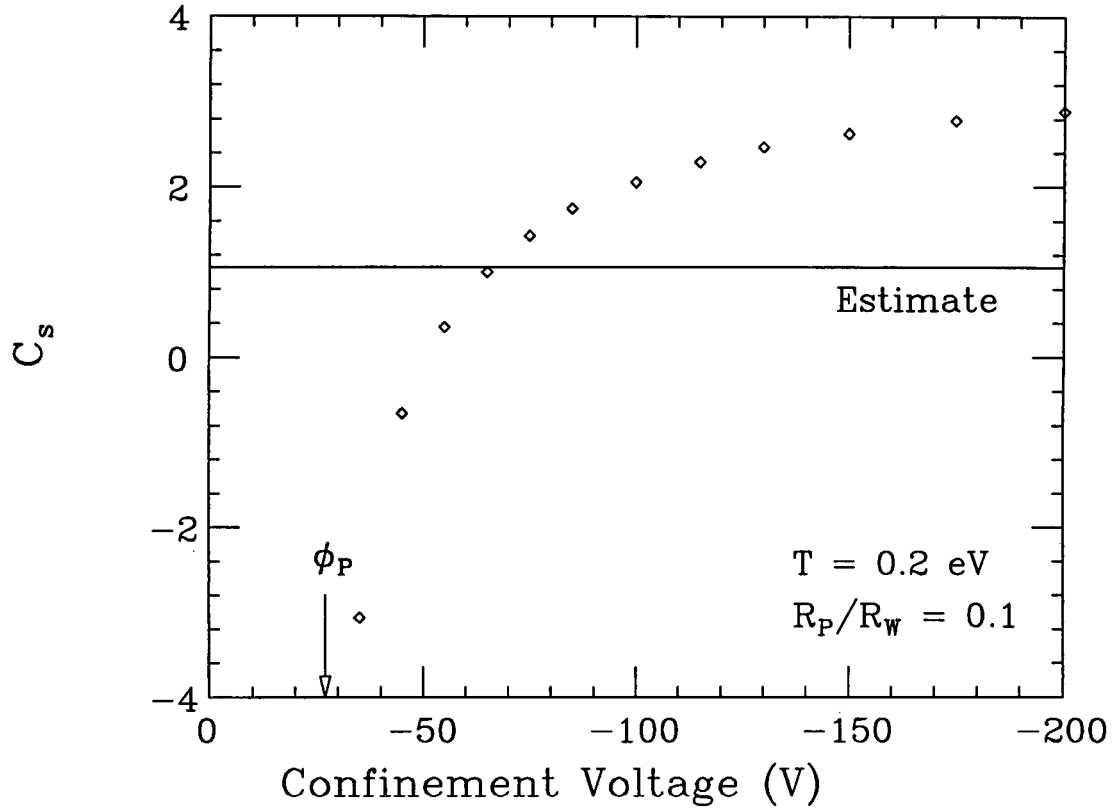


**Figure B.5:** The slant coefficient for an ill-confined plasma decreases with $|V_c|$ because the vacuum equipotentials have less curvature near the confinement boundary. At small enough $|V_c|$, the center of the plasma is inside the confining cylinder, where the equipotentials have opposite curvature, giving negative $C_s$. The solid line shows the estimate from Equation B.13.

curvature.

Figure B.5 shows that the slant coefficient of an ill-confined plasma decreases when the magnitude of the confining potential is decreased. These slant coefficients were calculated for the data in Figure 4.11. The arrow indicates the plasma potential $\phi_p$ when $V_c = -150$ V. As $V_c$ becomes less negative, $C_s$ decreases because the end of the plasma extends further into the low curvature region of the vacuum equipotentials. At $V_c = -50$V, the confining potential at the boundary between the grounded and end cylinders is about equal to the plasma space charge potential

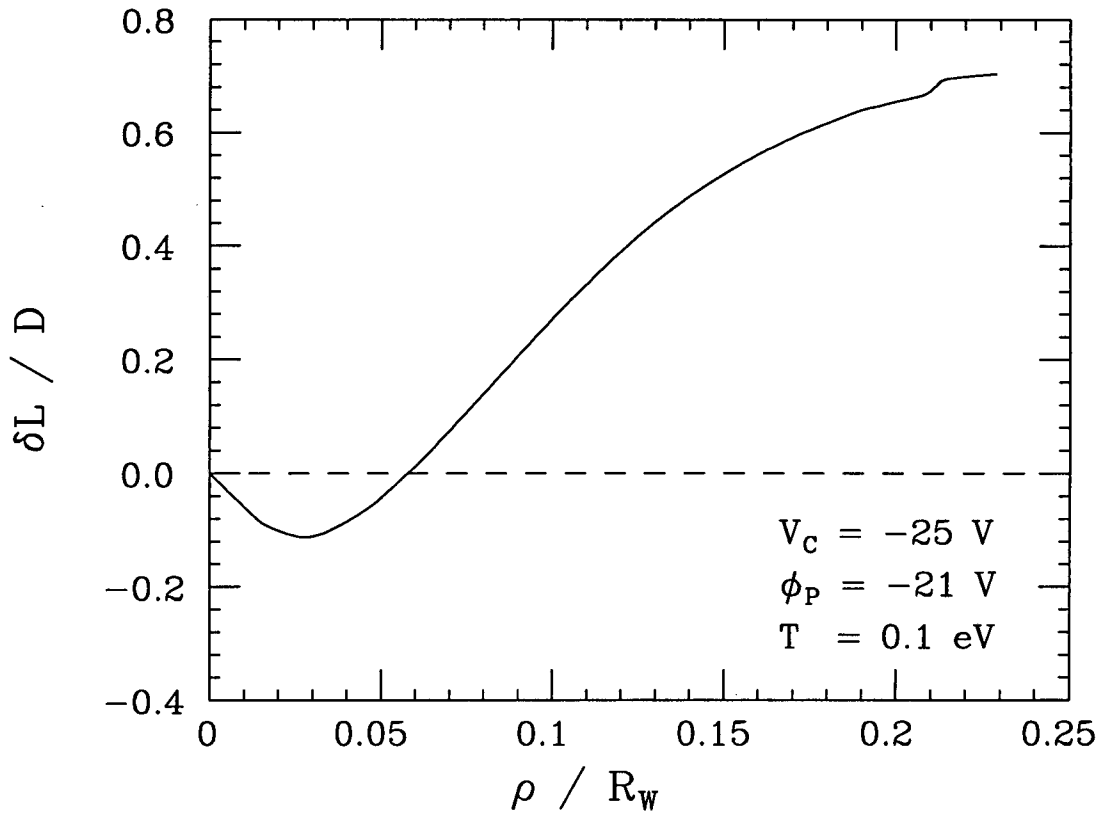


**Figure B.6:** The center of this ill-confined plasma is inside the confining cylinder, while the edge is well into the grounded cylinder. This gives a negative $\delta L$ near $\rho = 0$ but a large, positive $\delta L$ at the plasma edge.

of -25 V. The confining equipotentials at this boundary have no curvature, so the slant coefficient is zero. As $|V_c|$ is decreased further, the end of the plasma extends into the confining cylinder, where the curvature of the confining equipotentials is the opposite of the curvature in the grounded cylinder. This changes the sign of $C_s$.

The $z$ dependence of the curvature of the vacuum equipotentials does more than just change $C_s$. It can also give $\delta L$ a nonlinear dependence on $\rho$. Figure B.6 shows $\delta L(\rho)$, scaled by the displacement $D$, at $V_c$ = -25V for the same plasma as in Figure B.5. Near $\rho = 0$, $\delta L$ decreases strongly with $\rho$, giving a slant coefficient of $C_s$ = -8.0. However, $\delta L$ increases strongly with $\rho$ for $\rho/R_w > 0.06$. This nonlinear dependence on $\rho$ occurs because the plasma end is very rounded. The center of

the plasma extends into the confining cylinder, but the edges are still relatively well confined within the grounded cylinder. This sort of nonlinear $\delta L$ is included in the calculation of $\gamma_{rp}$ in Chapters 4 and 5 by numerically integrating Equation 4.21 over the plasma; whereas the calculation of $\gamma_{est}$ from Equation 4.22 assumes that $dL \propto \rho$.

# Appendix C

# Radiation Limit to Plasma Lifetime

In this Appendix, I consider the loss of angular momentum from a pure electron plasma by cyclotron radiation, and derive an estimate of the rate of expansion of the plasma column due to this process. This rate sets an upper limit on the plasma confinement time, as shown in Figure 3.1.

The total angular momentum of a pure electron plasma, $P_\theta$, is given by Equation 3.1, which is reproduced here:

$$P_\theta = \int d^3r\, n(m_e\mathbf{v} - \frac{e}{c}\mathbf{A}) \cdot r\hat{\theta} = \int d^3r\, nm_e(v_\theta r - \omega_c\frac{r^2}{2}), \quad . \tag{C.1}$$

In Section 3.2, the first term, which is the inertial component, was neglected because it is much smaller than the electromagnetic component. Here, I will keep both terms.

Consider a long, azimuthally symmetric plasma column which is centered on the trap axis. Assuming the plasma is uniform over its length $L_p$, the angular momentum can be written

$$P_\theta = 2\pi L_p \int_0^{R_w} r\, dr\, nm_e \left[(v_E + v_D)r - \omega_c\frac{r^2}{2}\right], \tag{C.2}$$

where the $\mathbf{E} \times \mathbf{B}$ drift velocity, $v_E$, is given by

$$v_E(r) = -\frac{E_r(r)}{B}c = \frac{4\pi ec}{B}\int_0^r r'dr'n(r'), \tag{C.3}$$

and the diamagnetic drift velocity, $v_D$, is given by

$$v_D(r) = -\frac{1}{nm_e\omega_c}\frac{\partial(nT_\perp)}{\partial r}, \tag{C.4}$$

where $\omega_c$ is the cyclotron frequency and $T_\perp$ is the perpendicular temperature. Solving the integral in Equation C.2 gives

$$P_\theta = \frac{1}{2}Nm_e\omega_c\left[2N_L\frac{m_ec^2}{B^2} + 4\frac{H_\perp/N}{m_e\omega_c^2} + R_w^2 - \langle r^2\rangle\right], \tag{C.5}$$

where $N_L = N/L_p$ is the number of electrons per unit length, and $H_\perp$ is the total perpendicular thermal energy, given by

$$H_\perp = 2\pi L_p\int_0^{R_w} r\,dr\;nT_\perp. \tag{C.6}$$

The first term in Equation C.5, which is due to $v_E$, is a constant, provided that $N$ and $L_p$ are constant. The $R_w^2$ term, due to image charges, is also a constant. Thus, $P_\theta$ can change only if $H_\perp$ or $\langle r^2\rangle$ changes.

The perpendicular energy of the electrons decreases through cyclotron radiation. Assuming that the wavelength of the radiation is short compared to the dimensions of the trap, the electrons radiate as $m = 1$ electric dipoles in free space [44]. The ratio of angular momentum to energy radiated by a dipole oscillating at frequency $\omega_c$ is $1/\omega_c$ [32]. Thus, if the plasma is optically thin, the loss rate of angular momentum from the plasma due to radiation is given by

$$\left(\frac{dP_\theta}{dt}\right)_{rad} = -3\frac{H_\perp/\omega_c}{\tau_{rad}}, \tag{C.7}$$

where $\tau_{rad}$ is the radiative cooling time for a single particle when the perpendicular and parallel temperatures are collisionally coupled. This assumes that the walls of the trap are sufficiently resistive to absorb the radiation before the optically thin plasma absorbs it.

If the plasma is not externally heated, $H_\perp$ quickly approaches zero. In that case, the loss of angular momentum through cyclotron radiation is negligible compared to the total angular momentum. However, if the plasma is actively heated

by the application of an azimuthally symmetric voltage, the competition between heating and cyclotron cooling keeps $H_\perp$ constant. The total loss of angular momentum due to radiation can then be many times the thermal component of $P_\theta$. The azimuthally symmetric heating voltage increases the parallel energy of the electrons but not their angular momentum. Collisions transfer this parallel energy to the cyclotron motion of the electrons, which increases $H_\perp$. The collisions must conserve angular momentum, so that the increase in the thermal part of $P_\theta$ must be accompanied by an increase in $\langle r^2 \rangle$. Ignoring other transport processes, if $H_\perp$ is constant, the rate of increase of $\langle r^2 \rangle$ is given by

$$\frac{d\langle r^2 \rangle}{dt} = 6\frac{H_\perp/(Nm_e\omega_c^2)}{\tau_{rad}}, \tag{C.8}$$

which means that $\langle r^2 \rangle$ increases linearly with time. Defining $\tau_m$ as the time required for $\langle r^2 \rangle$ to double gives

$$\tau_m = \frac{\langle r^2(t=0) \rangle}{6H_\perp/(Nm_e\omega_c^2)}\tau_{rad}. \tag{C.9}$$

For a plasma of uniform density and temperature with radius $R_p$, this equation becomes

$$\tau_m = \frac{1}{12}\left(\frac{R_p}{r_c}\right)^2 \tau_{rad}, \tag{C.10}$$

where $r_c = \sqrt{kT_\perp/m_e}/\omega_c$ is the mean cyclotron radius.

# Appendix D

# Damping of $m \geq 2$ Diocotron Modes by Rotational Pumping

Rotational pumping presumably damps the $m \geq 2$ diocotron modes just as it does the $m = 1$ mode. In this Appendix, I derive an estimate of the rotational pumping damping rate for the $m \geq 2$ modes. I find that, for $R_p \ll R_w$, the damping rate for all $m$ numbers is nearly identical.

Consider a long ($L_p \gg R_w$) plasma column which has uniform density and temperature. In the diocotron mode frame, the diocotron mode is simply a stationary distortion of the plasma cross-section. The radial distance from the axis to the surface of the plasma, $R_s$, can be described by

$$R_s(\theta) = \frac{R_p}{(1 + a_m^2/8)^{1/2}}(1 - \frac{a_m}{2}\cos m\theta), \tag{D.1}$$

where $a_m \ll 1$ is the amplitude of the mode and $R_p$ is radius of the column when $a_m = 0$. The $\mathbf{E} \times \mathbf{B}$ orbits of the electrons are likewise distorted. To lowest order in $a_m$, the radial excursions of an electron caused by an $m \geq 2$ diocotron mode can be described by

$$r_m(\theta) = r_0(1 - \frac{a_m}{2}\cos m\theta), \tag{D.2}$$

where $a_m \ll 1$ is the amplitude of the mode and $r_0$ is the mean radial location of the electron.

The radial excursions of the electrons cause the length of a tube of plasma to vary as it $\mathbf{E} \times \mathbf{B}$ drifts around the plasma axis. This length variation can be described by

$$L(r_0, t) = L_0(r_0) - \delta L(r_0) \cos m\omega_R t, \tag{D.3}$$

where $\delta L \ll L_0$ and $\omega_R(r_0)$ is the rotation frequency of the plasma in the diocotron mode frame. Inserting Equation D.2 into Equation B.3 gives (including both ends of the plasma)

$$\delta L(r_0) \equiv z_{eq}(\, r_m(0)\,) - z_{eq}(\, r_m(\pi/m)\,) \approx \frac{\kappa}{2}\frac{r_0}{R_w} r_0 a_m, \tag{D.4}$$

where $\kappa = j_{01} \approx 2.4$.

Equation 4.12 gives the rotation-averaged rate of change of the $z$-integrated thermal energy density of the tube of plasma as

$$\frac{3}{2} n_z \frac{dT}{dt} = 2 n_z k T \nu_{\perp\parallel} \left(\frac{\delta L}{L_0}\right)^2. \tag{D.5}$$

Integrating this equation gives the rate of change of the thermal energy of the plasma, i.e.

$$\frac{dH_T}{dt} = \frac{2\pi}{N}\int_0^{R_p} r_0\, dr_0\, \frac{3}{2} n_z \frac{dT}{dt} = \frac{1}{6}\kappa^2 \nu_{\perp\parallel} T \frac{R_p^4}{L_0^2} a_m^2, \tag{D.6}$$

where $H_T$ is the thermal energy per electron, and where $L_0$ is assumed to be uniform over the plasma.

Conservation of energy stipulates that the increase in $H_T$ must come from a decrease in the electrostatic energy of the plasma, $H_\phi$, through Joule heating. The electrostatic energy per electron is given by

$$H_\phi = N_L e^2 \left\{ \left[ \ln\left(\frac{R_w}{R_p}\right) + \frac{1}{4} \right] - \left[ \frac{1}{m}\frac{a_m^2}{4}\left(1 - \left(\frac{R_p}{R_w}\right)^{2m}\right)\right]\right\}, \tag{D.7}$$

The first term is from the self energy of the column, and the second is from the energy of the mode. The $(R_p/R_w)^{2m}$ term is due to the image charges induced by

the mode. Taking a time derivative of this equation gives

$$\frac{dH_\phi}{dt} \approx N_L e^2 \left( -\frac{1}{R_p}\frac{dR_p}{dt} - \frac{1}{2m} a_m \frac{da_m}{dt}(1-(R_p/R_w)^{2m}) \right), \tag{D.8}$$

where I have kept only the lowest order terms in $a_m$. This equation shows that the change in electrostatic energy is caused by the expansion of the plasma column and the decrease in the mode amplitude. The rate of change of $R_p$ and $a_m$ are related through the conservation of angular momentum. To lowest order in $a_m$, the total angular momentum is given by

$$P_\theta \approx \frac{N m_e \omega_c}{2} \int_0^{2\pi} d\theta \int_0^{R_s(\theta)} r\, dr\, n_z r^2 \propto \frac{R_p}{2}(1+\frac{1}{2}a_m^2). \tag{D.9}$$

Setting the the time derivative of Equation D.9 to zero gives

$$\frac{1}{R_p}\frac{dR_p}{dt} = -\frac{1}{2} a_m \frac{da_m}{dt}. \tag{D.10}$$

Inserting this into Equation D.8 and defining the damping rate, $\gamma_m$ , by $da_m/dt = -\gamma_m a_m$, gives

$$\frac{dH_\phi}{dt} = -\frac{1}{2} N_L e^2 a_m^2 \frac{m}{m-1+(R_p/R_w)^{2m}} \gamma_m. \tag{D.11}$$

The damping rate of the mode can now be obtained by using conservation of energy to set the sum of Equations D.6 and D.11 to zero. This gives

$$\gamma_m = \frac{4}{3}\kappa^2 \nu_{\perp\|} \left(\frac{\lambda_D}{L_0}\right)^2 \frac{m\,(R_p/R_w)^2}{m-1+(R_p/R_w)^{2m}}. \tag{D.12}$$

Note that $\gamma_m$ depends only weakly on $m$ through the last term. If $R_p/R_w$ is small, $\gamma_m$ is the same as $\gamma_{est}$ from Equation 4.22, except for a numerical constant. That is, Equation D.12 predictes that the damping rates of the $m \geq 2$ diocotron modes due to rotational pumping should be nearly identical to the damping rate of the $m = 1$ diocotron mode. This has not been tested experimentally, however.

# Appendix E

# Damping of Diocotron Modes by Shear Viscosity

From a fluid perspective, rotational pumping can be thought of as dissipation of fluid compressions by a second viscosity. (See Section 4.6.3.) Presumably, the first, or shear, viscosity also acts to damp the diocotron modes. In this Appendix, I derive an estimate of the damping rates of the linear diocotron modes due to shear viscosity.

In Section E.1, I derive the damping rate of the $m \geq 2$ modes. I find that the damping rate increases with $m$ and in some parameter regimes can be larger than the rotational pumping damping rate. In Section E.2, I derive the damping rate of the $m = 1$ mode. Because the shears induced by the $m = 1$ mode are nonlinear in the mode amplitude, the shear viscosity damping rate is small compared to the rotational pumping rate. In Section E.3, I show how viscosity, acting on internal shears, can move the center of mass of the plasma to damp the $m = 1$ mode. The viscous forces modify the equilibrium plasma shape, which changes the distribution of image charges. The perturbed image charge fields cause the plasma to $\mathbf{E} \times \mathbf{B}$ drift back towards the trap axis.

## E.1 Damping of $m \geq 2$ Modes

I derive the shear-induced damping rate of the diocotron modes by using conservation of energy and angular momentum, much the same way as I derived the damping rate of the $m \geq 2$ modes due to rotational pumping in Appendix D. Consider an infinitely long plasma column which has uniform density and temperature. In the diocotron mode frame, the mode is simply a stationary distortion of the plasma cross-section. The radial distance from the axis to the surface of the plasma, $R_s(\theta)$, can be described by Equation D.1. Similarly the angular momentum of the column can be described by Equation D.9.

The electrostatic potential inside the plasma due to a small amplitude diocotron mode of mode number $m$ can be written as

$$\phi_m = \frac{1}{m} a_m N_L e \left(\frac{r}{R_p}\right)^m \left(1 - \tilde{r}_p^{2m}\right) \cos m\theta, \tag{E.1}$$

where $a_m \ll 1$ is the mode amplitude, $R_p$ is the mean plasma radius, $N_L = n\pi R_p^2$ is the number of electrons per unit length in the column, and $\tilde{r}_p = R_p/R_w$ is the scaled plasma radius. The $\tilde{r}_p^{2m}$ term is due to the image charges induced by the mode. The electric fields, and hence the $\mathbf{E} \times \mathbf{B}$ drift velocity of the plasma, can be obtained by taking the gradient of the potential. This gives

$$v_r = \frac{a_m}{2} \omega_E R_p \left(\frac{r}{R_p}\right)^{m-1} \left(1 - \tilde{r}_p^{2m}\right) \sin m\theta, \tag{E.2}$$

$$v_\theta = \frac{a_m}{2} \omega_E R_p \left(\frac{r}{R_p}\right)^{m-1} \left(1 - \tilde{r}_p^{2m}\right) \cos m\theta + r\omega_R \tag{E.3}$$

where $\omega_E = 2\pi nec/B$ is the $\mathbf{E} \times \mathbf{B}$ rotation frequency of the plasma in the lab frame. For completeness, I have added to $v_\theta$ the rotation velocity of the plasma in the diocotron mode frame, $r\omega_R$, due to the self electric field of the plasma column. This uniform rotation does not contribute to the damping of the mode, however.

The components of the rate of strain tensor, $W_{jk}$, can be calculated from the

$\mathbf{E} \times \mathbf{B}$ velocity. The 4 components are

$$W_{rr} \equiv 2\frac{\partial v_r}{\partial r} = \Omega_m(r)\sin m\theta, \quad \text{(E.4)}$$

$$W_{\theta\theta} \equiv \frac{2}{r}\frac{\partial v_\theta}{\partial \theta} + \frac{2v_r}{r} = -\Omega_m(r)\sin m\theta, \quad \text{(E.5)}$$

$$W_{r\theta} = W_{\theta r} \equiv \frac{1}{r}\frac{\partial v_r}{\partial \theta} + \frac{\partial v_\theta}{\partial r} - \frac{v_\theta}{r} = \Omega_m(r)\cos m\theta, \quad \text{(E.6)}$$

where $\Omega_m(r) = (m-1)a_m\omega_E(r/R_p)^{m-2}(1-\tilde{r}_p^{2m})$. Using the $W_{jk}$, I calculate the rate of increase of thermal energy per electron, $H_T$, due to dissipation of the $\mathbf{E} \times \mathbf{B}$ flow by the shear viscosity. The rate of change of $H_T$ in a length $L$ of plasma is given by

$$\frac{1}{L}\frac{dH_T}{dt} = \frac{1}{2N}\eta\int_0^{2\pi} d\theta \int_0^{R_p} r dr \sum_{j,k} W_{jk}^2 = 2\frac{\eta}{nL}\frac{(m-1)^2}{m}\omega_E^2 a_m^2\left(1-\tilde{r}_p^{2m}\right)^2, \quad \text{(E.7)}$$

where $\eta$ is the coefficient of shear viscosity. Conservation of energy stipulates that the increase in thermal energy comes from a decrease in the electrostatic energy, $H_\phi$, due to Joule heating as the plasma expands and the mode damps. Using Equation D.11 to relate $dH_\phi/dt$ to the damping rate of the mode, $\gamma_m$, and setting $d(H_T+H_\phi)/dt = 0$, gives

$$\gamma_m = 4\frac{\omega_p^2}{\omega_c^2}\frac{\mu}{R_p^2}\frac{(m-1)^2(1-\tilde{r}_p^{2m})}{m-1+\tilde{r}_p^{2m}}, \quad \text{(E.8)}$$

where $\omega_p$ is the plasma frequency, $\omega_c$ is the cyclotron frequency, and $\mu$ is the kinematic viscosity, i.e. $\mu = \eta/nm_e$. Note that if the image charge effects can be neglected, i.e. $\tilde{r}_p^{2m} \ll 1$, the damping rate is proptional to $m-1$. The higher the mode number, the larger the shears, and the stronger the viscous dissipation.

The best developed theory of shear viscosity in pure electron plasmas is by O'Neil [45, 46], who postulated that the electrons diffuse mainly through $\mathbf{E} \times \mathbf{B}$ drifts. O'Neil's viscosity coefficient can be expressed as

$$\mu = \frac{\sqrt{\pi}}{6} nb^2\bar{v}\,\lambda_D^2\,\ln(\lambda_D/r_c), \quad \text{(E.9)}$$

where $b$ is the distance of closest approach, $\bar{v}$ is the thermal velocity, and $\lambda_D$ is the Debye length. Substituting this expression into Equation E.8, it is evident that $\gamma_m$

should be largest for a narrow, high density, cold plasma in a weak magnetic field. Inserting the plasma parameters from Figure 4.16 and a temperature of 0.003 eV into Equation E.8 gives a shear viscosity damping rate of $\gamma_m = 0.10$ sec$^{-1}$ for the $m = 2$ diocotron mode. This is much larger than the rotational pumping rate of 0.0016 sec$^{-1}$ given by Equation D.12, because the shear viscosity is not suppressed when $r_c < b$, as is the second viscosity. When $r_c > b$, the rotational pumping rate is generally larger for CV plasma parameters.

## E.2 Damping of the $m = 1$ Mode

The $m = 1$ diocotron mode differs from the other diocotron modes in that it is a displacement and distortion of the the plasma column rather than a just a distortion. Consider an infinitely long plasma column of uniform density and temperature which is displaced a distance $D$ from the trap axis. In the frame of the diocotron mode, the column is circular to first order in $D/R_w$, and the mode is undamped by shear viscosity. However, the image charges cause straining fields to second order in $D/R_w$, resulting in an elliptical distortion of the plasma column. Fine [18] has shown that the equilibrium quadrupole moment, $q_2$, of this distortion is given by

$$q_2 = 2\frac{\tilde{r}_p^2}{(1-\tilde{r}_p^2)^2}\left(\frac{D}{R_w}\right)^2, \tag{E.10}$$

where $\tilde{r}_p = R_p/R_w$ is the scaled plasma radius.

There are 4 sources of electric fields in the rotating frame of the diocotron mode. These are

1. the self field of the plasma,

2. the $m = 1$ image charge fields,

3. the fields due to the elliptical distortion, and

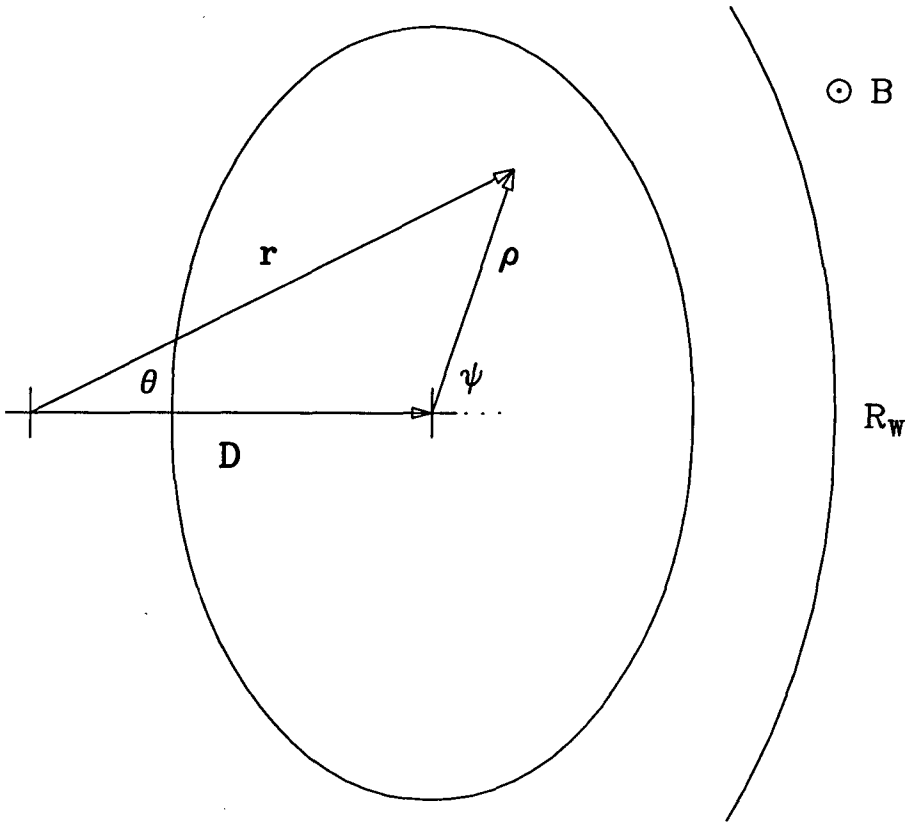


**Figure E.1:** Plasma centered coordinates for off-axis plasma. The straining field from the image charges gives the plasma an elliptical cross-section.

4. the $\mathbf{v} \times \mathbf{B}$ fields due to the rotating frame.

To second order in $D/R_w$, the $\mathbf{E} \times \mathbf{B}$ drift velocities due to all these fields are, in plasma centered coordinates,

$$v_\rho = q_2 \omega_E R_p \frac{\rho}{R_p} \left(1 - \tilde{r}_p^2\right) \sin 2\psi, \tag{E.11}$$

$$v_\psi = q_2 \omega_E R_p \frac{\rho}{R_p} \left(1 - \tilde{r}_p^2\right) \cos 2\psi + \rho \omega_R, \tag{E.12}$$

where $\omega_E$ is the $\mathbf{E} \times \mathbf{B}$ rotation frequency of the plasma around the center of charge in the lab frame, and $\omega_R$ is the rotation frequency of the plasma in the diocotron mode frame. The coordinates $(\rho, \psi)$ are measured from the center of charge of the plasma, as shown in Figure E.1. These velocities are almost the same as $(v_r, v_\theta)$ given

by Equations E.2 and E.3 for an $m = 2$ diocotron mode of amplitude $a_2 = 2q_2$. Thus, I can immediately write down the rate of change of thermal energy (per electron per length $L$) as

$$\frac{1}{L}\frac{dH_T}{dt} = 4\frac{\eta}{nL}\omega_E^2 q_2^2 \left(1 - \tilde{r}_p^2\right)^2. \tag{E.13}$$

The electrostatic energy per electron, to lowest order in $D/R_w$, is given by

$$\frac{H_\phi}{L} = \frac{1}{L}N_L e^2 \left\{ \left[ \ln\left(\frac{R_w}{R_p}\right) + \frac{1}{4} \right] - \frac{D^2}{R_w^2} \right\}, \tag{E.14}$$

and the rate of change of $H_\phi$ is given by

$$\frac{1}{L}\frac{dH_\phi}{dt} \approx -\frac{2}{L}N_L e^2 \left(\frac{1}{R_w^2} - \frac{1}{R_p^2}\right) D\frac{dD}{dt}. \tag{E.15}$$

Conservation of angular momentum gives

$$R_p\frac{dR_p}{dt} = -2D\frac{dD}{dt}. \tag{E.16}$$

Defining the damping rate of the mode by $dD/dt = -\gamma_1 D$ then gives

$$\frac{1}{L}\frac{dH_\phi}{dt} \approx -\frac{2}{L}N_L e^2 \frac{D^2}{R_p^2}\left(1 - \tilde{r}_p^2\right)\gamma_1. \tag{E.17}$$

Finally, using conservation of energy to set $d(H_T + H_\phi)/dt = 0$, inserting the expression for $q_2$ from Equation E.10 into Equation E.17, and solving for the damping rate gives

$$\gamma_1 = 8\frac{\omega_p^2}{\omega_c^2}\frac{\mu}{R_p^2}\frac{D^2}{R_w^2}\left(\frac{\tilde{r}_p^2}{1 - \tilde{r}_p^2}\right)^3. \tag{E.18}$$

The damping is nonlinear, i.e. $\gamma_1$ depends on $D$, because the elliptical distortion of the plasma is nonlinear in $D$. This also causes the damping to be extremely weak for small $D/R_w$. Comparing to Equation E.8, the damping rate of the $m = 1$ mode due to shear viscosity is a factor of $10^6$ smaller than the $m = 2$ mode for $R_p/R_w = 0.2$ and $D/R_w = 0.1$. Similarly, the shear viscosity damping rate is much smaller than the rotational pumping rate. Inserting the plasma parameters from Figure 4.16 into Equation E.18, along with $T = 0.003$ eV and $D/R_W = 0.1$ gives a damping rate of

$1.8 \times 10^{-10}$ sec$^{-1}$. (Here, as at the end of Section E.2, I have used Equation E.9 for $\mu$.) The shear viscosity rate is small compared to the rotational pumping rate for the $m = 1$ mode, even when $r_c < b$.

## E.3 Dynamics of the Shear Damping of the $m = 1$ Diocotron Mode

The calculation in the previous section does not explain the origin of the forces which cause the $m = 1$ diocotron mode to damp. The mode damps through the motion of its center of mass, so these forces must be external to the plasma. More precisely, the image charges must provide an electric field in the $-\theta$ direction which is non-zero when integrated over the plasma. Now, Fine [18] has shown that the equilibrium shape of an inviscid plasma in an $m = 1$ diocotron mode orbit is an ellipse with its long axis aligned with direction of motion. The image charge fields in the $\theta$ direction produced by this equilibrium are zero when integrated over the plasma. Therefore, the viscous forces must produce a new, quasi-equilibrium in order to damp the mode. Specifically, the ellipse is rotated in the in the $-\psi$ direction, as shown in Figure E.2.

In order to find the rotation angle, $\alpha$, the electric and viscous forces on the plasma must be calculated. The lowest order, nonzero viscous forces are proportional to $(D/R_w)^2$. The electric fields to this order are [18]

$$E_\rho = -q_2 n \pi e \rho \left[ \left(1 - \tilde{r}_p^2\right)^2 \cos 2\psi + \left(1 - \tilde{r}_p^4\right) \cos(2\psi + 2\alpha) \right], \qquad \text{(E.19)}$$

$$E_\psi = q_2 n \pi e \rho \left[ \left(1 - \tilde{r}_p^2\right)^2 \sin 2\psi + \left(1 - \tilde{r}_p^4\right) \sin(2\psi + 2\alpha) \right]. \qquad \text{(E.20)}$$

Here, the first term is from image charges induced by the displacement of the plasma from the trap axis; these fields are independent of the rotation angle. The second term is from the elliptical distortion of the plasma and the associated image charges.

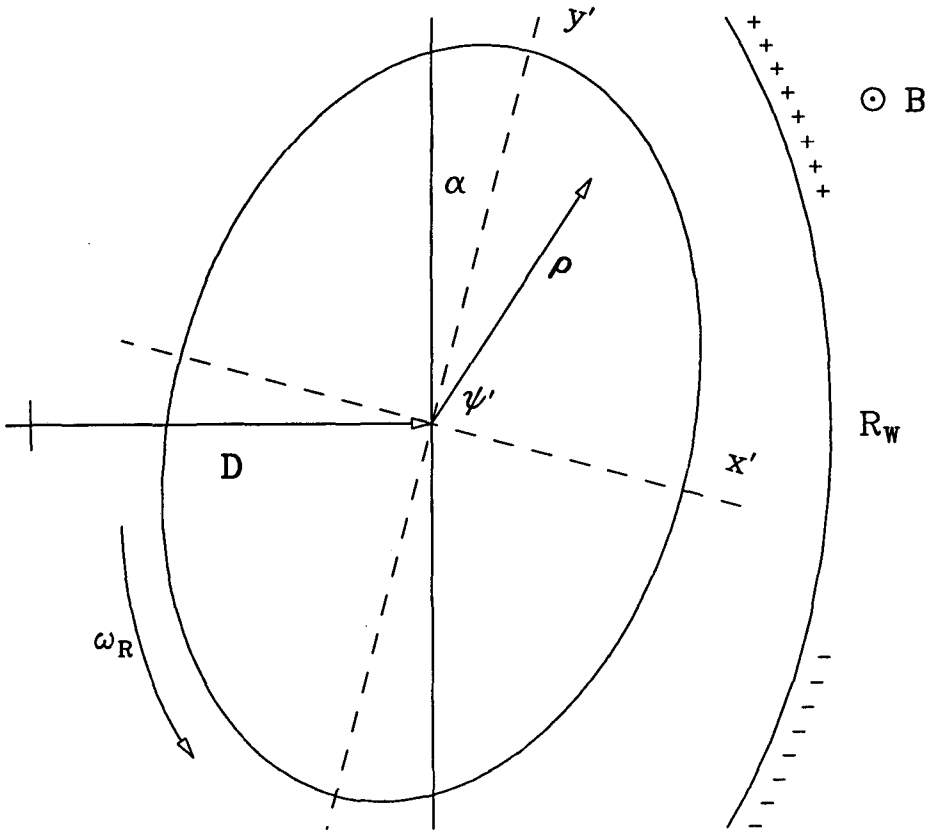


**Figure E.2:** Shear viscosity rotates the elliptical equilibrium shape in the $-\psi$ direction. This increases the positive (negative) image chrages in the $+y'(-y')$ direction, creating an electric field which acts to damp the mode.

The $\mathbf{E} \times \mathbf{B}$ drift velocities of order $(D/R_w)^2$ are obtained from the electric fields, and the rate of strain tensor from these velocities. The viscous forces act only on the surface of the uniform density plasma, i.e. $\partial W_{jk}/\partial x_k = 0$ inside the plasma. The force per unit area on the plasma surface, $\mathbf{p}$, is given by

$$p_\rho = -\eta W_{\rho\rho} = -\eta q_2 \omega_E \left[ \left(1 - \tilde{r}_p^2\right)^2 \sin 2\psi + \left(1 - \tilde{r}_p^4\right) \sin(2\psi + 2\alpha) \right], \quad \text{(E.21)}$$

$$p_\psi = -\eta W_{\rho\psi} = -\eta q_2 \omega_E \left[ \left(1 - \tilde{r}_p^2\right)^2 \cos 2\psi + \left(1 - \tilde{r}_p^4\right) \cos(2\psi + 2\alpha) \right]. \quad \text{(E.22)}$$

The elliptical equilibrium measured by Fine is that of an elliptical vortex in a "pure straining field," as calculated by Saffman [57]. Since the viscous forces do not produce a pure straining field, Saffman's equilibrium is not applicable here. Instead I look for

the rotation angle at which the forces on the elliptical plasma are symmetric across the long axis of the ellipse. That is, the angle at which $\mathbf{F} \cdot \hat{\mathbf{x}}' = F_\rho \cos\psi' - F_\rho \sin\psi'$ is odd in the $x'$ direction and even in the $y'$ direction, where $\mathbf{F}$ is the total force vector and the primed coordinates refer to the rotated coordinate system shown in Figure E.2. Therefore, the equilibrium rotation angle is defined by

$$\int_0^\pi d\psi' \left[ R_p p_{x'} + \int_0^{R_p} -neE_{x'}\rho d\rho \right] = 0, \tag{E.23}$$

which gives a rotation angle of

$$\alpha = \frac{6\mu}{\omega_c R_p^2 (1 - \tilde{r}_p^2)}, \tag{E.24}$$

where $\mu$ is again the kinematic viscosity.

The rotation of the elliptical equilibrium perturbs the image charges. The rotated equilibrium induces more positive image charges in the $+y'$ direction than in the $-y'$ direction, as shown in Figure E.2. The order $(D/R_w)^3$ component of the potential of the perturbed image charges is [18]

$$\phi_i^{(3)} = -q_2 n\pi e \tilde{r}_p^4 D\rho \left[ \cos(\psi + 2\alpha) + \frac{\rho^2}{R_w^2} \cos(3\psi + 2\alpha) \right], \tag{E.25}$$

where the superscript indicates that this is only the order $(D/R_w)^3$ component of the perturbed image charge potential. This potential gives rise to electric fields which, in turn, give rise to $\mathbf{E} \times \mathbf{B}$ drifts. The damping rate of the $m = 1$ diocotron mode is then given by

$$\gamma_1 \equiv -\frac{1}{D}\frac{dD}{dt} = -\frac{1}{DN_L} \int_0^{2\pi} d\psi \int_0^{R_p} n\, \rho\, d\rho\, (v_\rho \cos\psi - v_\psi \sin\psi). \tag{E.26}$$

It is evident that only terms in $v_\rho(v_\psi)$ proportional to $\cos\psi(\sin\psi)$ will give a nonzero contribution to $\gamma_1$. To order $(D/R_w)^3$, the only term that satisfies this condition comes from the first term in Equation E.25. This gives a damping rate of

$$\gamma_1 = q_2 \omega_E \tilde{r}_p^4 \alpha = 6 \frac{\omega_p^2}{\omega_c^2} \frac{\mu}{R_p^2} \frac{D^2}{R_w^2} \left( \frac{\tilde{r}_p^2}{1 - \tilde{r}_p^2} \right)^3. \tag{E.27}$$

which is the same, except for a factor of 4/3, as the damping rate in Equation E.18. The factor of 4/3 is presumably due to the *ad hoc* definition of the rotation angle given by Equation E.23. A more formal definition should give closer agreement with Equation E.18.

# Appendix F

# Rotational Pumping Dynamics

The heuristic derivation of the rotational pumping transport rates given in Section 4.4 does not explain how the confining fields cause the plasma to expand and the center of charge to move back to the trap axis. In this Appendix, I calculate the forces on the plasma and find that the collisional perturbation to the parallel temperature, $T_{||}$, produces forces which are not azimuthally symmetric around the plasma axis. I then rederive the radial electron flux and $m = 1$ diocotron mode damping rate given by Equations 4.14 and 4.22 from the drifts arising from these forces.

Consider a plasma with density $n(r,\theta)$ and length $L_0(r,\theta)$. If the Debye length is very small, i.e. $\lambda_D \ll L_0$, then the potential and density along a magnetic field line are constant inside the plasma and abruptly decrease at the end. At each end of the plasma, the force from the confining fields must balance the tendency of the plasma to expand along the field lines. Thus, the $z$-component of the force from the confining fields at one end of the plasma is given by

$$F_z(r,\theta) = \frac{1}{n_z}(nT_{||} + p_\phi), \tag{F.1}$$

where $n_z = nL_0$ is the $z$-integrated density, $nT_{||}$ is the thermal pressure, and $p_\phi$ is the electrostatic "pressure" due to the gradient in the space charge at the end of the plasma. Due to the curvature of the equipotentials (shown in Figure 4.1), there is

also a radial component to the confining electric fields. The radial component of the confining force is, to lowest order in $r/R_w$,

$$F_r = \frac{\kappa r}{2R_w} F_z, \tag{F.2}$$

where Equation B.2 has been used to approximate the confining potential, and $\kappa = j_{01}$ is the 1st zero of the $J_0$ Bessel function.

If the plasma radius were infinitesimally small, $F_r$ would simply cause a shift in the $m = 1$ diocotron mode frequency, as shown by Fine [17]. Combined with electron-electron collisions, however, it causes rotational pumping transport in a finite radius plasma. To demonstrate this, I use the plasma-centered coordinate system shown in Figure E.1. The confining field forces are then given by

$$F_\rho(\rho,\psi) = \frac{\kappa}{n_z R_w}\left(nT_\parallel + p_\phi\right)\left(D\cos\psi + \rho\right), \tag{F.3}$$

$$F_\psi(\rho,\psi) = -\frac{\kappa}{n_z R_w}\left(nT_\parallel + p_\phi\right)\left(D\sin\psi\right), \tag{F.4}$$

Note that I have included the here the force from both ends of the plasma, and have assumed that $F_\theta$ is zero. Using Equation 4.11, the parallel temperature can be written, to first order in $\delta L/L_0$, as

$$T_\parallel(\rho,\psi) = T_0\left[1 - 2\frac{\delta L}{L_0}\left(\cos\psi - \frac{2\nu_{\perp\parallel}}{\omega_R}\sin\psi\right)\right] \tag{F.5}$$

where $\psi = \omega_R t$. The first term in this equation, multiplied by $\rho$ in the expression for $F_\rho$ in Equation F.3, contributes to a shift in the rotation frequency of the plasma. Similarly, the electrostatic pressure contributes to this zero order shift in $\omega_R$. The expansion of the plasma, however, is due to $F_\psi$. The $z$-integrated, $\psi$-averaged radial electron flux is given by

$$\Gamma_\rho \equiv \langle n_z v_\rho\rangle_\psi \equiv \frac{n_z}{2\pi}\int_0^{2\pi} d\psi \frac{cF_\psi}{-eB}. \tag{F.6}$$

The electrostatic pressure, $p_\phi \equiv p_\phi(\rho,\cos\psi)$, makes no contribution to $\Gamma_\rho$ because variations in the electron density are in phase with the variation in the plasma length.

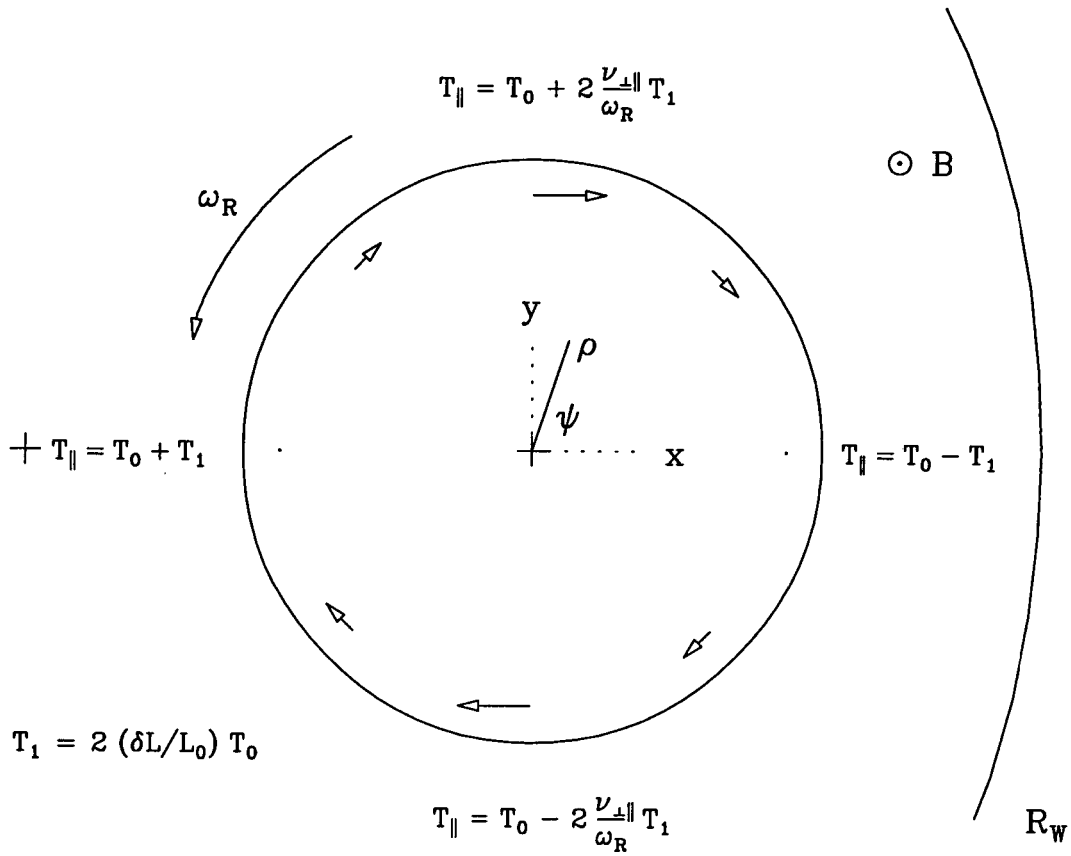


**Figure F.1:** Forces on the plasma from the confining fields. The parallel temperature oscillates in $\psi$, inducing an azimuthal variation in the force from the ends. The arrows show the component of $F_\psi$ which is proportional to $\nu_{\perp\parallel}$; this component causes the plasma to expand.

Comparing to Equations F.4 and F.5, it is apparent that only the collisional term of the thermal pressure makes a non-zero contribution to $\Gamma_\rho$. The collisions induce a phase shift between the thermal pressure and the variation in the plasma length. This is shown schematically in Figure F.1. A tube of plasma drifting around the plasma axis is longest near the wall and shortest near the trap axis. Hence, $T_\parallel$ is hottest near the trap axis and coldest near the wall. Collisions attempt to equilibrate $T_\perp$ and $T_\parallel$, lowering $T_\parallel$ if $T_\parallel > T_\perp$ (or raising $T_\parallel$ if $T_\parallel < T_\perp$), creating a temperature gradient in the $y$ direction. The arrows in Figure F.1 show the azimuthal forces arising from this gradient; i.e. the components of $F_\psi$ which are proportional to $\nu_{\perp\parallel}$. The drifts

caused by these forces result in the expansion of the plasma. Integrating over these drifts (Equation F.6) recovers the the expression for $\Gamma_\rho$ given in Equation 4.14, if Equation B.4 is used for $\delta L$ and the substitution $\omega_R = -E_\rho c/\rho B$ is made.

Similarly, the damping rate of the $m = 1$ diocotron mode can be derived from Equations F.3, F.4, and F.5. Defining an $(x, y)$ coordinate system as shown in Figure F.1, the $x$-component of the drifts induced by the confining forces at the plasma ends is given by

$$v_x = -\frac{c}{eB}(F_\rho \sin\psi + F_\psi \cos\psi). \tag{F.7}$$

The damping rate can be calculated as

$$\gamma = -\frac{1}{N}\int \rho d\rho\, d\psi\, n_z v_x, \tag{F.8}$$

where $N$ is the total number of electrons. As in the expression for $\Gamma_\rho$ in Equation F.6, only the collisional term of the thermal pressure contributes to this integral. If it is assumed that the plasma is uniform in density, integrating Equation F.8 recovers the expression for $\gamma_{est}$ in Equation 4.22 if Equation B.4 is again used for $\delta L$.

# Appendix G

# Symbols and Notations

This appendix lists symbols and notations commonly used in this thesis. Whenever necessary, definition of a symbol or equation number where it is first introduced is given. All equations use the cgs convention.

********** **Fundamental Quantities** **********

| | | |
|---|---|---|
| $-e$ | | Electron charge |
| $m_e$ | | Electron mass |
| $c$ | | Speed of light in vacuum |
| $k$ | | Boltzmann's constant |
| $\mathbf{B}$ | $B\hat{\mathbf{z}}$ | Axial magnetic field |
| $\phi$ | | Electrostatic potential |
| $\mathbf{E}$ | $-\nabla\phi$ | Electric field |
| $T$ | | Plasma temperature |
| $n$ | | Plasma density |
| $(r, \theta, z)$ | | Cylindrical coordinate system centered on the trap axis. |
| $(\rho, \psi, z)$ | | Cylindrical coordinate system centered on the plasma axis. |
| $t$ | | Evolution time |

## ********** Energies and Velocities **********

| | | |
|---|---|---|
| $E_{\|\|}$ | | Electron energy parallel to magnetic field |
| $E_\perp$ | | Electron energy perpendicular to magnetic field |
| $T_{\|\|}$ | | Plasma temperature parallel to magnetic field |
| $T_\perp$ | | Plasma temperature perpendicular to magnetic field |
| $T_w$ | | Temperature of trap wall |
| $v_{\|\|}$ | $\sqrt{2E_{\|\|}/m_e}$ | Electron velocity parallel to magnetic field |
| $\bar{v}$ | $\sqrt{kT/m_e}$ | Thermal electron velocity |

## ********** Lengths **********

| | | |
|---|---|---|
| $D$ | | Displacement of plasma from the trap axis |
| $L_c$ | | Length of grounded confinement region |
| $L(x,y)$ | Eq.4.16 | Plasma length profile |
| $L_0(\rho)$ | Eq.4.18 | Azimuthally averaged plasma length profile |
| $\delta L(\rho)$ | Eq.4.17 | Amplitude of variation of plasma length in $\psi$ |
| $L_p$ | Eq.2.12 | Mean plasma length |
| $R_p$ | | Plasma column radius |
| $r_c$ | $\bar{v}/\omega_c$ | Thermal electron gyroradius |
| $b$ | $e^2/kT$ | Distance of closest approach |
| $\lambda_D$ | $\sqrt{kT/4\pi ne^2}$ | Debye length |
| $R_w$ | 1.27 cm | Wall radius of trap |
| $R_i$ | Fig.2.2 | Radius of $i$th P1–P5 collector plate |

********** **Times and Frequencies** **********

| | | |
|---|---|---|
| $\omega_c$ | $eB/m_e c$ | Electron gyrofrequency |
| $\omega_p$ | $\sqrt{4\pi n e^2/m_e}$ | Electron plasma frequency |
| $\overline{f_B}$ | $\bar{v}/2L_p$ | Thermal electron axial bounce frequency |
| $f_E$ | $-E_r c/2\pi r B$ | $\mathbf{E} \times \mathbf{B}$ rotation frequency |
| $f_d$ | $\approx (R_p/R_w)^2 f_E$ | $m = 1$ diocotron mode frequency |
| $\omega_R$ | $2\pi(f_E - f_d)$ | $\mathbf{E} \times \mathbf{B}$ rotation frequency in the diocotron mode frame |
| $f_{mod}$ | | Applied voltage modulation frequency |
| $\nu_{\perp\parallel}$ | Eq.2.15 | $T_\parallel$-$T_\perp$ collisional equilibration rate |
| $\nu_{ee}$ | Eq.2.18 | Electron-electron collision rate |
| $\nu_3$ | Eq.4.27 | 3 body collision rate |
| $\tau_m$ | | Plasma column lifetime |
| $\tau_{rad}$ | | Plasma cooling time due to cyclotron radiation when $\nu_{\perp\parallel} \gg \tau_{rad}^{-1}$ |
| $\gamma$ | -(dD/dt)/D | $m = 1$ diocotron mode damping rate |
| $\gamma_{est}$ | Eq.4.22 | Estimate of $m = 1$ diocotron mode damping rate from rotational pumping theory |
| $\gamma_{rp}$ | Eq.4.21 | Exact $m = 1$ diocotron mode damping rate from rotational pumping theory |
| $\gamma_{sq}$ | | $m = 1$ diocotron mode squeeze damping rate |
| $\gamma_{ns}$ | | $m = 1$ damping rate with no squeeze |
| $\gamma_m$ | | Damping rate of $m \geq 2$ diocotron modes |

Note that $\omega = 2\pi f$ for all frequencies.

********** **Integrals** **********

| | | |
|---|---|---|
| $n_z$ | $\int dz\, n$ | $z$-integrated plasma density |
| $N$ | $\int d^3r\, n$ | Total number of electrons |
| $N_L$ | $N/L_p$ | Number of electrons per unit length |
| $P_\theta$ | Eq.3.1 | Angular momentum |
| $\langle r^2 \rangle$ | $\int d^3r\, nr^2/N$ | Mean square radius of plasma about trap axis |
| $\langle \rho^2 \rangle$ | $\langle r^2 \rangle - D^2$ | Mean square radius of plasma about plasma axis |
| $H_\phi$ | Eq.4.3 | Electrostatic energy per electron |
| $H_T$ | Eq.4.4 | Thermal energy per electron |
| $H_{rad}$ | Eq.4.5 | Energy loss due to cyclotron radiation per electron |
| $W_{ps}$ | Eq.4.6 | Work done by plasma on power supplies per electron |
| $\phi_p$ | | Electrostatic potential at plasma center |

********** **Miscellaneous** **********

| | | |
|---|---|---|
| P1–P5 | | Collector plates |
| L1–L6 | | Trap cylinders |
| $m$ | | Azimuthal mode number |
| $V_c$ | | Confinement voltage |
| $V_{sq}$ | | Squeeze voltage |
| $V_{mod}$ | | Applied modulated voltage |
| $\Gamma_\rho^{exp}$ | Eq.4.20 | Experimental $z$-integrated, $\psi$-averaged radial electron flux |
| $\Gamma_\rho^{th}$ | Eq.4.14 | Theoretical rotational pumping flux |
| $\eta$ | Eq.E.7 | First, or shear, viscosity coefficient |
| $\mu$ | $\eta/nm_e$ | Kinematic viscosity coefficient |
| $\zeta$ | Eq.4.29 | Second, or bulk, viscosity coefficient |
| $C_s$ | Eq.B.17 | End slant coefficient |

# References


[1] B. R. Beck. *Measurement of the Magnetic and Temperature Dependence of the Electron-Electron Anisotropic Temperature Relaxation Rate.* PhD thesis, University of California at San Diego, 1990.

[2] B. R. Beck, J. Fajans, and J. H. Malmberg. Measurement of collisional anisotropic temperature relaxation in a strongly magnetized pure electron plasma. *Phys. Rev. Lett.*, 68:317, 1992.

[3] S. I. Braginskii. Transport processes in a plasma. *Reviews of Plasma Physics*, 1:205, 1965.

[4] R. J. Briggs, J. D. Daugherty, and R. H. Levy. Role of Landau damping in crossed-field electron beams and inviscid shear flow. *Phys. Fluids*, 13:421, 1970.

[5] J. D. Crawford and T. M. O'Neil. Nonlinear collective processes and the confinement of a pure-electron plasma. *Phys. Fluids*, 30:2076, 1987.

[6] J. D. Crawford, T. M. O'Neil, and J. H. Malmberg. Effect of nonlinear collective processes on the confinement of a pure electron plasma. *Phys. Rev. Lett.*, 54:697, 1985.

[7] S. M. Crooks and T. M. O'Neil. Rotational pumping and damping of the $m = 1$ diocotron mode. *Phys. Plasmas*, 2:355, 1995.

[8] J. S. deGrassie and J. H. Malmberg. Waves and transport in the pure electron plasma. *Phys. Fluids*, 23:63, 1980.

[9] M. H. Douglas and T. M. O'Neil. Transport of a nonneutral electron plasma due to electron collisions with neutral atoms. *Phys. Fluids*, 21:920, 1978.

[10] C. F. Driscoll and K. S. Fine. Experiments on vortex dynamics in pure electron plasmas. *Phys. Fluids B*, 2:1359, 1990.

[11] C. F. Driscoll, K. S. Fine, and J. H. Malmberg. Reduction of radial losses in a pure electron plasma. *Phys. Fluids*, 29:2015, 1986.

[12] C. F. Driscoll and J. H. Malmberg. Length-dependent containment of a pure electron plasma. *Phys. Rev. Lett.*, 50:167, 1983.

[13] C. F. Driscoll, J. H. Malmberg, and K. S. Fine. Observation of transport to thermal equilibrium in pure electron plasmas. *Phys. Rev. Lett.*, 60:1290, 1988.

[14] D. L. Eggleston, C. F. Driscoll, B. R. Beck, A. W. Hyatt, and J. H. Malmberg. Parallel energy analyzer for pure electron plasma devices. *Phys. Fluids B*, 4:3432, 1992.

[15] D. L. Eggleston and J. H. Malmberg. Observation of an induced scattering instability driven by static field asymmetries in a pure electron plasma. *Phys. Rev. Lett.*, 59:1675, 1987.

[16] K. S. Fine. *Experiments with the $l = 1$ Diocotron Mode.* PhD thesis, University of California at San Diego, 1988.

[17] K. S. Fine. Simple model of a finite length diocotron mode. *Bull. Am. Phys. Soc.*, 36:2331, 1991.

[18] K. S. Fine. Simple model of a nonlinear diocotron mode. *Phys. Fluids B*, 4:3981, 1992.

[19] K. S. Fine, A. C. Cass, W. G. Flynn, and C. F. Driscoll. Relaxation of 2D turbulence to vortex crystals. *Phys. Rev. Lett.*, 1995. (Submitted).

[20] K. S. Fine, C. F. Driscoll, and J. H. Malmberg. Measurements of a nonlinear diocotron mode in pure electron plasmas. *Phys. Rev. Lett.*, 63:2232, 1989.

[21] G. Gabrielse, X. Fei, L. A. Orozco, R. L. Tjoelker, et al. Thousandfold improvement in the measured antiproton mass. *Phys. Rev. Lett.*, 65:1317, 1990.

[22] M. E. Glinsky, T. M. O'Neil, M. N. Rosenbluth, K. Tsuruta, and S. Ichimaru. Collisional equipartition rate for a magnetized pure electron plasma. *Phys. Fluids B*, 4:1156, 1992.

[23] D. L. Goodman, C. C. Patty, and R. S. Post. Radial ion transport measurements in a nonaxisymmetric magnetic mirror. *Phys. Fluids B*, 2:2173, 1990.

[24] R. W. Gould and M. A. LaPointe. Cyclotron resonance in a pure electron plasma column. *Phys. Rev. Lett.*, 67:3685, 1991.

[25] R. G. Greaves, M. D. Tinkle, and C. M. Surko. Creation and uses of positron plasmas. *Phys. Plasmas*, 1:1439, 1994.

[26] J. A. Helffrich, B. Cluggish, and J. H. Malmberg. Dance of the diocotron and long-time evolution of a pure electron plasma. *Bull. Am. Phys. Soc.*, 36:2331, 1991.

[27] P. G. Hjorth and T. M. O'Neil. Numerical study of a many particle adiabatic invariant. *Phys. Fluids*, 30:2613, 1987.

[28] E. B. Hooper, Jr., R. H. Cohen, D. L. Correll, and J. M. Gilmore *et al.*. Non-ambipolar radial particle transport in a tandem mirror. *Phys. Fluids*, 28:3609, 1985.

[29] X. P. Huang and C. F. Driscoll. Relaxation of 2D turbulence to a meta-equilibrium near the minimum enstrophy state. *Phys. Rev. Lett.*, 72:2187, 1994.

[30] X. P. Huang, K. S. Fine, and C. F. Driscoll. Coherent vorticity holes from 2D turbulence decaying in a background shear flow. *Phys. Rev. Lett.*, 1994. (Submitted).

[31] A. W. Hyatt, C. F. Driscoll, and J. H. Malmberg. Measurement of the anisotropic temperature relaxation rate in a pure electron plasma. *Phys. Rev. Lett.*, 59:2975, 1987.

[32] J. D. Jackson. *Classical Electrodynamics.* John Wiley and Sons, second edition, 1975.

[33] C. A. Kapetanakos and A. W. Trivelpiece. Diagnostics of non-neutral plasmas using an induced-current electrostatic probe. *Jour. Appl. Phys.*, 42:4841, 1971.

[34] S. S. Khirwadkar, P. I. John, K. Avinash, A. K. Agarwal, and P. K. Kaw. Steady state formation of a toroidal electron cloud. *Phys. Rev. Lett.*, 71:3443, 1993.

[35] J. D. Lambert. *Vibrational and Rotational Relaxation in Gases.* Clarendon, Oxford, England, 1977. Sect. 2.2.

[36] L. D. Landau and E. M. Lifshitz. *Fluid Mechanics, Landau and Lifshitz Course of Theoretical Physics*, volume 6. Pergamon Press, second edition, 1987.

[37] J. H. Malmberg and C. F. Driscoll. Long-time containment of a pure electron plasma. *Phys. Rev. Lett.*, 44:654, 1980.

[38] T. B. Mitchell. *Experiments on Electron Vortices in a Malmberg-Penning Trap.* PhD thesis, University of California at San Diego, 1993.

[39] T. B. Mitchell and C. F. Driscoll. Symmetrization of 2D vortices by beat-wave damping. *Phys. Rev. Lett.*, 73:2196, 1994.

[40] T. B. Mitchell, C. F. Driscoll, and K. S. Fine. Experiments on stability of equilibria of two vortices in a cylindrical trap. *Phys. Rev. Lett.*, 71:1371, 1993.

[41] J. Notte and J. Fajans. The effect of asymmetries on non-neutral plasma confinement time. *Phys. Plasmas*, 1:1123, 1994.

[42] J. Notte, A. J. Peurrung, J. Fajans, R. Chu, and J. S. Wurtele. Asymmetric stable equilibria of non-neutral plasmas. *Phys. Rev. Lett.*, 69:3056, 1992.

[43] T. M. O'Neil. A confinement theorem for nonneutral plasmas. *Phys. Fluids*, 23:2216, 1980.

[44] T. M. O'Neil. Cooling of a pure electron plasma by cyclotron radiation. *Phys. Fluids*, 23:725, 1980.

[45] T. M. O'Neil. A new theory of transport due to like-particle collisions. *Phys. Rev. Lett.*, 55:943, 1985.

[46] T. M. O'Neil, C. F. Driscoll, and D. H. E. Dubin. Like particle transport: A new theory and experiments with pure electron plasmas. In *Turbulence and Anomalous Transport in Magnetized Plasmas - Proc. of Int. Workshop on Small Scale Turbulence and Anomalous Transport in Magnetized Plasmas*, pages 293–308. Editions de Physique, Orsay, 1987.

[47] T. M. O'Neil and R. A. Smith. Stability theorem for off-axis states of a non-neutral plasma column. *Phys. Fluids B*, 4:2720, 1992.

[48] A. J. Peurrung and J. Fajans. Nonneutral plasma shapes and edge profiles. *Phys. Fluids B*, 2:693, 1990.

[49] A. J. Peurrung and J. Fajans. A limitation to the analogy between pure electron plasmas and two-dimensional inviscid fluids. *Phys. Fluids B*, 5:4295, 1993.

[50] A. J. Peurrung and J. Fajans. Three-dimensional non-neutral plasma shapes. *Phys. Fluids B*, 5:4250, 1993.

[51] D. L. Phillips. A technique for the numerical solution of certain intergral equations of the first kind. *Jour. Assoc. Comp. Mach.*, 9:84, 1962.

[52] N. S. Pillai and R. W. Gould. Damping and trapping in 2D inviscid fluids. *Phys. Rev. Lett.*, 73:2849, 1994.

[53] S. A. Prasad and T. M. O'Neil. Vlasov theory of electrostatic modes in a finite length electron column. *Phys. Fluids*, 27:206, 1984.

[54] H. D. Price, A. J. Lichtenberg, M.A. Lieberman, and M. Tuszewski. Radial and axial losses in a multiple-mirror experiment. *Nucl. Fusion*, 23:1043, 1983.

[55] D. D. Ryutov and G. V. Stupakov. Diffusion of resonance particles in ambipolar plasma traps. *Doklady AkademiiNauk SSSR*, 240:1086, 1978.

[56] D. D. Ryutov and G. V. Stupakov. Neo-classical theory of transport processes in ambipolar traps. *Fizika Plazmy*, 4:501, 1978.

[57] P. G. Saffman and R. Szeto. Equilibrium shapes of a pair of equal uniform vortices. *Phys. Fluids*, 23:2339, 1980.

[58] E. Sarid, F. Anderegg, and C. F. Driscoll. Cyclotron resonance phenomenon in a non-neutral multi-species ion plasma. *Phys. Plasmas*, 1995. (Accepted).

[59] W. M. Stacey and D. R. Jackson. Poloidal rotation, density asymmetries, and momentum confinement in tokamak experiments. *Phys. Fluids B*, 5:1828, 1993.

[60] T. H. Stix. Decay of poloidal rotation in a tokamak plasma. *Phys. Fluids*, 16:1260, 1973.

[61] C. R. Subrahmanya. A new method of deconvolution and its application to lunar occultations. *Astronomy and Astrophysics*, 89:132, 1980.

[62] S. Twomey. On the numerical solution of Fredholm integral equations of the first kind by the inversion of the linear system produced by quadrature. *Jour. Assoc. Comp. Mach.*, 10:97, 1963.

[63] W. D. White, J. H. Malmberg, and C. F. Driscoll. Resistive wall destabilization of diocotron waves. *Phys. Rev. Lett.*, 49:1822, 1982.

[64] D. J. Wineland, W. M. Itano, J. C. Bergquist, S. L. Gilbert, J. J. Bollinger, and F. Ascarrunz. Liquid and solid ion plasmas. In C. W. Roberson and C. F. Driscoll, editors, *Non-Neutral Plasma Physics*, page 93. American Institute of Physics, 1988.